

University of Nevada, Reno

Exploring the Spin Density and Electrochemical Properties of Benzotriazinyl Radicals: Advancement in Functional Materials for Flow Battery Application

A thesis submitted in partial fulfillment of the requirements for the degree of Master of Science in Chemistry

by

Kingsley Eberechukwu Onyenwe

Dr. Natia L. Frank/Thesis Advisor

August , 2025

Copyright by Kingsley E. Onyenwe 2025

All Rights Reserved



THE GRADUATE SCHOOL

We recommend that the thesis
prepared under our supervision by

kingsley E, Onyenwe

entitled

**Exploring the Spin Density and Electrochemical Properties
of Benzotriazinyl Radicals: Advancement in Functional
Materials for Flow Battery Application**

be accepted in partial fulfillment of the
requirements for the degree of

Master of Science

Frank L. Natia, Ph.D.
Advisor

Jeffrey S. Christopher, Ph.D.
Committee Member

Kistin A. Lewis, Ph.D.
Graduate School Representative

Markus Kemmelmeier, Ph.D., Dean
Graduate School

August, 2025

Abstract:

Redox flow batteries (RFBs) are charge storage devices that are particularly well-suited for grid-scale energy storage due to their long-life span, independent scalability of power and energy, enhanced safety compared to other battery technologies, ability to handle a large number of charge-discharge cycles without significant degradation, and potential for cost-effectiveness at large scales. The dominant material for redox flow batteries is based on inorganic vanadyl salts, which provide large cell voltages and excellent fatigue resistance. Redox-active organic compounds are promising alternatives to traditional inorganic redox-active compounds for redox flow battery (RFB) applications due to their tunable electrochemical properties through molecular design and synthesis, as well as their potential for faster charge-discharge kinetics.

Stable organic radicals have come to the forefront of this field, in which fully reversible electrochemical processes are often observed. Benzotriazinyl radicals are unique materials for redox flow battery (RFBs) applications owing to their bipolar redox chemistry which arises from the ability to undergo fully reversible reduction and oxidation processes. Previous work suggests that benzotriazinyls are promising for redox flow batteries, but challenges arise in increasing the cell voltage. In this work, we report the design, synthesis and characterization of a series of 6-position functionalized 1,3-diphenyl-1,2,4-benzotriazinyl radicals (6-X-BTR, where X = H, Cl, CH₃, NH₂, NO₂, and OMe) toward the aim of increasing cell voltage and charge/discharge kinetics. The electronic structures of the 6-X-BTR series were characterized by electronic absorption spectroscopy, electron

paramagnetic resonance (EPR), cyclic voltammetry (CV), computational methods, and, for some of the series, single-crystal X-ray diffraction (SCXRD). Cyclic voltammetry confirmed reversible reduction and oxidation processes for all stable radical derivatives, revealing tunable redox potentials and moderate cell voltages (~ 1.0 V). Electron-withdrawing substituents (e.g., $-\text{Cl}$ and $-\text{NO}_2$) were found to stabilize the radical anion forms, as indicated by anodically shifted reduction potentials, as expected. Heterogeneous electron-transfer rates were measured for the series in which it was found that some of the derivatives had a faster electron transfer kinetics compared to previously reported benzotriazinyl derivative. Substituent effects are rationalized based on a combination of computation, electronic absorption spectra and spin densities obtained by room temperature EPR. Attempts to gain structural insight from the 6-amino-benzotriazinyl radical lead to SCXRD crystallographic characterization of an 8-amino-functionalized leuco radical, which suggest that steric interactions may inhibit final oxidation to the benzotriazinyl radical. Electronic absorption spectroscopy (UV-vis) and EPR analyses were used to follow the conversion of the leuco to the radical form which occurs slowly over 14–15 hours in the presence of oxygen as an oxidant. Overall, these results provide insights into the role of steric hindrance and planarity in stabilizing the redox processes in these unique radicals and support the potential of functionalized benzotriazinyl radicals as tunable, bipolar electrolytes for RFB charge storage materials with fast charge-discharge kinetics.

Acknowledgments

It's true that science is not done in a vacuum and that success in graduate school depends largely on supervisor's support. For this, I want to thank my supervisor Natia L, Frank for allowing me to stay and learn in the lab. Dr. Subrata Ghosh for all his genuine show of love and help throughout these years; you always showed up and helped answer questions to a curious mind. To my brothers Victor and Prakash, and Chinedu, thank you for all your support. To my other colleagues and good friends- Garret, Hailey, Tanzil, Nikhil, Jessica, and Julian. Etc. I am grateful for your help and support.

Lastly, I want to Thank Dr Stephen Spain and Dr Nina Ruprecht, for always helping with instrumentation and training.

Table of Contents

Chapter 1. Grid-scale electrochemical energy storage.....	1
1. Redox flow batteries	1
1.1 Working Principle of a Redox Flow Battery.....	3
1.2 Non-Aqueous Flow Batteries and Symmetric Redox Flow Batteries	6
1.3 Challenges in Organic Redox Flow Battery Technology.....	9
1.4 1,3-Diphenyl-1,2,4-Benzotriazinyl - A Stable Organic Radical	10
1.5 Thesis goal	12
1.6 Specific Aims	14
1.7 Thesis scope and organization	15
Chapter 2. Synthesis and Characterization of 6-Substituted 1,3-Diphenyl-1,2,4- benzotriazinyl Derivatives	18
2.1. Stable Organic Radicals.....	18
2.2. The 1,3-Diphenyl-1,2,4-benzotriazin-4-yl (DPBT) Radical.....	21
2.3 Results and discussion	34
2.4 Molecular structure	38
2.5 Spectroscopic characterization.....	47

2.5.1 Electronic absorption spectroscopy	47
2.5.2 Electron Paramagnetic Resonance (EPR) Analysis for Radicals 1.1-1.5	50
2.6 Electrochemistry	54
2.7 Heterogeneous rate constant and diffusion coefficient for 1.2, 1.3, 1.4, and 1.5....	61
2.8 Maximum solubility measurement for 1.4.....	73
2.9 Conclusion	75
3.0 Experimental.....	76
3.1.1 General Procedures and Characterization.....	76
Chapter 3.....	82
3.1 Conclusion and outlook	82
References.....	86
Appendix A DFT calculation output parameters.....	106
Appendix B ¹ H-NMR and ¹³ C-NMR spectra.....	110
.....	115
Appendix C Complete listings of bond lengths and angles	116
Appendix D SC-XRD Crystallographic data for 1.8 and 2.11.....	127
Appendix E X-band CW-EPR Spectrum of radicals 1.1-1.5	128
Appendix G Complete FTIR (ATR) Data.....	131
Appendix H: Complete HRMS Data	137

Appendix F Absorption Spectroscopic and cyclic voltammetry data for radical 1.1 and	
1.12.....	144

List of Tables

Table 2. 1	Summary of the X-ray crystallographic data for 1.12	40
Table 2. 2	Selected bond lengths (Å) and angles (°) for 1.12.	41
Table 2. 3	Selected Torsional angles (°) for 1.12 and 1.0	42
Table 2. 4	Summary of the X-ray crystallographic data for 1.4	44
Table 2. 5	Selected bond lengths (Å) and angles (°) for 1.4.	46
Table 2. 6	Key Torsional angles (°) for 1.4 and 1.0	46
Table 2. 7	Selected Bond Angles (°)	47
Table 2. 8	Absorption data for radicals 1.1,1.3,1.5,1.6, and 1.0.	50
Table 2. 9	Hyperfine coupling constants (a_N) and g-values the series of radicals.	52
Table 2. 10	Select electrochemical parameters for 1.2, 1.3, 1.4, 1.5 and 1.0.....	59
Table 2. 11	Diffusion coefficient and rate constant for 1.1, 1.3, 1.6, and 1.10	63

List of figures

Figure 1. 1 Project, named Fifth Standard, is RWE's largest U.S. storage facility to date, at 137 megawatts (MW), and includes a 150-MW solar PV array expected to be complete in August. When fully energized, the facility, located in Fresno County, will have the capacity to power more than 26,000 homes (ref.11).....	3
Figure 1. 2 Examples of organic redox active molecular systems utilized in charge storage materials, with the range of redox processes given in V vs Ag/AgCl. (Ref 15).....	8
Figure 1. 3 IUPAC numbering for parent BTR compound 1.0	11
Figure 1. 4 Stable organic radical classes	19
Figure 1. 5 Resonance structures of 1.0	23
Figure 1. 6 The Crystal Structure of leuco Radical 1.12 (50% Probability Ellipsoids and Hydrogen Atoms shown.....	39
Figure 1. 7 Crystal Structure of Radical 1.4 (50% Probability Ellipsoids and Hydrogen Atoms omitted for Clarity	43
Figure 1. 8 Electronic absorption spectra of 2.9,1.2-1.5 in toluene at 300k	50
Figure 1. 9 CW X-Band EPR spectrum of 1.7 in toluene at 298k	54
Figure 1. 10 Electrochemical oxidation and reduction process of benzotriazinyl radicals.....	56

- Figure 1. 11 Effect of EWG and EDG substitution on electrochemistry (V vs SCE) ..56
- Figure 1. 12 Cyclic voltammograms of radical 1.4 in MeCN with 0.1 M [Bu₄N][PF₆]
supporting electrolyte, glassy carbon working electrode, silver reference
electrode, platinum counter electrode, 10-200 mV/s scan rate64
- Figure 1. 13 Peak currents (i_{pc} and i_{pa}) from CV data vs. $v^{1/2}$ for the reduction process
used to determine the diffusion coefficient from Randles Sevcik equation (see
equation (S2) for radical 1.4. Lines are least-squares fits to the data65
- Figure 1. 14 Peak currents (i_{pc} and i_{pa}) from CV data vs. $v^{1/2}$ for the oxidation process
used to determine the diffusion coefficient from Randles Sevcik equation (see
equation (S2) for radical 1.4. Lines are least-squares fits to the data65
- Figure 1. 15 Nicholson dimensionless coefficient Ψ (see Equation (S5 and S5) vs. v
 $^{1/2}$ used to determine the electron transfer rate constants k^0 for 1.466
- Figure 1. 16 Cyclic voltammograms of radical 1.2 in MeCN with 0.1 M [Bu₄N][PF₆]
supporting electrolyte, glassy carbon working electrode, silver reference
electrode, platinum counter electrode, 10-250 mV/s scan rate67
- Figure 1. 17 Peak currents (i_{pc} and i_{pa}) from CV data vs. $v^{1/2}$ used to determine the
diffusion coefficient from Randles Sevcik equation (see equation (S2) for
radical 1.2. Lines are least-squares fits to the data67
- Figure 1. 18 Peak currents (i_{pc} and i_{pa}) from CV data vs. $v^{1/2}$ used to determine the
diffusion coefficient from Randles Sevcik equation (see equation (S2) for
radical 1.2. Lines are least-squares68

- Figure 1. 19 Nicholson dimensionless coefficient Ψ (see Equation (S4 and S5) vs. $v^{1/2}$ used to determine the electron transfer rate constants k^0 68
- Figure 1. 20 Cyclic voltammograms of radical 1.5 in MeCN with 0.1 M [Bu₄N][PF₆] supporting electrolyte, glassy carbon working electrode, silver reference electrode, platinum counter electrode, 10-500 mV/s scan rate69
- Figure 1. 21 Peak currents (i_{pc} and i_{pa}) from CV data vs. $v^{1/2}$ used to determine the diffusion coefficient from Randles Sevcik equation (see equation (S2) for radical 1.5. Lines are least-squares fits to the data69
- Figure 1. 22 Peak currents (i_{pc} and i_{pa}) from CV data vs. $v^{1/2}$ used to determine the diffusion coefficient from Randles Sevcik equation (see equation (S2) for radical 1.5. Lines are least-squares fits to the data70
- Figure 1. 23 Nicholson dimensionless coefficient Ψ (see Equation (S4 and S5) vs. $v^{1/2}$ used to determine the electron transfer rate constants k^0 70
- Figure 1. 24 Cyclic voltammograms of radical 1.3 in MeCN with 0.1 M [Bu₄N][PF₆] supporting electrolyte, glassy carbon working electrode, silver reference electrode, platinum counter electrode, 50-500 mV/s scan rate71
- Figure 1. 25 Peak currents (i_{pc} and i_{pa}) from CV data vs. $v^{1/2}$ used to determine the diffusion coefficient from Randles Sevcik equation (see equation (S1) for radical 1.3. Lines are least-squares fits to the data71

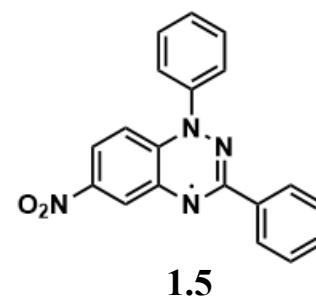
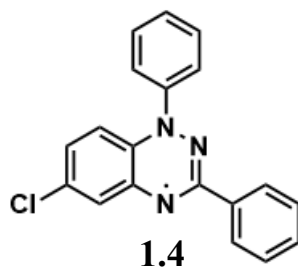
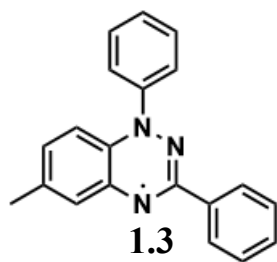
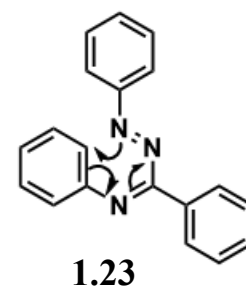
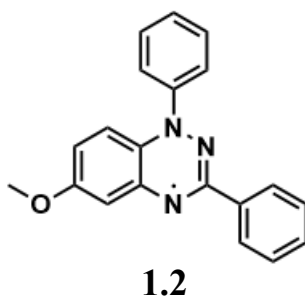
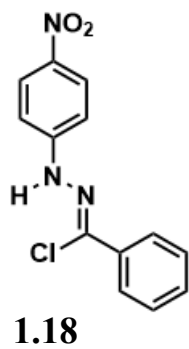
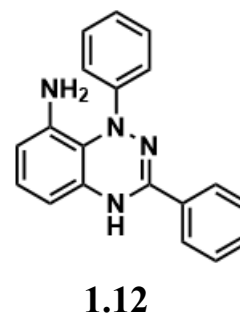
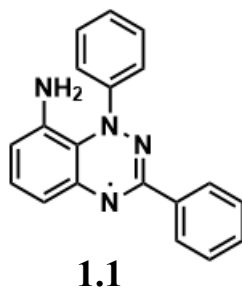
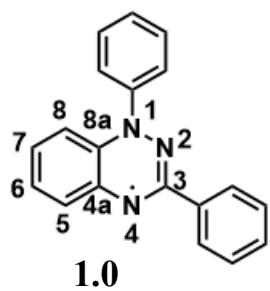
Figure 1. 26 Peak currents (i_{pc} and i_{pa}) from CV data vs. $v^{1/2}$ used to determine the diffusion coefficient from Randles Sevcik equation (see equation (S2) for radical 1.3. Lines are least-squares fits to the data	72
Figure 1. 27 Nicholson dimensionless coefficient Ψ (see Equation (S4 and S5) vs. $v^{1/2}$ used to determine the electron transfer rate constants k^0	72
Figure 1. 28 Absorption spectra of 1.1 in CH3CN at various concentrations. (top left). Calibration curve based on the peak absorbance maximum at 270 nm (top right). Absorption spectra for the saturated sample (bottom). red data point indicating sample concentration.	74
Figure 1. 29 The Crystal Structure of 1,3,7,9-Tetraphenyl-1H-benzo[1,2-e:5,4-e' bis([1,2,4]triazine)-9-ium-6-ide (2.11-TPHA) (50% Probability Ellipsoids and Hydrogen Atoms Omitted for Clarity. Two molecules seen in the asymmetric unit cell.....	127
Figure 1. 30 Crystal Structure of 1.8 (50% Probability Ellipsoids and Hydrogen Atoms omitted for Clarity	127
Figure 1. 31 X-band CW-EPR spectrum of 1.3 in toluene at 298 K	128
Figure 1. 32 X-band CW- EPR spectrum of 1.2 in toluene at 298 K	128
Figure 1. 33 CW X-band EPR spectrum of 1.4 in toluene at 298 K	129
Figure 1. 34 Experimental and simulated EPR spectrum of 1.1 in toluene at 298 K	130
Figure 1. 35 Electronic absorption spectra of 1.1 in acetonitrile at 300k.....	144

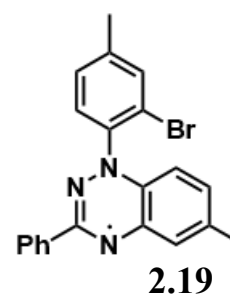
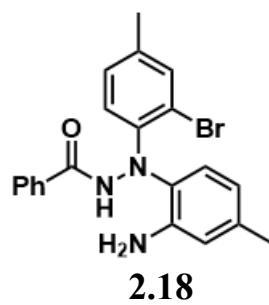
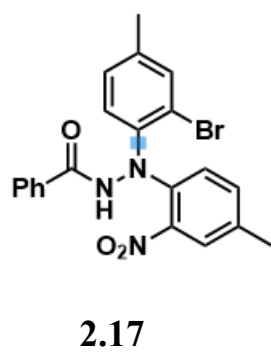
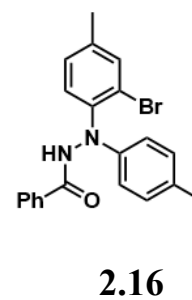
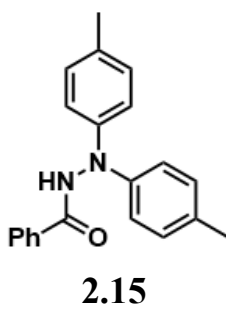
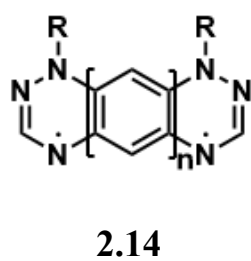
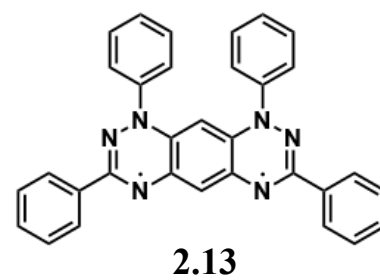
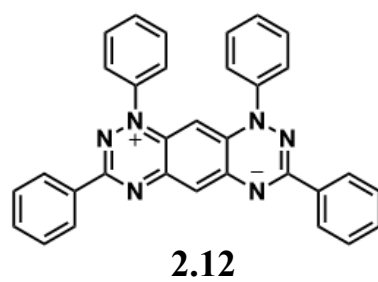
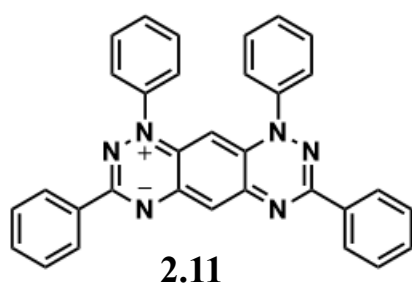
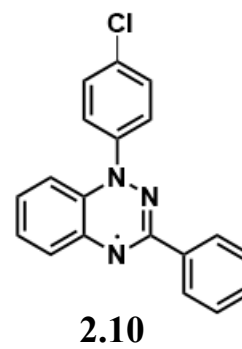
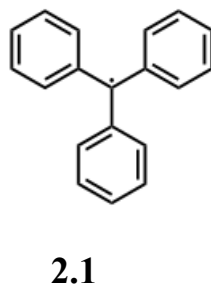
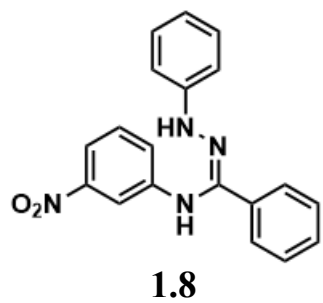
Figure 1. 36 Time-dependent Cyclic voltammogram of radical 1.1 in MeCN with 0.1 M [Bu₄N][PF₆] supporting electrolyte, glassy carbon working electrode, silver reference electrode, platinum counter electrode, 100 mV/s scan rate 145

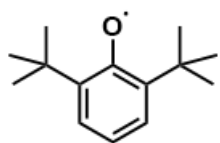
List of schemes

Scheme 2.1 Blatter Synthesis (Route A) ^a	25
Scheme 2.2 Blatter Synthesis (Route B) ^a	26
Scheme 2.3 Kadirov synthesis (Route C) ^a	27
Scheme 2.4 Neugebauer synthesis (Route D) ^a	28
Scheme 2.5 Proposed mechanism of oxidative radical formation	30
Scheme 2.6 The mechanism for the formation of 2.32.	30
Scheme 2.7 Synthesis of 7-bromo-1,3-diphenyl-1,2,4-benzotriazin-4-yl (2.38) (Route E) ^a	32
Scheme 2.8 Proposed mechanism of base and acid-catalyzed radical formation ..	33
Scheme 2.9 Synthesis of radical 1.1-1.5	35

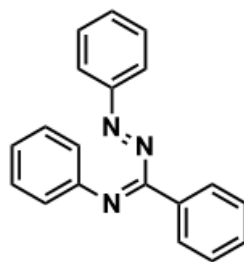
List of Numbered Compounds



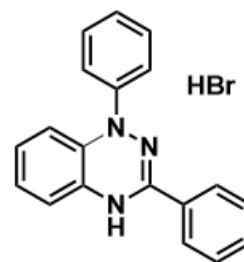




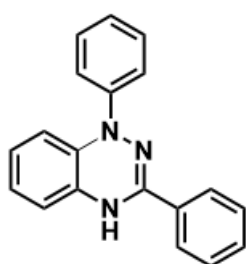
2.2



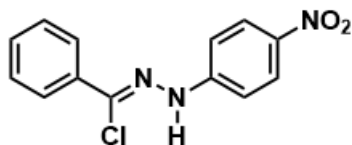
2.20



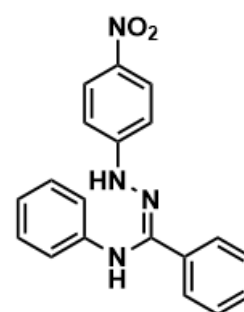
2.21



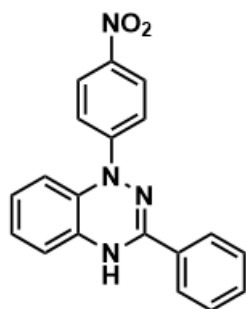
2.22



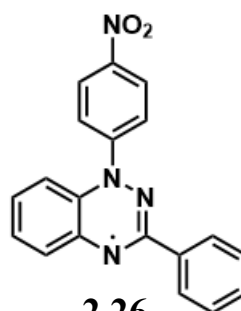
2.23



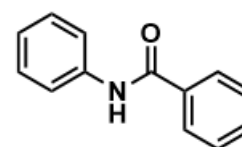
2.24



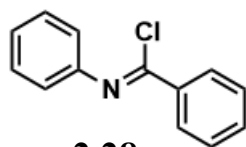
2.25



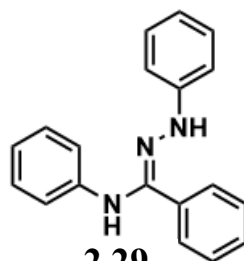
2.26



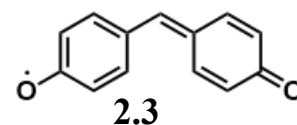
2.27



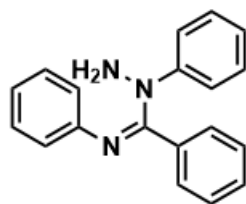
2.28



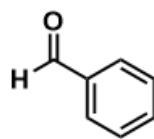
2.29



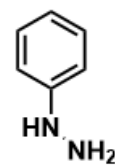
2.3



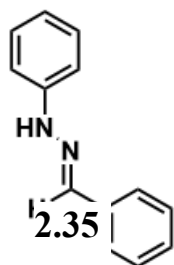
2.30



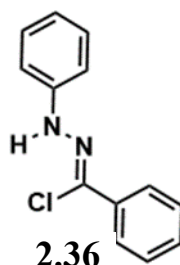
2.33



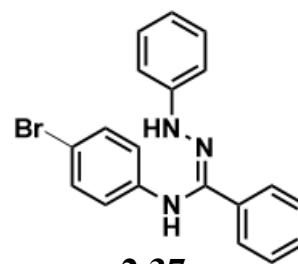
2.34



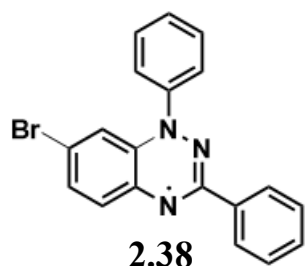
2.35



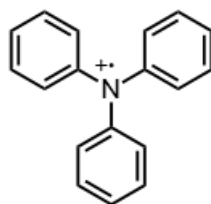
2.36



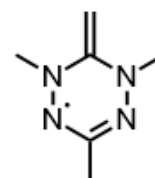
2.37



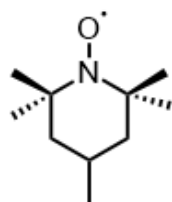
2.38



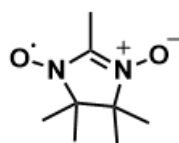
2.4



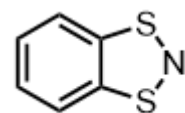
2.5



2.6



2.7



2.8

List of Abbreviations

6-31G(d, p)	a split valence plus polarization basis set
<i>a</i>	hyperfine coupling constant
°C	degrees Celsius
cm	centimeter
DBU	1,8-diazabicyclo [5.4.0] undec-7-ene
DFT	density functional theory
DMF	dimethylformamide
E_{cell}	electrochemical cell potential or disproportionation energy
$E_{1/2(\text{ox})}$	oxidation half-wave potential
$E_{1/2(\text{red})}$	reduction half-wave potential
ΔE_p	peak-to-peak separation between anodic and cathodic waves
EDG	electron donating group
ENDOR	electron-nuclear double resonance
EPR	electron paramagnetic resonance
ESI-MS	electrospray ionization mass spectrometry
EtOH	ethanol

EWG	electron withdrawing group
F	Faraday constant (96 485.34 C·mol ⁻¹)
<i>g</i>	<i>g</i> -factor (Lande factor)
G	Gauss
HOMO	highest occupied molecular orbital
Hz	Hertz
IR	infrared
LUMO	lowest unoccupied molecular orbital
ORFB	Organic redox flow battery
ROM	Redox-active molecule
M	molarity
mol	mole
mV	millivolt
MeCN	acetonitrile
MeOH	methanol
Me ₂ S	dimethyl sulfide
MHz	megahertz

ν	Scan rate
k^0	heterogenous rate constant
NCS	N-Chlorosuccinimide
NMR	nuclear magnetic resonance
π	Pi=3.1416
D	diffusion coefficient
I_p	peak current
Ψ	Nicholson dimensionless constant
OMe	methoxy
ORB	organic radical battery
RFB	Redox flow battery
(A-ONRBs)	All organic non-aqueous redox flow batteries
(ARFBs)	Aqueous redox flow batteries
(NARFBs)	non-aqueous redox flow batteries
TPHA	Tetraphenylhexaazaanthracene
Q	McConnell equation proportionality constant
SCE	saturated calomel electrode

SOMO	Singly occupied molecular orbital
T	Temperature
TD-DFT	time-dependent density functional theory
TEA	triethylamine
TEMPO	2,2,6,6-tetramethyl-1-piperidinyloxy
THF	tetrahydrofuran
TLC	thin layer chromatography
UB3LYP	unrestricted Becke 3-parameter Lee-Yang-Parr
UV	ultraviolet
V	volt
XRD	X-ray diffraction
E	extinction coefficient
λ	wavelength
ρ	spin density

Chapter 1. Grid-scale electrochemical energy storage

1. Redox flow batteries

Electrical energy demand has been increasing exponentially, and predictions suggest that global electricity generation will increase from 21.6 trillion kWh in 2012 to 36.5 trillion kWh by 2040.¹ Issues of sustainability² and diminishing fossil reserves have necessitated the exploration of abundant renewables such as solar and wind as alternative sources for electricity generation.³ Power generated from solar and wind energy systems is however intermittent, requiring that energy generated during peak operation be adequately stored and used when needed.

Lithium ion batteries along with redox flow batteries are among the most promising array of energy storage systems aimed at tackling the intermittency experienced with wind and solar renewable energy systems.⁴ At present, lithium-ion batteries dominate the commercial energy storage market, largely due to their high gravimetric energy density $>250 \text{ Wh L}^{-1}$, and falling battery pack cost at a reported yearly decline rate of 8%.⁵ However, concerns with lithium-ion batteries include fire hazards arising from the use of flammable organic electrolytes, and irreversible aging due to phase transitions (changes in the physical structure of a material) even when not in use.⁶

Redox flow batteries (RFBs) are particularly well-suited for large-scale energy storage due to their scalability, long cycle life, and the ability to decouple power and energy capacity.⁷ Unlike lithium-ion batteries, which face challenges related to resource scarcity and safety concerns, RFBs utilize liquid electrolytes (typically water-based), offering greater flexibility in material selection and system design.⁸ The performance of RFBs critically depends on the electrochemical properties of their electrolytes, including redox potential (thermodynamics), mass transport, and electron-transfer kinetics (k^0).⁹ High solubility of electrolytes enhances energy density, while stability ensures long-term operational viability.⁹ Redox flow batteries (RFBs) that are commercially available and in use today are based on the redox chemistry of transition metal elements like vanadium. Concerns have been raised about the environmental and biological impacts of vanadium, which could pose safety risks.⁶ Rapid commercialization of redox flow batteries has been hindered largely due to lower energy density of only 25–35 Wh L⁻¹, substantially lower than the >250 Wh L⁻¹ typical for lithium-ion batteries^{6,7}, cost, and environmental friendliness of the materials utilized in the device fabrication.¹⁰



Figure 1.1 Project, named Fifth Standard, is RWE's largest U.S. storage facility to date, at 137 megawatts (MW), and includes a 150-MW solar PV array expected to be complete in August. When fully energized, the facility, located in Fresno County, will have the capacity to power more than 26,000 homes (ref.11)

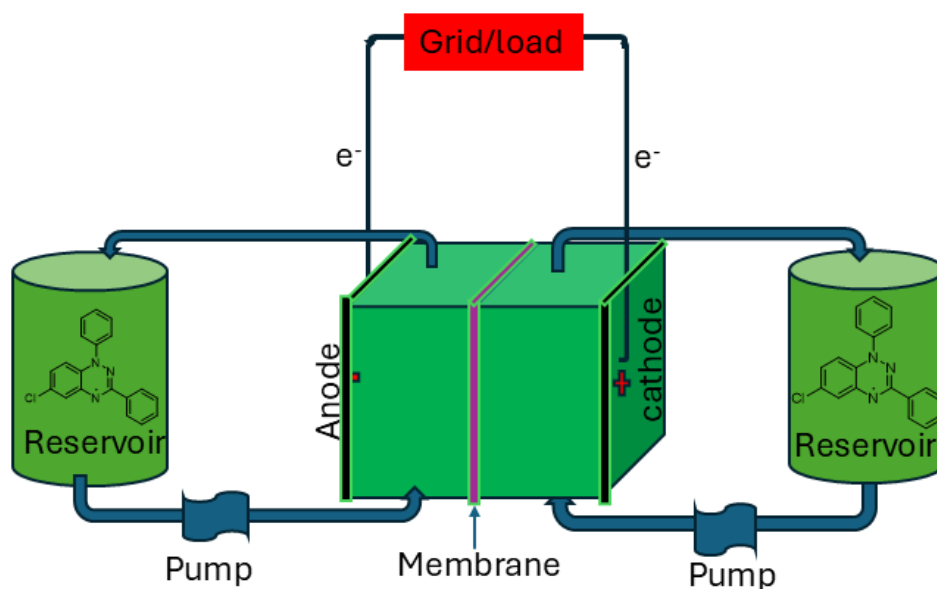
1.1 Working Principle of a Redox Flow Battery

A typical RFB contains two tanks in which the catholyte (redox active molecules dissolved in an electrolyte which gets oxidized at the anode during charging) and anolyte (redox active molecules dissolved in an electrolyte which gets reduced at the cathode during charging) are stored.⁴ Subsequently, these catholyte and anolytes are pumped into an electrochemical cell where they undergo oxidation and reduction. The electrochemical cell is fitted with positive and negative electrodes-which facilitate oxidation and reduction, with an intervening ion exchange membrane for ion migration and maintenance of charge neutrality in the cell. The cell voltage is defined as the difference between reduction and oxidation of the catholyte/anolyte and is dictated by innate structure of the redox materials. The power output of a redox flow battery, typically measured in kilowatts (kW), with some

large-scale systems reaching megawatts (MW), is dependent on two factors. The specific power output of a redox flow battery depends on the number of cell stacks and the electrolyte volume, which also determines the energy capacity (measured in kilowatt-hours (kWh)).⁴

Fundamentally, energy density of a battery system is dependent on the number of electrons involved, solubility of redox species, and the difference in electrochemical potential between the cathode and anode-active materials. Energy density is the most important performance metric for energy storage devices, and it relates to how much energy is stored in each volume.

Scheme 1. 1 Typical Operation and design of a redox flow battery



In an RFB system, the energy density is related to voltage and the number of electron processes, as is seen in the equation 1 below.¹²

$$\text{Energy density} = \frac{nCFV}{\mu_v} \quad \text{Equation 1}$$

where n is the number of electrons transferred in the reaction, C is the lower concentration of two electrolytes, F is Faraday's constant, V is the voltage of the battery, and μ_v is the volume factor ($\mu_v = 1 + \text{lower electrolyte concentration/higher electrolyte concentration}$). The energy density is directly proportional to number of electrons transferred-which correlates to the number of electron processes a material can provide, concentration (solubility) and voltage of the battery (which is directly related to the potential of the catholyte and anolyte).

Historically, the earliest redox flow battery patents involve the vanadium redox couple and titanium flow cell which were first registered as patents in France and Germany in 1933 and 1954 respectively¹³. Subsequently, NASA and other early researchers attempted using Fe/Cr to design RFBs in the early 80's, however, problems with poor reversibility of the chromium half-cell and challenges with developing an efficient ion selective membrane limited the performance of the RFB.¹⁴ The first reported commercial development of redox flow batteries employing vanadium in each half cell (VRB, Vanadium/vanadium Redox Battery) was demonstrated at the University of New South Wells (UNSW), AU, by Skyllas-Kazacos in 1986.¹⁵ The design of the battery utilized V(II)/V(III) and V(IV)/ V(V) couples as the anolyte and catholyte. Widespread adoption

of this device was unsuccessful due to toxic concerns with vanadium and the risk of V(II) being readily oxidized in the presence of air.¹⁴

1.2 Non-Aqueous Flow Batteries and Symmetric Redox Flow Batteries

Two types of redox flow battery designs exist: aqueous redox flow batteries (ARFBs) and non-aqueous flow batteries (NARFBs). Aqueous redox flow batteries are currently limited in use largely due to narrow electrochemical window of water (1.5V), and generally lower energy density of 20-50 W h/L.¹⁶ A non-aqueous flow battery is a type of energy storage battery that uses a non-water-based electrolyte like acetonitrile, propylene carbonate, and dimethyl sulfoxide to dissolve redox active organic molecules,¹⁷ unlike the aqueous flow battery systems that uses water-based electrolytes.^{18 4} All organic non aqueous redox flow batteries (A-ONRBs) are a recent development in RFBs. The non-aqueous redox flow battery idea was first proposed by Singh in 1984¹⁹. Experimental demonstration of a non-aqueous flow battery was made in 1988 when Matsuda et. al. used a tris(bipyridine)ruthenium(II) tetrafluoroborate complex $[\text{Ru}(\text{bpy})_3(\text{BF}_4)_2]$ in acetonitrile (CH_3CN) with tetraethylammonium tetrafluoroborate (TEABF_4) to design a RFB.²⁰ Non-aqueous redox flow batteries are particularly desired over their aqueous counterpart for wider voltage windows (up to 4V for most organic solvents)¹⁸, intrinsically faster electron-transfer kinetics⁴, and more extended working temperature ranges (up to -40°C).²¹

The concept of a “symmetric redox flow battery” refers to a type of flow battery where the catholyte and anolyte are made of the same redox-active species. They use only

organic materials, which are considered green and relatively inexpensive compared to vanadium. Current design of A-ONRBs involves the use of different anolytes and catholytes, separated by a porous separator commonly called a membrane.²² A separator membrane is important to discourage crossover of distinct active materials which has been reported to reduce capacity of A-ONRBs and also cause irreversible reductions in energy density²². To solve the issue of crossover of active materials, a proposal was made for use of singular bipolar redox active material in a symmetric flow battery system where the bipolar redox active molecule functions as both the anolyte and catholyte. All organic non aqueous redox flow batteries (A-ONRBs) have been reported to have cell potentials of up to 4V²³ which is comparable to 3.5V for lithium ion batteries.

While inorganic redox-active materials provide excellent stability and performance, their structures allow little space for modification. By contrast, organic redox active molecules offer rich molecular diversity and can be purpose-designed to tune properties²⁴, boost performance, and reduce costs.²⁵ Current research efforts are geared towards making structural modifications to available redox active molecules in order to improve the performance metrics of organic redox flow batteries.

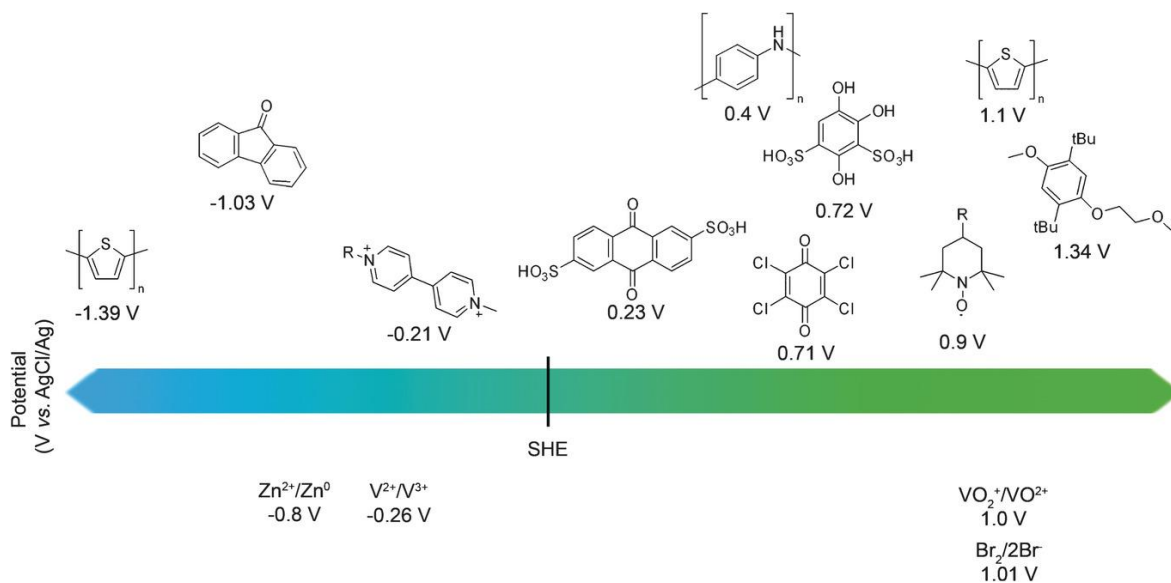
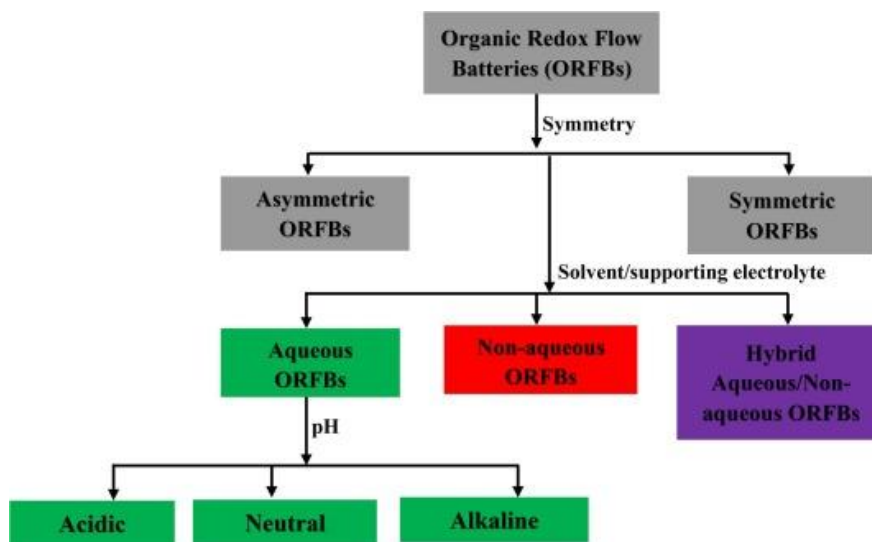


Figure 1. 2 Examples of organic redox active molecular systems utilized in charge storage materials, with the range of redox processes given in V vs Ag/AgCl. (Ref 15)

Organic redox flow batteries are broadly classified into asymmetric and symmetric systems which is based on redox material symmetry, followed by the solvent-based categorization into aqueous (further divided by pH), non-aqueous, and hybrid aqueous/non-aqueous systems.²⁶ Each category offers unique advantages and challenges, influencing their suitability for various energy storage applications. Aqueous ORFBs prioritize sustainability, non-aqueous ORFBs focus on performance, and hybrid systems seek a compromise, with ongoing research aimed at overcoming low solubility, membrane inefficient leading to cross over of ROMs and stability limitations. Among a wide variety of all organic non-aqueous redox flow batteries (A-ONRFBs) which include polymer redox flow battery (PRFB)²⁷, Li/ Polysulfide²⁸ etc., organic based electroactive compounds are

particularly desirable due to the structural diversity that can be introduced²⁹. Previously, redox active molecules such as quinone³⁰, nitroxides^{31,31-34}, ferrocene³⁵, viologen³⁶⁻³⁹, and phenothiazine⁴⁰⁻⁴² etc. , have been used in designing RFBs.

Scheme 1.2 Schematic of typical redox flow battery classifications (from ref 17)



1.3 Challenges in Organic Redox Flow Battery Technology

The global energy landscape is undergoing a transition from fossil fuels to renewable sources to address sustainability and environmental concerns. Renewable energy technologies such as solar and wind are abundant but intermittent, necessitating efficient energy storage systems to ensure a stable energy supply.^{26,43,44} Currently, vanadium-based electrolytes dominate the RFB market due to their proven performance; however, their high

cost and environmental impact have motivated research into organic redox-active materials such as TEMPO, quinones, and benzotriazinyl radicals.^{8,25,45}

Among these, benzotriazinyl radicals are promising candidates owing to their reversible redox chemistry, high stability, and tunable electrochemical properties.⁴⁶ Recently, Edwin Otten et al successfully designed a non-aqueous symmetric flow battery using benzotriazinyl radicals by functionalizing the C-3 phenyl ring using electron donating and withdrawing groups.¹⁰ This result provides proof of principle for the use of benzotriazinyl radicals in redox flow batteries. Despite these advantages, their application in flow systems remain underexplored.

1.4 1,3-Diphenyl-1,2,4-Benzotriazinyl - A Stable Organic Radical

Stable organic radicals have long been a subject of fascination in chemistry due to their unique electronic properties and potential applications in materials science, electronics, and medicinal chemistry⁴⁷. The historical context of stable organic radicals dates back to the early 20th century with the synthesis of the triphenylmethyl radical by Gomberg in 1900.⁴⁸ Since then, various classes of stable radicals have been discovered, including nitroxides, verdazyls, and, more recently, benzotriazinyl (“Blatter”) radicals.⁴⁹ First synthesized in 1968 by Blatter and Lukaszewski,⁵⁰ these radicals have garnered significant attention for their exceptional stability and versatility. Unlike many organic radicals that are highly reactive and require careful handling, Blatter radicals can be manipulated under ambient conditions in both solution and solid state using standard

organic chemistry techniques.⁵¹ The stability of benzotriazinyl radicals is attributed to stabilization of the unpaired electron due to spin delocalization within the benzotriazinyl ring system, as well as steric protection provided by the phenyl substituents at positions N-1 and C-3 phenyl rings.⁵¹

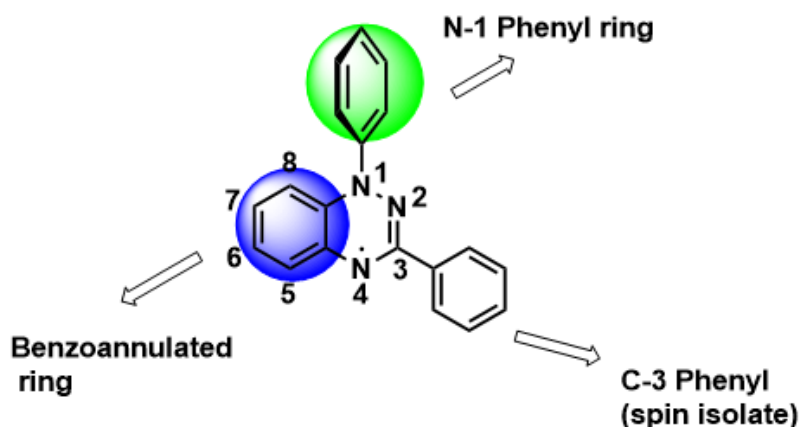


Figure 1.3 IUPAC numbering for parent BTR compound 1.0

Benzotriazinyl radicals are particularly notable for their ease of modification through substitution at the C-3, N1 phenyl, and benzo-annulated ring, which allows for tailoring their properties for specific applications.⁴⁶ This modifiability has opened up numerous possibilities for their use in functional materials, such as sensors⁵², spin labels, magnetic materials, liquid crystals, and charge storage materials.⁵¹

Tuning the substituents on the phenyl rings of benzotriazinyl radicals allows redox potential adjustment, improving energy density and cycling stability.⁴⁶ Previous studies

have focused on peripheral substitutions, demonstrating that electron-donating or -withdrawing groups modulate both the redox potentials and the spin distribution.^{46,51} Although some studies have investigated modifications to the benzoannulated section of the triazinyl core, particularly the 7-position, which is reported to block decomposition of benzotriazinyl radicals,⁵³ systematic and comprehensive functionalization at the sixth position remains much less developed. Notably, previous work by Oakley within the group explored electron-donating substitution at the 5-position and showed that the parent radical could be destabilized by certain functional groups, leading to changes in oxidation and reduction potential. His work confirmed that substitution influenced redox potentials without compromising reversibility.

1.5 Thesis goal

To tackle ongoing difficulties in the advancement of redox flow batteries (RFBs)—specifically concerning the enhancement of energy density, which is related to solubility of available redox active molecules, electrochemical tunability, and material stability—we have investigated a category of persistent redox-active and stable organic radicals: the 1,3-diphenyl-1,2,4-benzotriazinyl radical. These radicals offer highly adjustable electrochemical characteristics, rendering them a promising candidate for the improvement of charge storage capabilities. The structural flexibility of 1,3-diphenyl-1,2,4-benzotriazinyl radical enables them to operate effectively as both the catholyte and anolyte in redox flow batteries (RFBs), thereby potentially facilitating symmetric flow battery configurations and augmenting overall system efficiency.

Several critical gaps hinder the advancement of benzotriazinyl radicals as RFB electrolytes. First, the solubility of substituted radicals, which directly impacts energy density, has not been systematically characterized.⁴⁵ Second, electron-transfer kinetics (k^0) across different substituted derivatives remain poorly understood, limiting insights into their kinetic performance.⁵⁴ Third, the relationship between spin density—particularly at para positions relative to the N1 phenyl nitrogen—and electrochemical properties requires further elucidation.⁴⁶ Finally, existing studies have not thoroughly evaluated cycling stability, mass transport under dynamic conditions, or the long-term operational stability of these radicals in flow systems.⁵⁵

In this work, we extend functionalization to the 6-position of the benzotriazinyl core. This position is para to the position of highest spin density (the N1 position, *vide infra*) and is thus expected to significantly influence spin density distribution and therefore electronic structure and electrochemical behavior. The 6-position also offers synthetic accessibility through directed substitution of the benzo-annulated ring. By targeting this position, we aim to identify derivatives with enhanced solubility, reversible redox behavior, and favorable electron-transfer kinetics—key criteria for use in symmetric nonaqueous RFBs. We therefore set out to synthesize and characterize comprehensively, a series of 6-substituted benzotriazinyl radicals bearing electron-donating and electron-withdrawing groups. We evaluate how substitutions at this position affect optical absorption, EPR hyperfine coupling, redox potentials, and electron-transfer kinetics. As an application, we were interested in assessing these radicals in the context of nonaqueous flow battery design, focusing on how substituents impact cell voltage, energy density and kinetic performance.

This approach enables structure-property relationships to be mapped for benzotriazinyl radicals beyond previously studied substitution patterns.

1.6 Specific Aims

This study aims to carry out a systematic investigation of substituted benzotriazinyl radicals as RFB electrolytes.

The aims of this project are:

- 1) To prepare a series of 6-substituted radicals that include electron withdrawing and electron donating groups and measure their redox potentials and to correlate structure with redox processes.
- 2) To correlate electronic absorption spectroscopy, EPR and computation with structure to understand the effect of substitution on these open shell systems, which may or may not behave as closed shell systems in terms of substituents effects.
- 3) To determine how substitution affects the electrochemical behavior in terms of reversibility of redox processes and electron-transfer kinetics. The electron transfer rate constants (k^0) will be determined through electrochemical impedance spectroscopy to evaluate kinetic performance, and reversibility through cyclic voltammetry experiments.

By integrating these analyses, this work aims to provide a comprehensive evaluation of 6-substituted benzotriazinyl radicals, facilitating their development as sustainable and efficient electrolytes for RFB applications.

1.7 Thesis scope and organization

This thesis investigates the design, synthesis, and electrochemical characterization of a new series of 6-position functionalized 1,3-diphenyl-1,2,4-benzotriazinyl (BTR) radicals for application in nonaqueous symmetric redox flow batteries (RFBs). By introducing both electron-donating and electron-withdrawing groups at the 6-position of the benzotriazinyl ring, the study aims to elucidate how substituent effects influence redox potentials, spin delocalization, solubility, and electron-transfer kinetics. Particular emphasis is placed on understanding how these parameters affect reversibility, stability, and redox accessibility, all of which are critical for their use as organic redox-active electrolytes.

A comprehensive suite of techniques—including UV-Vis absorption spectroscopy, continuous-wave X-band electron paramagnetic resonance (EPR), cyclic voltammetry (CV), and single-crystal X-ray diffraction (SCXRD)—is employed to investigate the structure–property relationships of the functionalized radicals. Electrochemical analyses include both thermodynamic (redox potential) and kinetic (heterogeneous rate constant, k^0) evaluations, with diffusion coefficients determined from the Randles-Sevcik equation. Spin distribution is analyzed using McConnell’s relationship via hyperfine coupling constants from EPR spectra, further supported by DFT calculations. Notably, structural

characterization of a rare 8-amino-functionalized leuco radical intermediate is achieved via SCXRD, offering new insight into oxidation pathways and radical stabilization mechanisms.

This thesis is organized as follows:

Chapter 1 introduces the broader context of grid-scale electrochemical energy storage, with an emphasis on redox flow batteries and their advantages over other technologies. The chapter provides a technical overview of the redox flow battery architecture, challenges associated with current aqueous and nonaqueous systems, and a rationale for pursuing benzotriazinyl radicals as tunable bipolar materials. The thesis goal and specific research objectives are also clearly defined.

Chapter 2 details the synthetic routes used to access six new functionalized BTR derivatives via oxidative ring closure and modular approaches. It presents structural and electronic characterization through spectroscopy and computation, with a focus on correlating substituent effects with radical stability and redox behavior. CV is used to evaluate redox reversibility, estimate kinetic parameters, and quantify diffusion coefficients. Crystallographic analysis provides atomic-level insight into molecular planarity, packing, and potential steric hindrance. The chapter culminates in a discussion of how molecular design influences electrochemical performance and how specific substituents modulate charge transfer dynamics.

Chapter 3 summarizes the major findings of the work and outlines future directions. Potential improvements for redox-active molecule design—such as enhancing solubility,

tuning redox potentials beyond 1.0 V, and modifying core frameworks—are discussed. Recommendations are made for integrating functionalized BTR derivatives into prototype RFB systems and for extending this research toward polymeric or dimeric radical systems for enhanced charge storage performance.

Together, these chapters provide a foundational understanding of how structural modifications to the BTR core influence redox performance and assists future development of high-performance organic electrolytes in next-generation redox flow batteries

Chapter 2. Synthesis and Characterization of 6-Substituted 1,3-Diphenyl-1,2,4-benzotriazinyl Derivatives

2.1. Stable Organic Radicals

Several classes of stable organic radicals have been prepared and studied as spin carriers in both metal-radical networks⁴⁶ for organic electronic materials⁵⁶, spintronics⁵⁷, charge storage⁵⁸, and quantum science.⁵⁹ The overall electronic structure and physical properties of organic radicals are dictated by (i) molecular topology of the radical, (ii) molecular conformation, and (iii) the packing of the molecules in the solid or crystalline state. The distinct classes of stable organic radicals are comprised of carbon-based radicals (triarylmethyl **2.1**),⁶⁰ oxyl radicals (phenoxyl **2.2** and galvinoxyl **2.3**),^{61,62} nitrogen-based radicals (triarylaminyll **2.4**⁶³ and verdazyl **2.5**⁶⁴), aminoxyl radicals (nitroxide **2.6**⁶⁵ and nitronyl nitroxide **2.7**⁶⁶), and thiazyl radicals **2.8**,⁶⁷ which differ in relative stability, spin density distribution, packing motif, and topology (see Figure 1.4). Whereas the electronic structure, reactivity and properties of closed shell organic materials are typically characterized by the frontier orbitals, the HOMO (highest occupied molecular orbital) and the LUMO (lowest unoccupied molecular orbital), open-shell systems are characterized by the SOMO (singly occupied molecular orbital in the restricted Hartree-fock model). The SOMOs of these classes of organic radicals tend to be highly localized on the heteroatoms due to both increased electronegativity of the heteroatom and twisting out of plane of corresponding aryl substituents, which allow for kinetic stabilization. Intermolecular

magnetic exchange interactions almost exclusively occur through radical-radical contacts in the solid state.

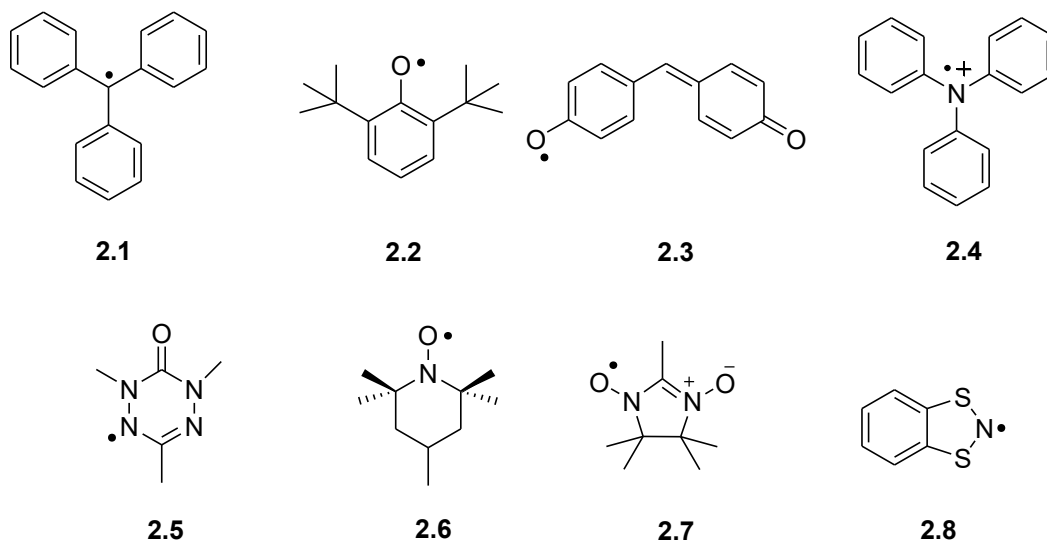


Figure 1.4 Stable organic radical classes

The earliest work on stable organic radicals began with the triarylmethyl radical **2.1** first prepared by Gomberg in 1900,⁶⁸ though not in its free radical state until many decades later due to its instability towards dimerization. At 5 °C in benzene, triarylmethyl radical exists in only 2-3% as the dissociated radical⁶⁹ and requires substitution with electron donating groups or extended conjugation in the *para* positions to achieve higher stabilities of the corresponding radical (*i.e.*, $(p\text{-OCH}_3\text{C}_6\text{H}_4)_3\text{C}\cdot$) exists as 100% dissociated in benzene at 100 °C).¹²⁶ The spin density distribution is such that 30% is centered on the central atom, with ~8% spin density on the *ortho* and *para* carbons of the phenyl substituents. The parent radical exhibits a reversible reduction process at -1.2 V, and an irreversible oxidation process at 0.57 V (vs Ag/AgI in DME).⁷⁰ Considerable stability is gained upon

perchlorination of the triarylmethyl radicals,(refs) with little perturbation of the spin density distribution.

Phenoxy radicals (**2.2**) are oxygen-centered, with the majority of spin density located on the heteroatom.⁷¹ Usually, a bulky substituent must be present at the *ortho* position to prevent decomposition of the radical. Galvinoxyl (**2.3**) is a typical example of phenoxy radicals showing bulk weak ferromagnetic exchange.⁶¹ There have been a number of papers using phenoxy radical as building blocks for pure organic polyradicals.⁷²⁻⁷⁸ Galvinoxyls have been used as anodic materials for organic radical batteries, leading to the preparation of the first fully organic battery, albeit with a low cell voltage of about 0.3V.⁷⁹ Substitution of the central carbon with the electronegative nitrogen leads to the triarylamines, which upon one electron oxidation leads to the triarylaminy radical cation (**2.4**). In general, the triarylaminy radicals are more air stable and thermally stable than the triarylmethyl radicals and are stabilized by electron donating groups or extended conjugation in the *para* position. X-ray crystallography reveals a propeller-like geometry with dihedral angles of roughly 30-40°.⁸⁰ EPR suggests little perturbation of the spin density distribution upon substitution with nitrogen.

Verdazyls (**2.5**) are another class of stable radicals extensively exploited. Numerous of substituted verdazyl radicals have been investigated so far, and magnetic properties vary from weak ferromagnetism to antiferromagnetism as well as spin-Peierls transitions.¹⁹ The spin density is primarily located on the four nitrogens with a node in the SOMO at C3. Verdazyls have been used for charge storage, in which verdazyl polymers have been investigated that exhibit ambipolar redox activity, high radical density, and good stability.⁸¹

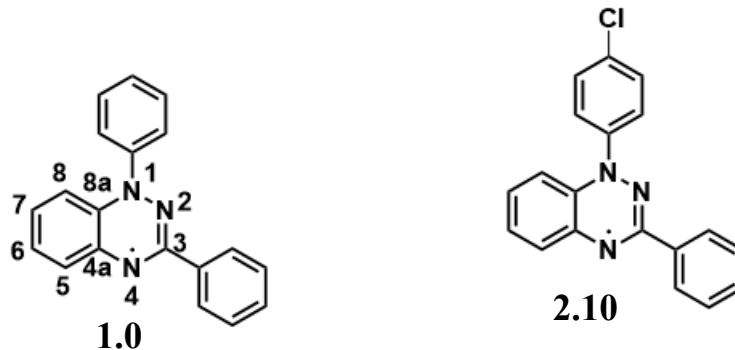
The nitroxide (**2.6**) and nitronyl nitroxide (**2.7**) radicals have been most extensively exploited by chemists⁸², *p*-Nitrophenyl nitronyl nitroxide (β phase) is the first example of a genuine bulk organic ferromagnet, which was discovered by Kinoshita in 1991.⁶⁶ Both have stable electron configurations which in part are attributed to π -conjugation in extended aromatic systems or steric shielding by bulky *ortho* substituents. In nitronyl nitroxides, the unpaired spin can be delocalized into two N-O groups with a node on the central carbon atom. Currently many efforts are made to incorporate nitroxides into polymeric backbones, and the first and most successful organic radical batteries are comprised of polymethylmethacrylate nitroxide polymers, which serve as the cathodic materials in a lithium battery configuration, with cell voltages of ~ 3.4 V and specific capacities of around 110 mAh/g.⁸³

Sulfur based thiazyl radicals include thioaminyl, dithiazoyl, dithiadiazolyl, and thiatriazinyl derivatives.¹⁹ In contrast to nitroxides, thiazyls usually show high transition temperatures and a tendency toward dimerization through S-S contacts. It was found that *p*-NC(C₆F₄)(CNSSN) is one of the pure organic ferromagnets with the highest T_c (36 K) observed so far.⁸⁴ Structure-property correlations have been extensively investigated, but few cases have been reported in which they have been used as building blocks for polymeric materials.

2.2. The 1,3-Diphenyl-1,2,4-benzotriazin-4-yl (DPBT) Radical

The parent radical, 1,3-diphenyl-1,4-dihydrobenzo[*e*][1,2,4]triazinyl (IUPAC) or 1,3-diphenyl-1,2,4-benzotriazinyl (DPBT, **1.0**) was first synthesized by Blatter in 1968⁵⁰, and

was found to exhibit high thermal and chemical stability under ambient conditions.⁴⁶ Early work focused on the biological and materials properties of the radical, in which it was found that the benzotriazinyl (BT) radical could be used as a polymerization inhibitor⁸⁵ and photographic sensitizer⁸⁶. In addition, it was found that its quaternary salts could be used as disinfectants due to their antibacterial or antifungal properties, which has led to a number of patents.⁸⁷ Waldrep found that the parent precursor, 1,4-dihydrobenzo[*e*][1,2,4]triazine and its derivatives exhibit a significant degree of herbicidal activity that is lost upon oxidation to the radical form or alkylation at C6.⁸⁸



Early spectroscopic studies of **1.0** support a delocalized electronic structure, giving rise to a complicated absorption and unusual EPR spectra. The absorption spectrum of **1.0** exhibits several low-intensity bands in the UV region at $\lambda_{\text{max}} = 267, 320, \text{ and } 370 \text{ nm}$ and visible region at $\lambda_{\text{max}} = 420, 490 \text{ and } 550 \text{ nm}$ ⁸⁹⁻⁹¹, suggesting several low-lying transitions⁹².

Kadirov and Neugebauer successfully used electron-nuclear double resonance (ENDOR) to assign EPR hyperfine splitting's, suggesting that the spin density distribution is fairly delocalized with 26.0% on N1, 17.8% on N2, and 17.8% on N4.^{91,93-95} Note that the

resonance structure typically drawn for the BTR radical represents the unpaired electron on N4, when ENDOR reveals that the highest spin density is in fact on N1. This is due to the fact that the electronic structure of the radical has multiconfigurational character. The electronic structure can be represented by three resonance structures (I-III), in which the zwitterionic form reveals higher spin density at N1. This is important and typically not properly represented in the vast literature and recent studies published on this system.

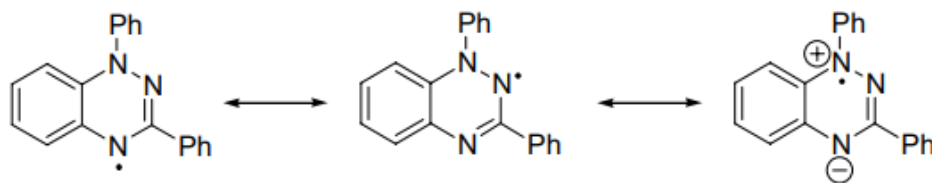


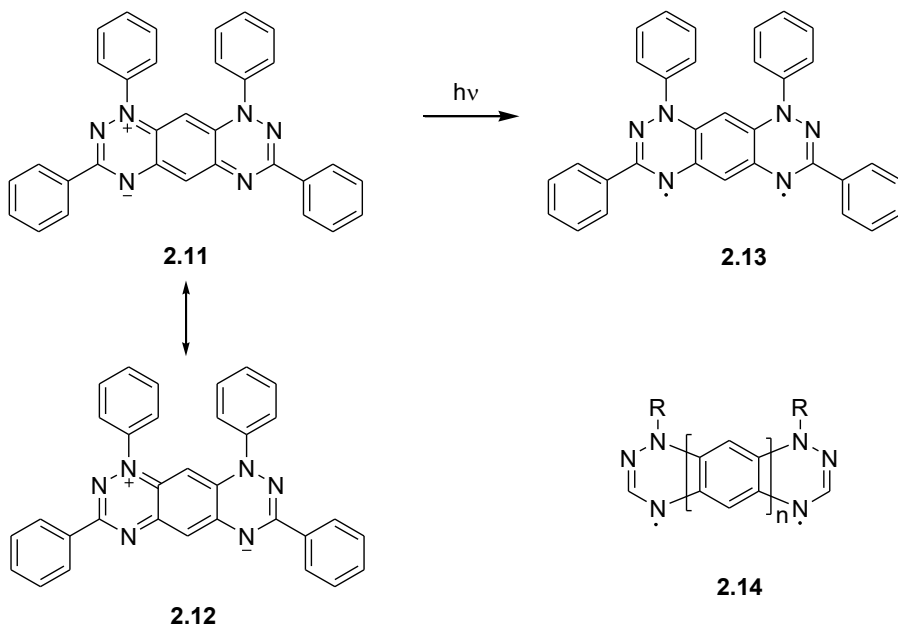
Figure 1.5 Resonance structures of 1.0

In 1980, Neugebauer *et al.* developed an alternate synthetic methodology to **1.0**,⁹¹ allowing full characterization of this radical and its derivatives.^{96–98} X-ray crystallography reveals a planar structure with the N1-phenyl substituent twisted out of plane with a dihedral angle of 56° .¹⁶² In general, the radical packs in 1-D slipped π -stacks in the crystalline state which successfully accounts for the weak bulk antiferromagnetic exchange observed in the solid state.^{91,96,98} In addition, 1-(4-chlorophenyl)-3-phenyl derivative (CDPB, **2.10**) was found to exhibit unusually strong antiferromagnetic exchange ($2J_1/k = -220$ K) due to the formation of 1-D π -stacks.⁹⁶

Electrochemical measurements reveal that the radical is an extremely good electron donor and acceptor, with a reversible one-electron oxidation at 0.103 V vs SCE, and a reversible one-electron reduction at -0.960 V vs SCE.¹⁵⁸ By utilizing the strong electron

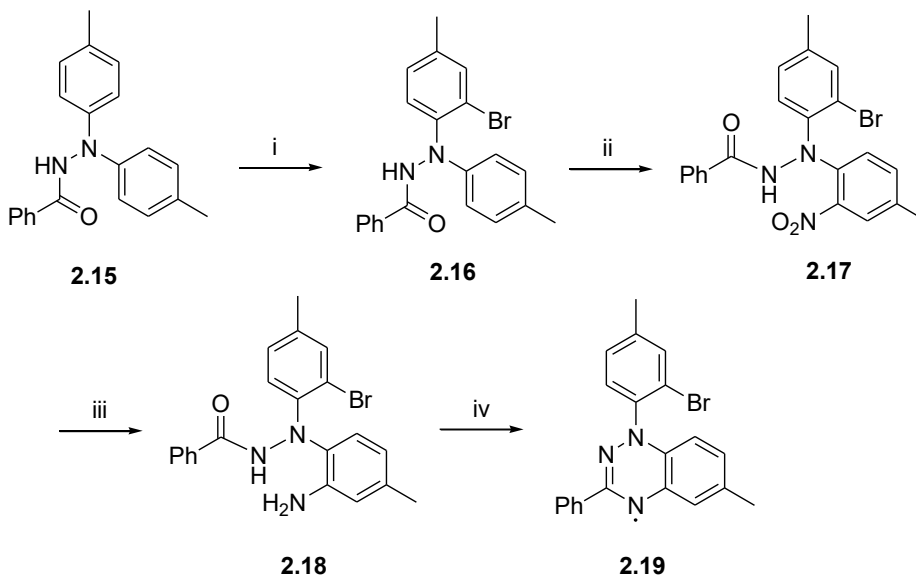
donating ability of **1.0**, Hutchison prepared a novel pressure sensitive organic charge transfer salt by combining with TCNQ (a good acceptor) to yield a 5:2 salt: $(\text{TCNQ})_5(\text{DPBT})_2$.¹⁶⁴ The salt forms $(\text{TCNQ})_2$ layers which consist of a pair of two dimers separated by a “skewed” TCNQ in the solid state. Electrical conductivity measurements revealed that the salt was a pressure dependent semiconductor with $\sigma_{\text{cp}} = 10^{-4} \text{ S}\cdot\text{cm}^{-1}$ at the ambient conditions, and σ_{a} increased by approximately two orders of magnitude when the pressure was increased from 1.8 to 2.1 Kbar at room temperature.^{89,99}

The effect of conjugation and annulene topology on a bistriazinyl biradical has been investigated via the preparation of a fused dimer – tetraphenylhexaazaanthracene (TPHA, **2.11**).¹⁶⁵ Spectroscopic measurements (NMR, UV-Vis, and emission) and theoretical work suggest that the molecule exists as a zwitterionic closed shell singlet state in the ground state, with a singlet-triplet gap of 18.9 kcal/mol.^{89,100}



Overall, out of the various classes of organic radicals discussed, the benzotriazinyl radicals are unique in their combined spin delocalized structure, and good electron donating/accepting ability.

Scheme 2.1 Blatter Synthesis (Route A)^a

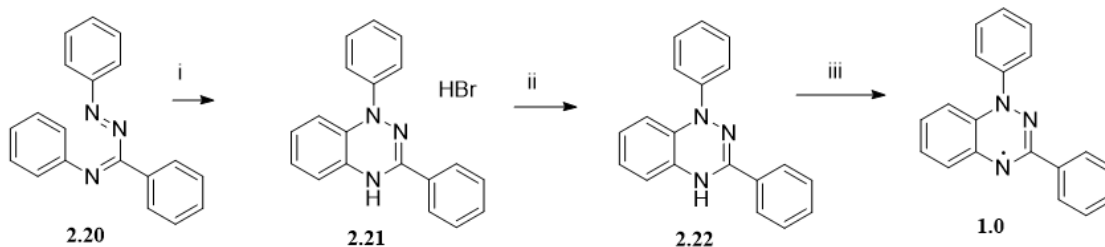


^a *Reagents and Conditions:* (i) Br₂/CH₂Cl₂, KOH; (ii) HNO₃, acetone; (iii) Pd/C, H₂, EtOH, 78%; (iv) EtOH, reflux; KOH, 59%.

The Blatter synthesis¹⁵² Route A (Scheme 2.1) involves bromination of the 2',2'-bis(*p*-tolyl) benzoylhydrazide (**2.15**) in “fair” yield with bromine and potassium hydroxide in CH₂Cl₂ to give the monobrominated hydrazide **2.16**. Mononitration was achieved by treatment with one equivalent of nitric acid in cold acetone to give **2.17**, followed by reduction with hydrogen over 10% Pd/C to give the aminohydrazide **2.18** in 78% yield.

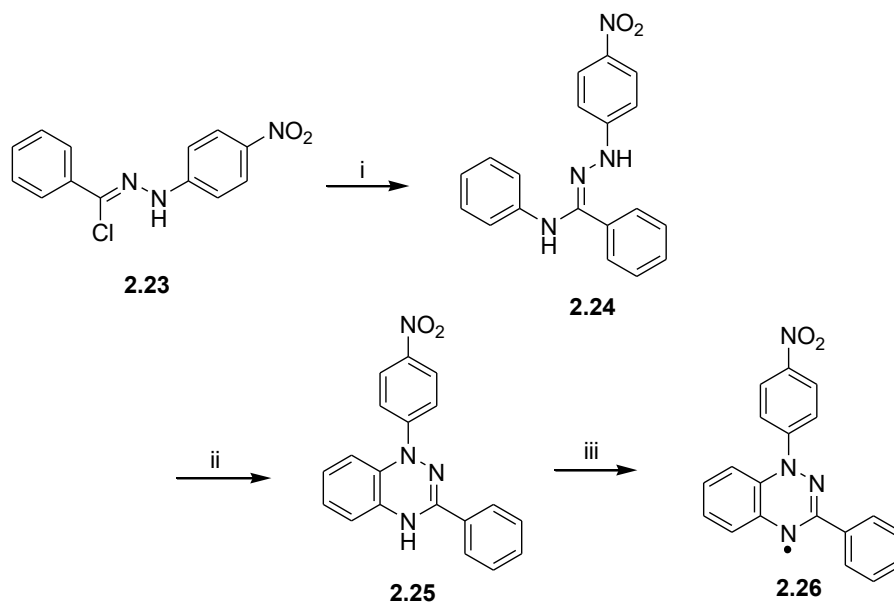
Heating of **2.18** in ethanol to reflux with potassium hydroxide yielded the diarylbenzotriazinyl radical **2.19** as “beautiful black” crystals (m.p.123-125°) in 59% yield.

Scheme 2.2 Blatter Synthesis (Route B)^a



^a *Reagents and Conditions:* (i) HBr, (CH₃)₂CHOH, 22 °C, 70%; (ii) NaHCO₃ or KOH, C₂H₅OH; (iii) O₂.

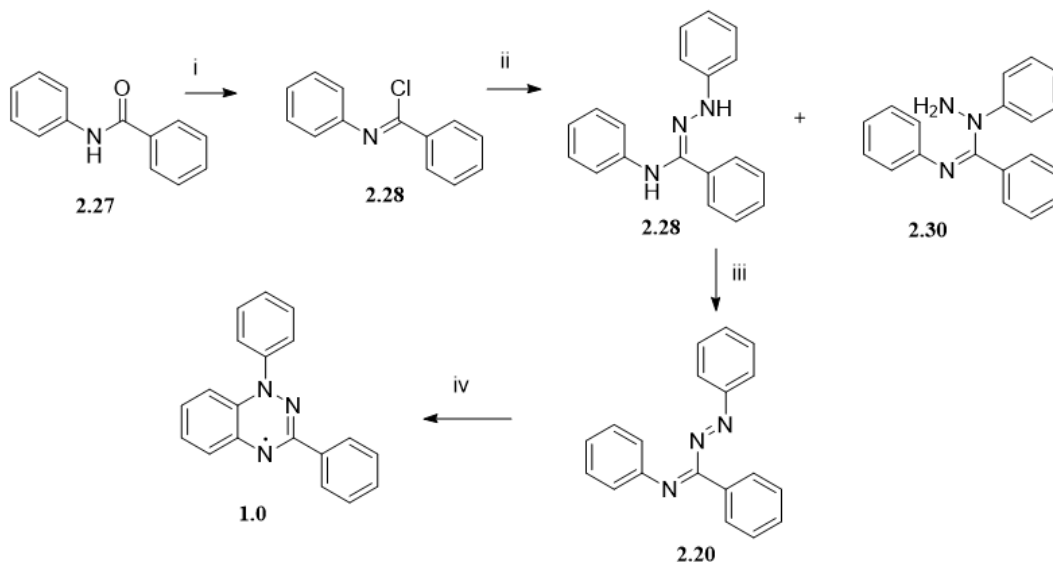
An alternative route developed by Blatter is the most widely used synthetic methodology for **1.0** and is shown in Scheme 2.2. The critical radical forming step, which differs significantly from Route A, involves oxidation and ring closure to yield the radical from an amidrazone. Both formation of the amidrazone and the following cyclization can be difficult and low yielding synthetic steps, leading to low overall yield of the final radical product. The synthesis involves ring closure of the imidrazonane **2.20** with HBr in isopropanol to yield the HBr salt of the triazine **2.21** in 70% yield. Treatment with base yields the reduced radical **2.22**, which under exposure to oxygen undergoes immediate oxidation to the final radical **1.0** in quantitative yield.^{152, 153}

Scheme 2.3 Kadirov synthesis (Route C)^a

^a *Reagents and Conditions:* (i) aniline, TEA, 90%; (ii) Ag₂O, 63%; (iii) Ag₂O, reflux, 40-50%.

Kadirov developed an alternate route (Scheme 2.3) in which a chlorohydrazone **2.23** undergoes a base-catalyzed substitution of aniline to give **2.24**, followed by oxidative cyclization with silver oxide to give **2.25**. The benzotriazine **2.25** was further treated with silver oxide for 1-2 days to give final radical **2.26**. However, we found that silver oxide and mercury oxide was only applicable to a limited class of amidrazones for radical generation.

Scheme 2.4 Neugebauer synthesis (Route D)^a



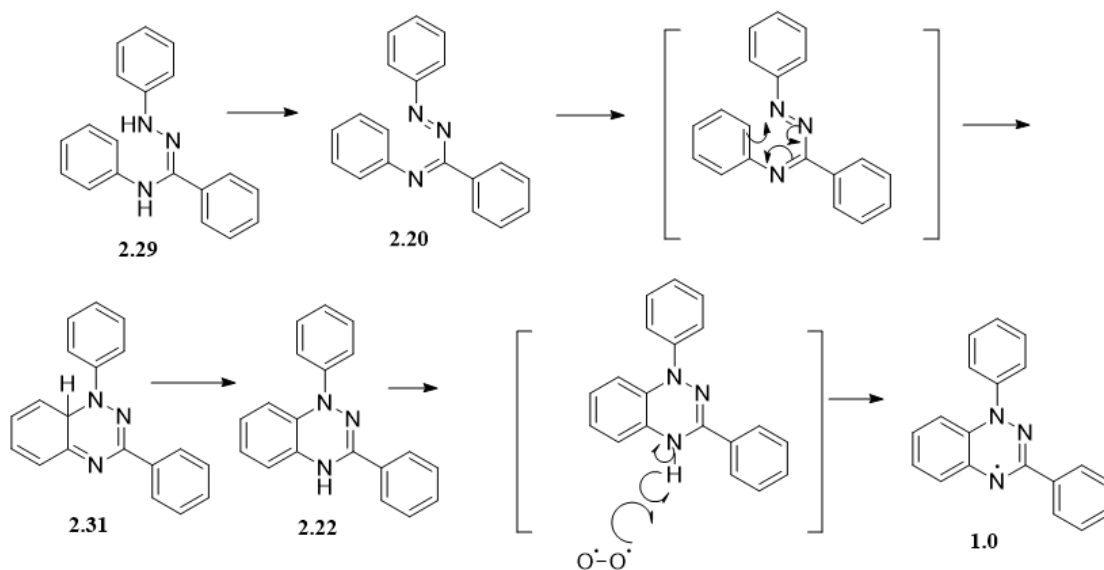
^a *Reagents and conditions:* (i) PCl₅, reflux, 3 h; (ii) phenylhydrazine, 22 °C, 12 h, 36%; (iii) HgO, ethanol, reflux, 1 h; (iv) O₂, 22 °C, 4 d, 51%.

The synthesis developed by Neugebauer^{156-158, 167} (Scheme 2.4) begins with the conversion of a benzamide (**2.27**) to the N-phenylbenzimidoyl chloride (**2.28**) based on a procedure developed by Wallach in which the benzamide is heated to reflux with phosphorus pentachloride to give the chloroimine, which is directly used in the next step without further purification.¹⁶⁸ Condensation of **2.28** with phenylhydrazine occurs via nucleophilic attack of either N1 or N2 of phenylhydrazine gives isomeric products **2.29** and **2.30**. The relative rate of formation of both isomers is comparable, leading to a low yield (36%) of the desired isomer **2.29**. Oxidation of amidrazone **2.29** with mercury(II)

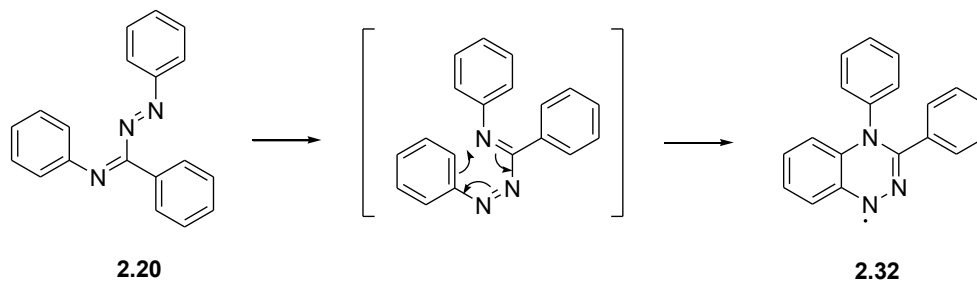
oxide gives the imidrazone **2.20** followed by exposure to O₂ over several days leads to the radical **1.0** in 51% yield from the amidrazone **2.29**.¹⁵⁶

The parent radical **1.0** was initially synthesized in our lab according to Neugebauer's methodology with slight modification. In the first step, benzanilide (**2.27**) was treated with phosphorus pentachloride at room temperature and refluxed for 3 hours to yield N-phenylbenzimidoyl chloride **2.28**. After the removal of POCl₃ by distillation, the resultant residue was directly subject to amidrazone formation by condensation with phenylhydrazine in hexanes at room temperature to yield **2.29** cleanly in 43% yield. Treatment of the amidrazone **2.29** with mercury oxide in ethanol at reflux for 1 hour under anaerobic conditions led to the imidrazone **2.20**. Removal of the reduced mercury oxide by filtration, followed by exposure to oxygen for 4 days led to formation of radical **1.0** in 89% yield from amidrazone **2.29**.

The ring-closure step is effectively a formal oxidation, followed by cyclization and re-aromatization as shown in Scheme 2.5. Although the mechanism has not been experimentally investigated, the proposed mechanism upon oxidation by mercury (II) oxide involves initial oxidation of the amidrazone **2.29** to an imidrazone **2.20**. An imidrazone analog has in fact been isolated and fully characterized by ¹H NMR and IR in our lab. The imidrazone **2.20** then undergoes a 1,6-electrocyclic ring closure through an asymmetric disrotatory process to yield an intermediate **2.31**, which re-aromatizes to form triazine **2.22** through a [1,5]-sigmatropic rearrangement.^{171, 172} This approach was substantiated by the formation of nitro-substituted triazine observed by Kadirov (Scheme 2.3).¹⁶⁰ The radical precursor **2.22** is finally oxidized by O₂ to yield radical **1.0**.

Scheme 2.5 Proposed mechanism of oxidative radical formation.

It is worthy to note that a radical isomer **2.32** was isolated by Zverev in the conversion of **2.20** to radical **1.0**.^{171, 173} The formation of this side product involves the attack of the imine N4 atom on the azo phenyl ring (N1 phenyl ring) as illustrated in Scheme 2.6. Buzykin suggests that **2.32** is a minor product due to the hindered approach of the N1 nitrogen.¹⁷¹

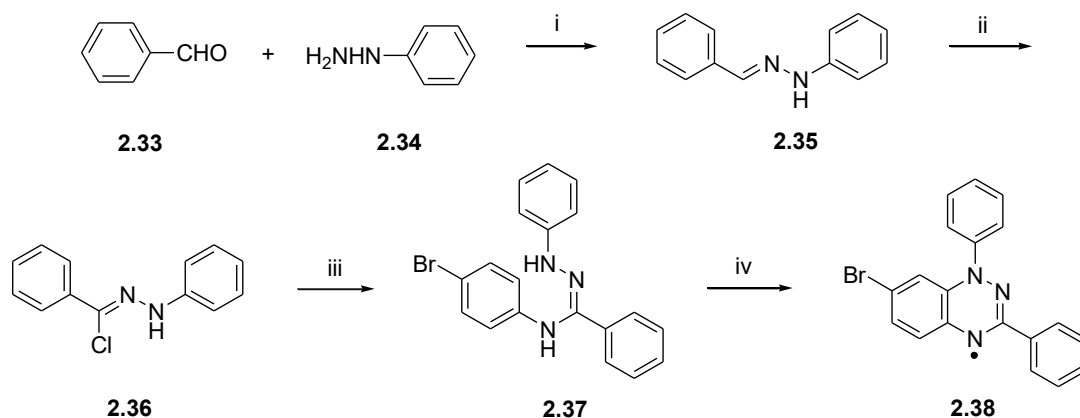
Scheme 2.6 The mechanism for the formation of 2.32.

The earlier syntheses of **1.0** developed by Neugebauer *et al.* and repeated in our lab involve conversion of a benzanilide (**2.27**) to the N-phenylbenzimidoyl chloride (**2.28**) in the presence of phosphorus pentachloride. The difficulties in isolation of the imidoyl chloride due to moisture sensitivity, the strong oxidative conditions of chlorination, and the low yield of amidrazone formation due to poor regioselectivity render this synthetic methodology undesirable for the synthesis of functionalized DPBT radicals. An alternate synthetic methodology for DPBT derivatives was therefore developed in our lab in which the desired radicals can be prepared in high yield and purity under mild conditions as shown in Scheme 2.7. The use of mild conditions is necessitated by the need to install functionality in the benzotriazinyl moiety for polymer generation, and a route which exhibits high tolerance to a wide range of functionality was therefore necessary.

Functionalized 1,2,4-benzotriazinyl radicals were synthesized according to a linear synthetic approach in which the functionality of interest is introduced into the amidrazone core **2.37** under mild and neutral conditions, as shown in Scheme 2.7. This approach began with the preparation of the hydrazone **2.35**. Condensation of benzaldehyde **2.33** and phenylhydrazine **2.34** in benzene gave the hydrazone **2.35** in 72% yield.¹⁷⁴ Chlorination of **2.35** with the Corey-Kim reagent, NCS/(CH₃)₂S at -78 °C, followed by purification via chromatography gave **2.36** in 73% yield. The chlorohydrazone **2.36** underwent condensation with aniline with base (TEA) catalysis in refluxing ethanol to give the amidrazone **2.37** in 36% yield. Isolation and purification of the amidrazone **2.37** by column chromatography is possible but has been found to result in low yields due to acid-catalyzed decomposition on silica gel. As a result, the crude amidrazone is typically subjected to flash

chromatography on a short column and taken on to the next synthetic transformation directly. It was found that HgO failed in initiating the ring closure of **2.37**. Addition of DBU to a solution of amidrazone in aerated ethanol led to radical formation as evidenced by the formation of a brown solution. The resulting radical was purified by flash chromatography on silica gel, followed by recrystallization from CH₂Cl₂/hexanes (~1:1) to give **2.38** as a brown-black polycrystalline solid in 62% yield.

Scheme 2.7 Synthesis of 7-bromo-1,3-diphenyl-1,2,4-benzotriazin-4-yl (**2.38**) (Route E)^a



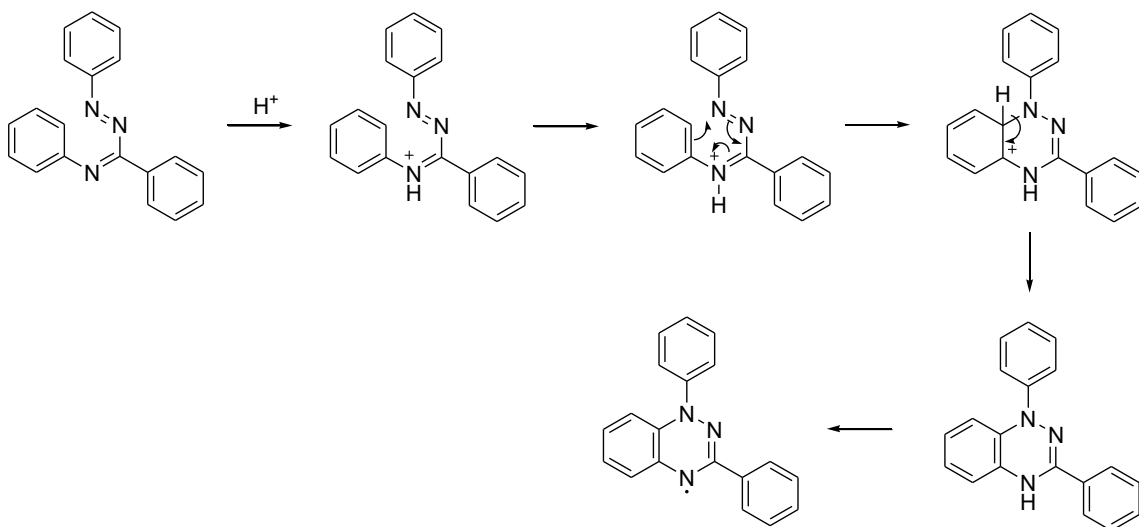
^a *Reagents and conditions:* (i) Benzene, 22 °C, 6 h, 72%; (ii) NCS, (CH₃)₂S, -78 °C, CH₂Cl₂, 1 h, 73%; (iii) 4-Bromoaniline, TEA, ethanol, 78 °C, 3 h, 36%; (iv) DBU, ethanol, 22 °C, 12 h, 62%.

The radical formation step deserves some discussion as this is typically the yield-limiting step. Radical formation has been found to be catalyzed by HgO in the presence of O₂, HBr, and DBU, thus oxidative, acidic (oxidative) and basic conditions all catalyze the same reaction depending on the substrate. It is believed that all three reagents aid in the generation of the imidrazone, which then cyclizes by 1,6-electrocyclic ring closure. Acid-

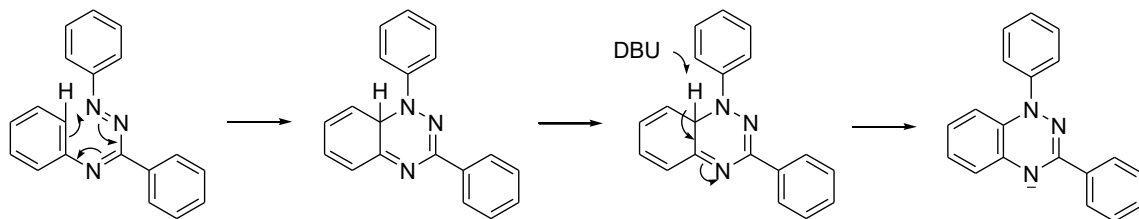
catalysis by HBr may involve initial generation of the protonated imidrazone, followed by 1,6-electrocyclization as shown in Scheme 2.8. Protonation of the carbon-nitrogen double bond at N4 is likely to lead to activation for cyclization, facilitating the ring closure. Radical formation with DBU may occur as shown in Scheme 2.8 in which DBU may assist in the re-aromatization step.

Scheme 2.8 Proposed mechanism of base and acid-catalyzed radical formation

Acid-catalyzed radical formation



Base-catalyzed radical formation



In this work, series of 6-substituted DPBT derivatives were successfully synthesized by slight modification of the procedure described in route E (Figure 2.1). The derivatives, 8-Amino-1,3-diphenyl-1,2,4-benzotriazinyl-4yl (**1.1**), , 6-Chloro-1,3-diphenyl-1,2,4-benzotriazinyl-4yl (**1.4**), , 6-Methyl-1,3-diphenyl-1,2,4-benzotriazinyl-4yl (**1.3**), , 6-Nitro-1,3-diphenyl-1,2,4-benzotriazinyl-4yl (**1.5**), , 6-Methoxy-1,3-diphenyl-1,2,4-benzotriazinyl-4yl (**1.2**), were synthesized according to Scheme 2.9 to yield blue for 1.1 and brown-black solids in 35-60% yield.

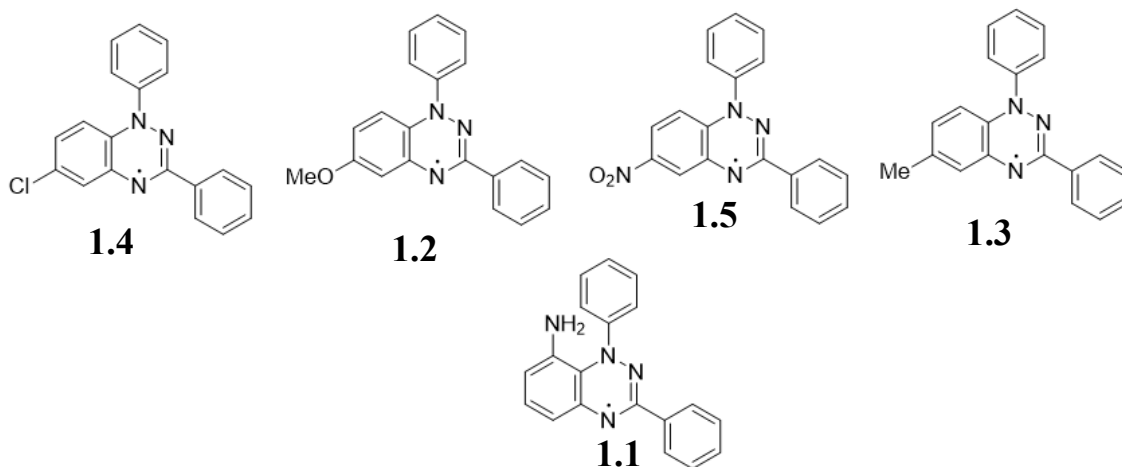


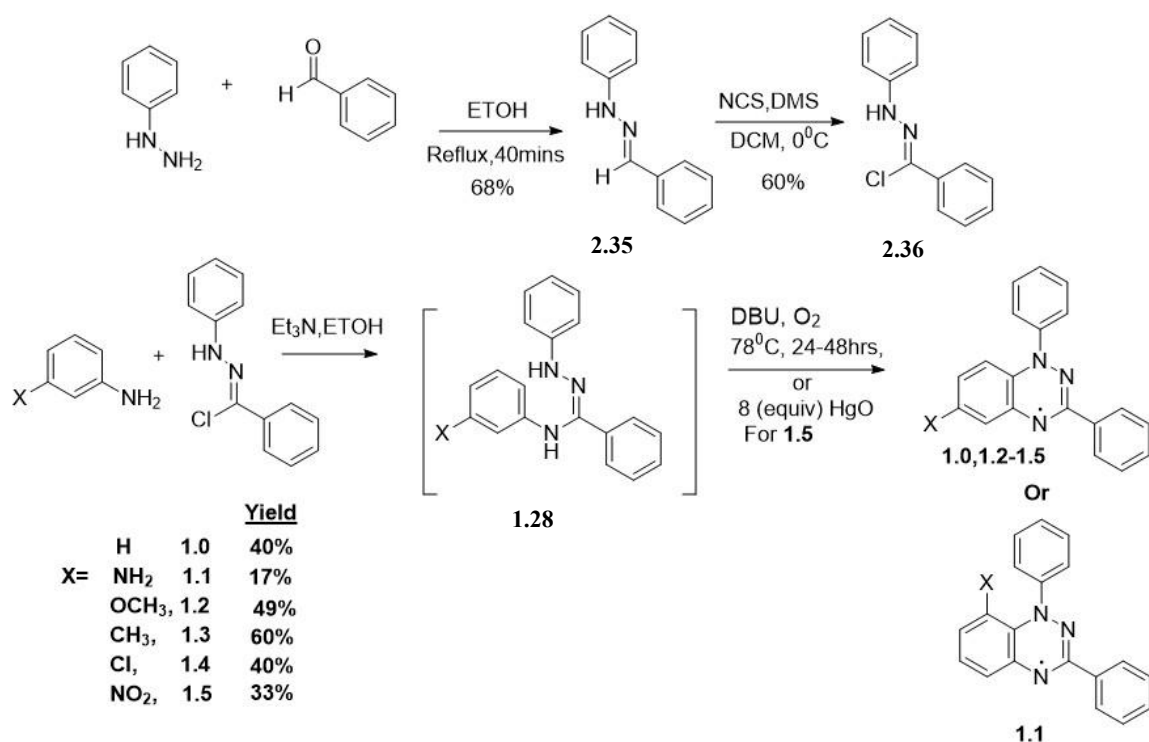
Figure 2.1 DPBT derivatives **1.1-1.5** were synthesized according to Route E.

2.3 Results and discussion

2.3.1 Synthesis of 6-substituted derivatives 1.1-1.5

The benzotriazinyl radicals investigated in this project were synthesized using the general approach illustrated in Scheme 2.9

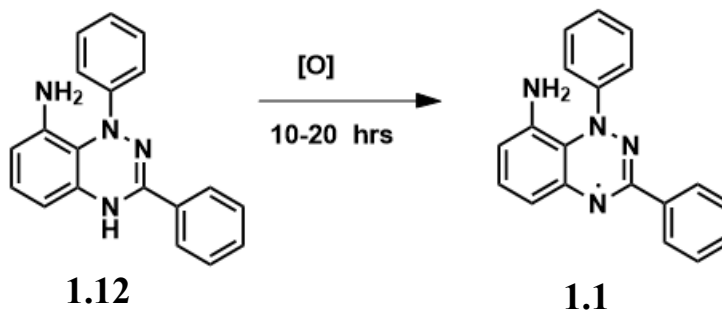
Scheme 2.9 Synthesis of radical 1.1-1.5



The radical 1,3-diphenyl-1,2,4-benzotriazinyl-4-yl (**1.0**) was prepared via the synthetic route shown in Scheme 2.9. The benzaldehyde was condensed with phenylhydrazine at room temperature in ethanol to afford hydrazone **2.35** in 68% yield. Treatment with the Corey-Kim reagent at -78°C resulted in chlorohydrazone **2.36** in 63% yield. Subsequent

condensation with aniline in refluxing ethanol led to the amidrazone **1.28** in 60% yield, which underwent oxidation in ethanol to form the imidrazone **1.29** in 34% yield. DBU-mediated oxidative cyclization and subsequent stirring at room temperature delivered radical **1.0** in 40% yield.

The radical 8-amino-1,3-diphenyl-1,2,4-benzotriazinyl-4-yl (**1.1**) was also synthesized as shown in Scheme 2.9. Benzaldehyde and phenylhydrazine were condensed to give hydrazone **2.35** in 68% yield, which was chlorinated using the Corey-Kim reagent at $-78\text{ }^{\circ}\text{C}$ to furnish chlorohydrazone **2.36** in 63% yield. Condensation with *m*-phenylenediamine in refluxing ethanol led to the amidrazone **1.28**. Treatment of this intermediate with DBU in ethanol resulted in the formation of three distinct products. A minor fraction was identified as an unexpected 8-functionalized leuco radical **1.12** and confirmed by single-crystal X-ray diffraction (SC-XRD, see **Figure 1.27**). This leuco radical gradually oxidized in solution (toluene and acetonitrile) to form the 8-Amino-1,3-diphenyl-1,2,4-benzotriazinyl-4-yl **1.1** over time (see Spectroscopy Section). A second major fraction corresponded to a zwitterionic compound **2.11**, and was assigned as tetraphenylhexaazaanthracene (TPHA), consistent with literature reports¹⁰¹ and confirmed by HRMS, NMR spectroscopy and SC-XRD.



The radical 6-chloro-1,3-diphenyl-1,2,4-benzotriazinyl-4-yl (**1.4**) was synthesized according to the method in Scheme 2.4. Hydrazone **2.35** was obtained from the condensation of benzaldehyde with phenylhydrazine in 68% yield. Chlorination with Corey-Kim reagent furnished chlorohydrazone **2.36** in 63% yield. Condensation with 3-chloroaniline in refluxing ethanol provided the amidrazone **1.28**. Oxidation to the corresponding imidrazone **1.29** occurred in 34% yield, followed by DBU-mediated oxidative cyclization to give radical **1.4** in 40% yield

The radical 6-methyl-1,3-diphenyl-1,2,4-benzotriazinyl-4-yl (**1.3**) was synthesized via the route outlined in Scheme 2.4. Initial condensation of benzaldehyde with phenylhydrazine produced hydrazone **2.35** in 68% yield. This was converted to chlorohydrazone **2.36** using the Corey-Kim reagent (63% yield). Condensation with 3-methylaniline in refluxing ethanol afforded amidrazone **1.28**, which, upon oxidation, formed imidrazone **1.29** in 34% yield. Oxidative cyclization, under DBU/O₂ conditions, yielded radical **1.3** in 60% yield.

The radical 6-nitro-1,3-diphenyl-1,2,4-benzotriazinyl-4-yl (**1.5**) was prepared via the synthetic route outlined scheme 2.10 below. Benzaldehyde and phenylhydrazine were condensed in ethanol at room temperature to afford hydrazone **2.35** in 68% yield. Subsequent chlorination using the Corey-Kim reagent at -78 °C provided chlorohydrazone **2.36** in 63% yield. Condensation with 3-nitroaniline in refluxing ethanol yielded the

corresponding amidrazone **1.8** in 50-60% yield . Oxidation in ethanol led to the imidrazone **1.29** in 34% yield, which upon DBU-catalyzed oxidative cyclization and stirring at room temperature gave radical **1.5** in 33% yield.

2.4 Molecular structure

The crystal structure of benzotriazinyl radicals provides further insight into their molecular framework. The benzotriazinyl moiety remains largely planar, while the N1-phenyl ring displays a significant torsional angle of about 40-50° due to steric interactions between ortho-hydrogens.¹⁰² These structural features, observed in crystallographic analyses of derivatives like DPBT , contribute to the radicals' stability, intermolecular interactions and pathways for magnetic exchange.

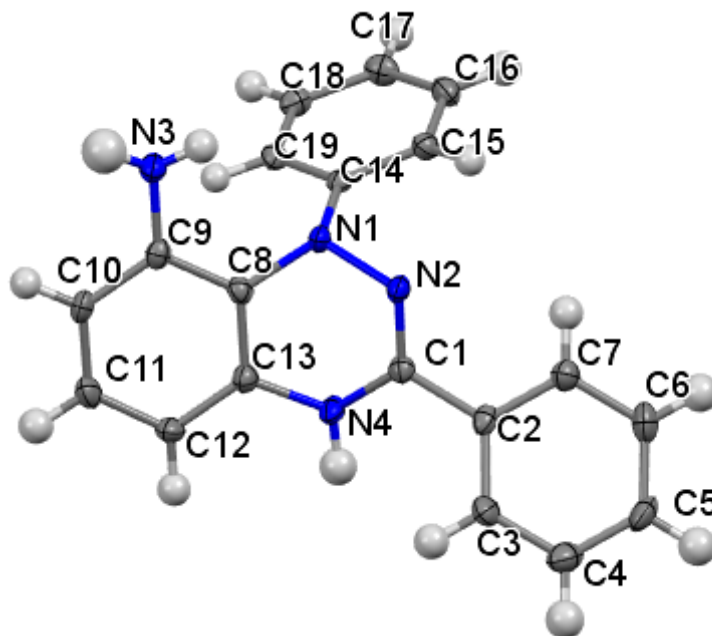


Figure 1. 6 The Crystal Structure of leuco Radical **1.12** (50% Probability Ellipsoids and Hydrogen Atoms shown)

Single blue block-shaped crystals of **1.12** were recrystallized from a mixture of hexane and ethyl acetate by slow evaporation. A suitable crystal with dimensions $0.30 \times 0.27 \times 0.08 \text{ mm}^3$ was selected and mounted on a mylar loop in oil on a Bruker APEX-II CCD diffractometer. The crystal was kept at a steady $T = 100(2) \text{ K}$ during data collection. The structure was solved with the ShelXT 2018/2¹⁰³ solution program using Intrinsic Phasing methods and by using Olex2 1.5¹⁰⁴ as the graphical interface. The model was refined with ShelXL 2019/3¹⁰⁵ using full matrix least squares minimization on F^2 .

Table 2. 1 Summary of the X-ray crystallographic data for **1.12**

Radical	1.12
Empirical Formula	C ₁₉ H ₁₆ N ₄
F _w	300.36
crystal system	orthorhombic
Space group	<i>P2₁2₁2₁</i>
Temp	100(2)
a (Å)	7.9869(5)
b (Å)	11.0281(6)
c (Å)	17.1648(11)
β, deg	90
V, (Å ³)	1511.88(16)
Z	4
Crystal size/mm ³	0.3 × 0.27 × 0.08
Goodness of Fit	1.049
Residual: R1, wR2 ^a	0.0528 ,0.1303

The compound crystallized in the orthorhombic system, space group *P2₁2₁2₁*, with *Z* = 4 molecules per unit cell. The molecular framework retains the core structure found in the parent BTR radical, but with notable changes in bond length and geometry consistent with the leuco form. The central N1–N2–C1–N4 fragment (analogous to N1–N2–C3–N4 in parent BTR) shows a torsion of $-9.7(4)^\circ$, compared to $0.5(2)^\circ$ in the parent compound,

indicating a deviation from planarity. However, the most significant difference is observed in the N1–N2 bond length, which is 1.463(3) Å in the leuco radical—considerably longer than the 1.361(2) Å in parent BTR—reflecting a reduction in double-bond character and loss of delocalization in the amidrazonyl core. The aryl rings flanking the central structure are also more twisted in the leuco form. The N2–N1–C8–C9 torsion is 142.3(3)°, contrasting sharply with the parent compound's N2–N1–C8a–C4a = 4.3(2)°, and the N2–N1–C14–C15 torsion is –29.1(4)°, indicating that both phenyl rings are significantly out of plane. This contrasts significantly with the more planar arrangement observed in the parent radical and suggests that the N-1 nitrogen is pyramidalized.

Table 2. 2 Selected bond lengths (Å) and angles (°) for 1.12.

Bond (Parent BTR)	Length (Å)	Bond (Leuco Radical)	Length (Å)
N1–N2	1.361(2)	N1–N2	1.463(3)
N2–C3	1.337(2)	N2–C1	1.294(4)
C3–N4	1.324(2)	C1–N4	1.378(4)

Bond (Parent BTR)	Length (Å)	Bond (Leuco Radical)	Length (Å)
C3–C1''	1.489(3)	C1–C2	1.480(4)
N1–C8a	1.401(2)	N1–C8	1.427(4)
N1–C1'	1.427(2)	N1–C14	1.420(4)

Table 2.3 Selected Torsional angles (°) for 1.12 and 1.0

Torsion Segment	Parent BTR (°)	Amino Leuco Radical (°)
N1–N2–C3–N4 / N1–N2–C1–N4	0.5(2)	–9.7(4)
N2–N1–C8a–C4a / N2–N1–C8–C9	4.3(2)	142.3(3)
— / N2–N1–C14–C15	—	–29.1(4)
— / C13–N4–C1–C2	—	158.3(3)
— / N1–C14–C15–C16	—	178.3(3)

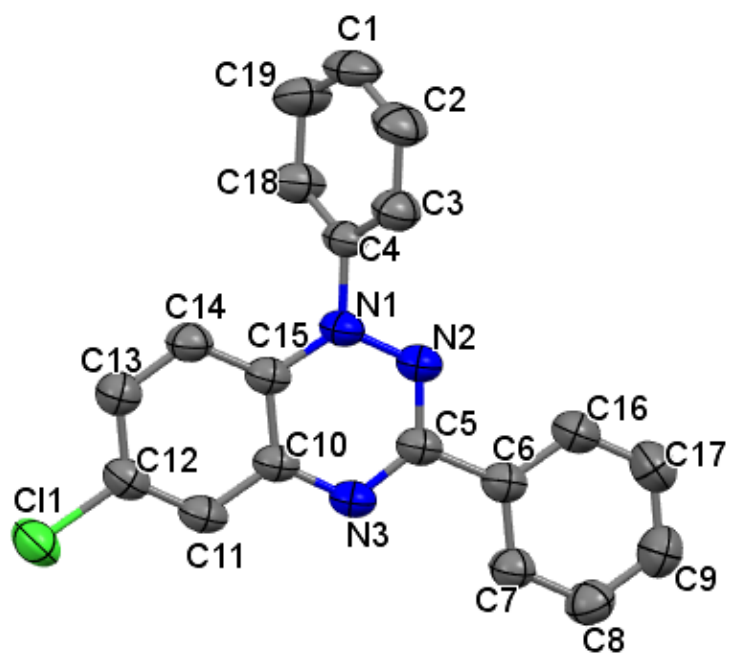


Figure 1. 7 Crystal Structure of Radical **1.4** (50% Probability Ellipsoids and Hydrogen Atoms omitted for Clarity)

Table 2. 4 Summary of the X-ray crystallographic data for **1.4**

Radical	1.4
Empirical Formula	C ₁₉ H ₁₃ N ₃ Cl
F _w	318.77
crystal system	triclinic
Space group	<i>P</i> -1
Temp	299(2)
a (Å)	7.8131(12)
b (Å)	9.8080(15)
c (Å)	11.5048(17)
β, deg	86.4
V, (Å ³)	775.9(2)
Z	2
Crystal size/mm ³	0.3 × 0.3 × 0.2
Goodness of Fit	1.067
Residual: R1, wR2 ^a	0.0399,0.1135

Radical 1.4, crystallized via slow evaporation from a 70:30 hexane: ethyl acetate mixture, forming black crystals (0.3 × 0.3 × 0.2 mm³) in the triclinic *P*-1 space group with *Z* = 2.

Its molecular structure closely mirrors the parent BTR radical, with a near-planar amidrazonyl core (N1–N2–C5–N3 torsion of –0.1(2)° vs. 0.5(2)° in BTR) and bond

lengths (e.g., N1–N2 = 1.3612(16) Å, N2–C5 = 1.3349(17) Å) nearly identical to BTR, indicating an unchanged electronic structure. However, the 6-chloroBTR derivative shows a significant twist in one phenyl ring (N2–N1–C4–C3 = $-55.07(17)^\circ$ vs. $50.3(2)^\circ$ in BTR) and enhanced planarity on the opposite side (N2–N1–C15–C14 = $175.13(12)^\circ$ vs. $4.3(2)^\circ$ in BTR), suggesting reduced steric strain or increased π -delocalization.

The chlorine-bearing phenyl ring remains coplanar (C11–C12–C13–C14 = $179.42(11)^\circ$), with conformational distortion localized to the twisted side, yielding an asymmetric yet stable geometry. Bond angles, such as N2–N1–C4 = $113.91(11)^\circ$ (vs. $122.2(1)^\circ$ in BTR), indicate subtle geometric adjustments due to chlorine substitution, but core planarity and delocalization are preserved, as evidenced by consistent bond angles (e.g., N2–C5–N3 = $127.68(13)^\circ$ vs. $127.7(2)^\circ$ in BTR) and C–C bond lengths (1.366–1.393 Å) across aromatic systems.

Table 2.5 Selected bond lengths (Å) and angles (°) for **1.4**.

Bond (Parent BTR)	Length (Å)	Bond (1.4)	Length (Å)
N1–N2	1.361(2)	N1–N2	1.3612(16)
N2–C3	1.337(2)	N2–C5	1.3349(17)
C3–N4	1.324(2)	C5–N3	1.3373(18)
C3–C1''	1.489(3)	C5–C6	1.484(2)
C6–C7	1.389(3)	C6–C7	1.3872(19)
C7–C8	1.375(2)	C7–C8	1.382(2)

Table 2.6 Key Torsional angles (°) for **1.4** and **1.0**

Torsion (Parent BTR)	Angle (°)	Torsion (1.4)	Angle (°)
N1–N2–C3–N4	0.5(2)	N1–N2–C5–N3	–0.1(2)
C8a–N1–C1'–C6'	50.3(2)	N2–N1–C4–C3	–55.07(17)
N2–N1–C8a–C4a	4.3(2)	N2–N1–C15–C14	175.13(12)
C11–C12–C13–C14 (no analog in parent) –		C11–C12–C13–C14	179.42(11)

Table 2. 7 Selected Bond Angles (°)

Angle (Atoms) Parent BTR (°) Leuco BTR (°)

N2–N1–C8a	122.2(1)	N2–N1–C8 = 114.5(2)
N2–N1–C1'	114.3(1)	N2–N1–C14 = 111.0(2)
C1–N2–N1	—	114.1(2)
C1–N4–C13	—	118.6(3)

2.5 Spectroscopic characterization

The six radical derivatives were characterized by electronic absorption spectroscopy, and EPR spectroscopy to determine how substitution at the 6-position modified their electronic structures in both the ground state and excited state.

2.5.1 Electronic absorption spectroscopy

The electronic absorption spectra of the substituted radicals—**1.2** (OMe, electron-donating group), **1.3** (-Me, electron-donating group), **1.4** (-Cl, weak electron-withdrawing group), and **1.5** (-NO₂, strong electron-withdrawing group)—were compared to the unsubstituted parent radical **1.0** to study how different substituents affect electronic

transitions. The spectrum of the parent radical **1.0** features $\pi \rightarrow \pi^*$ transitions in the UV region (with peaks at 286 nm and 374 nm) and weaker transitions in the visible region due to HOMO-SOMO and SOMO-LUMO transitions (peaks at 447 nm and 564 nm). These transitions give **1.0** a dark brown/black color in the solid state and an orange/brown color in solution. The NO₂-substituted radical **1.5** stands out with a unique spectrum, suggesting a major change in its electronic structure, including several weak transitions in the visible region (peaks at 433 nm, 458 nm, and 665 nm) and one in the near-infrared (NIR) region (742 nm)

The electronic absorption spectra of the 8-amino functionalized radical (**1.1**) exhibit distinct features compared to the parent radical (**1.0**), indicating a significant alteration in the electronic structure. The spectra reveal prominent $\pi\text{-}\pi^*$ transitions in the UV region, with absorption maxima at $\lambda_{\text{max}} = 289$ nm, 309 nm, and a broader range from 360 nm to 483 nm. Additionally, the increasing intensity of the low-energy transition in the visible region (600-800 nm) is attributable to HOMO-SOMO and SOMO-LUMO transitions, reflecting the progressive formation and stabilization of the radical species.

The time-dependent spectral data suggest that an initial isolation of a leuco radical (**1.12**) form of the 8-amino radical occurred, with a gradual transformation into the radical form becoming evident after approximately 15 hours. This conversion is marked by a progressive increase in radical concentration over time, observable in both toluene and acetonitrile solvents, and further corroborated by the growing absorption in the 600-800 nm range. The absence of an isosbestic point during this transformation indicates a clear

and direct conversion from the leuco radical to the radical, rather than a reversible equilibrium or the presence of multiple intermediates.

Furthermore, the observed increase in absorbance, corresponding to an enhanced extinction coefficient, supports the hypothesis of a complete structural transformation to the 8-amino functionalized radical (**1.12**). This suggests that the molecular changes extend beyond mere electronic redistribution, potentially involving a distinct chemical species with heightened chromophoric activity, as evidenced by the intensified radical-specific absorption in the visible region.

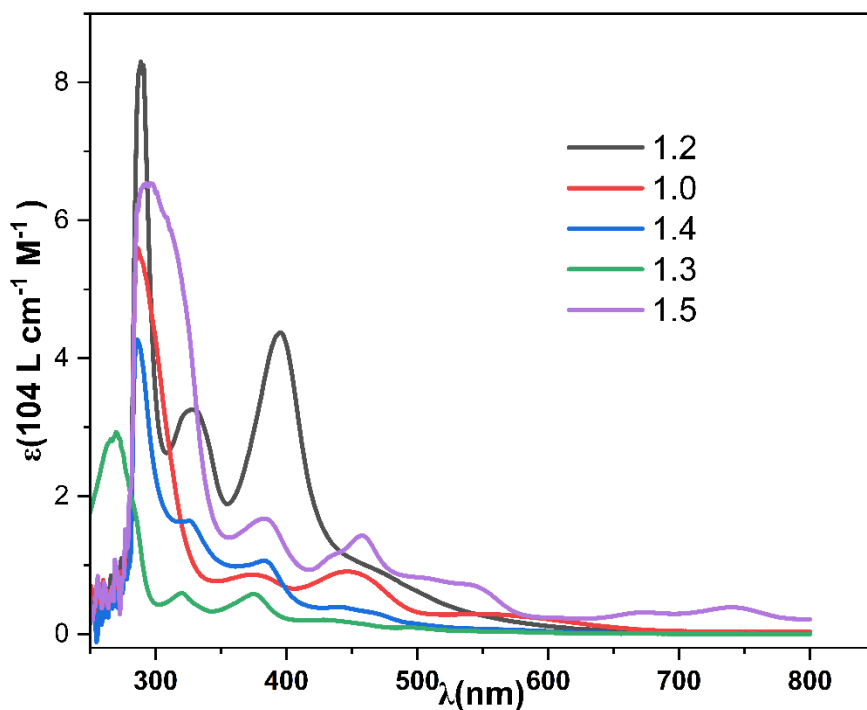


Figure 1. 8 Electronic absorption spectra of 1.0,1.2-1.5 in toluene at 300k

Table 2. 8 Absorption data for radicals 1.1,1.3,1.5,1.6, and 1.0.

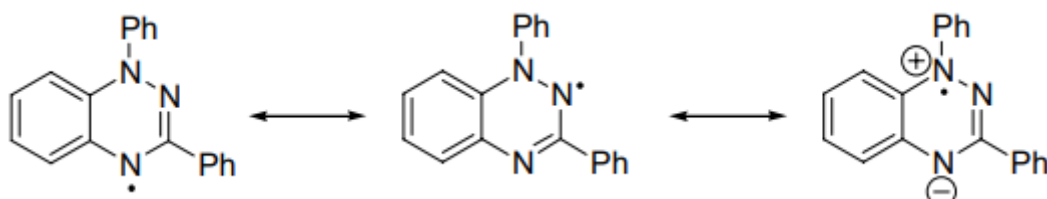
	$\lambda_{\max} (\epsilon) \text{ a}$						
1.4	286(4.2)	327(1.6)	338(1.07)	441(0.3)	469(0.2)		
1.3	270(2.9)	320(0.6)	371(0.5)	431(0.2)	496(0.1)		
1.5	294(6.5)	384(1.69)	433(1.1)	458(1.42)	665(0.3)	742(0.4)	
1.2	289(8.3)	328(3.2)	395(4.3)	477(0.9)			
1.0	286(5.5)	374(0.8)	447(0.92)	564(0.2)			

2.5.2 Electron Paramagnetic Resonance (EPR) Analysis for Radicals 1.1-1.5

This section examines the electron paramagnetic resonance (EPR) spectra of radicals 1.2, 1.5, and 1.0, focusing on their hyperfine coupling constants which relates to spin density distributions. EPR spectroscopy was conducted using a Bruker EMXplus electron paramagnetic resonance spectrometer (EPR) with cryogenic capabilities operating at approximately 9.5 GHz. A 1mM solution of the samples was prepared in toluene and measured at room temperature. The hyperfine coupling constants for the nitrogen and hydrogen nuclei were determined by simulating the EPR spectra with Easy Spin 6.0.7. The

simulation included couplings only to hydrogens in the methyl, and methoxy derivatives, as their spectra revealed splitting and broadening due to interactions with nearby hydrogen nuclei, but excluded couplings to phenyl ring hydrogens.

EPR spectroscopy was employed to investigate how functionalization affects the distribution of the unpaired electron across the radical structures. Previous report by Neugebauer and Rimmler demonstrated that the unpaired electron is delocalized within the amidrazonyl segment of the 1,2,4-triazinyl cycle. using electron nuclear double resonance (ENDOR), they reported hyperfine coupling constants for the three chemically distinct nitrogen atoms in the triazine core as : N-1 (~ 7.5 G), N-2 (~ 4.9 G), and N-4 (~ 5.2 G)⁹⁵ . These values indicate that the unpaired electron is predominantly located on the N-1 nitrogen, consistent with the resonance structures of benzotriazinyl radicals below, and highlighting the significant role of resonance in dictating hyperfine coupling values.



The experimental spin density was calculated using the McConnell equation, $a = Q\rho$, where a is the hyperfine coupling constant, Q is a semiempirical constant (28.6 G for nitrogen, -27 G for hydrogen), and ρ is the spin density. The EPR spectrum of radical 1.0 shows a seven-line pattern ($2n+1$, where $n=3$ for three equivalent nitrogen nuclei with spin

quantum number $I=1$), reflecting hyperfine interactions between the unpaired electron and the three nitrogen atoms in the triazine core. Minor super-hyperfine coupling (<1 G) to benzene ring hydrogens causes slight resonance broadening.

Table 2. 9 Hyperfine coupling constants (a_N) and g-values the series of radicals.

Radical	g-value	$a_{(N1)}$ *	$a_{(N2)}$ *	$a_{(N4)}$ *
1.0 (Parent BTR)	2.0033	7.5	4.9	5.2
1.1 (NH ₂)	2.0023	7.70	4.90	4.98
1.2 (OMe)	2.0038	7.89	4.10	4.92
1.3 (Me)	2.0035	7.73	4.38	4.90
1.4 (Cl)	2.0036	7.34	4.70	4.81
1.5 (NO ₂)	2.0038	6.64	4.92	5.11

*The g-values and hyperfine were derived from fitting of the experimental EPR spectra with Easy Spin. Tentative assignment of isotropic nitrogen hyperfine values is made by comparison to ENDOR data for the parent diradical, in which the larger spin density is observed for N1.

EPR spectroscopy reveals subtle differences in electronic structure between substituted members of the series of radicals 6-X-BTR. The g-values are close to that of the free electron value ($g_e = 2.0023$), consistent with isotropic $S=1/2$ spin systems, in which little

to no g-anisotropy is expected due to a lack of spin-orbit coupling or low-lying excited states. Hyperfine is apparent to the three nitrogens of the triazinyl core, in which the nuclear spin of N ($I=1$) leads to a splitting of the resonance into a multiplicity of seven lines ($2nI + 1$, in which n is the number of nuclei). Analysis of the hyperfine coupling to nitrogens reveals an increase in spin density at N1, relative to the parent for electron donating groups (amine, methoxy), and a decrease in spin density at N1 relative to the parent for electron withdrawing groups. Electron withdrawing groups stabilize organic radicals through resonance or inductive effects, leading to a decrease in overall spin density in the triazinyl core, as evidenced by a slight to moderate decrease in spin density at N2 and N4 in these systems ($X = \text{NO}_2, \text{Cl}$). For example, while the parent radical exhibits hyperfine values of 7.5, 4.9, and 5.2 for N1, N2 and N4, respectively, these values change for the nitro derivative (1.5) to 6.64, 4.92 and 5.11, respectively. For electron donating groups by resonance, we observe an increase in electron density at N1, with a slight to moderate decrease in spin density at N2 and N4, consistent with electron donation primarily to N1, as the substituent is in the para position to N1, where resonance effects would be strong. These subtle shifts in electron density suggest changes in reduction and oxidation potentials along the series, in line with substituent effects.

Lastly, EPR spectra were measured at 298 K in toluene as a function of time of the leuco radical, to provide support for the hypothesis that the leuco radical undergoes oxidation to the amino radical slowly over time with oxygen exposure. As can be seen from Figure 1.7, the EPR resonance due to the amino radical grows over 24 hours, consistent with an increase of radical concentration as a function of oxidation time. This dynamic evolution

results from absorption spectroscopy, which suggests a transformation from an isolated leuco (reduced) form to the radical species.

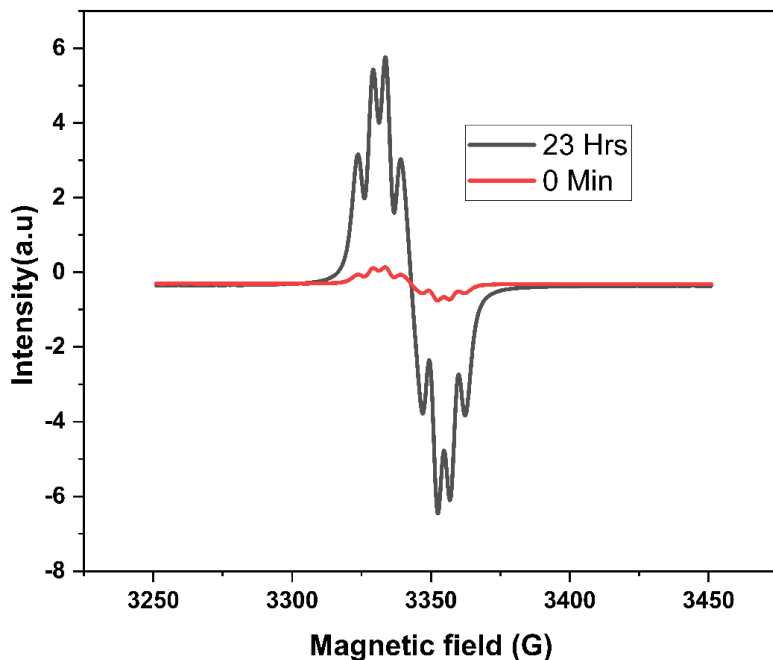


Figure 1. 9 CW X-Band EPR spectrum of 1.12 in toluene at 298k

2.6 Electrochemistry

The electrochemical behavior of benzotriazinyl radicals is a critical aspect of their utility in redox flow battery and charge storage applications. These radicals exhibit reversible one-electron oxidation and reduction processes, which are essential for their use in electrochemical devices such as batteries and sensors.^{106–108} Benzotriazinyl radicals are also chemically and electrochemically stable allowing for the repeated cycling of the radical between its oxidized and reduced forms over numerous cycles, which is crucial for

applications in charge storage materials where longevity and efficiency are paramount.⁵¹ For example, in organic radical batteries (ORBs), the stability of the redox couple directly impacts the cycling performance and overall efficiency of the device.¹⁰⁹

Another key feature of Blatter radicals is their electrochemical tunability. By introducing substituents at various positions on the benzotriazinyl ring, the oxidation and reduction potentials can be shifted to more positive or negative values without compromising the reversibility of the redox processes. This tunability is particularly valuable for optimizing their performance in specific applications. A larger E_{cell} enhances the energy density and power output of the device. Research by the Frank group on halogen-functionalized derivatives of Blatter radicals demonstrated that substitutions with electron-withdrawing groups shift both oxidation and reduction potentials to more positive values compared to the parent radical (**figure 1.21**). Specifically, halogen-functionalized Blatter radicals exhibited oxidation potentials up to 600 mV more positive than the parent radical, while maintaining fully reversible redox behavior. This property allows for the design of Blatter-based materials with tailored electrochemical properties for specific applications.

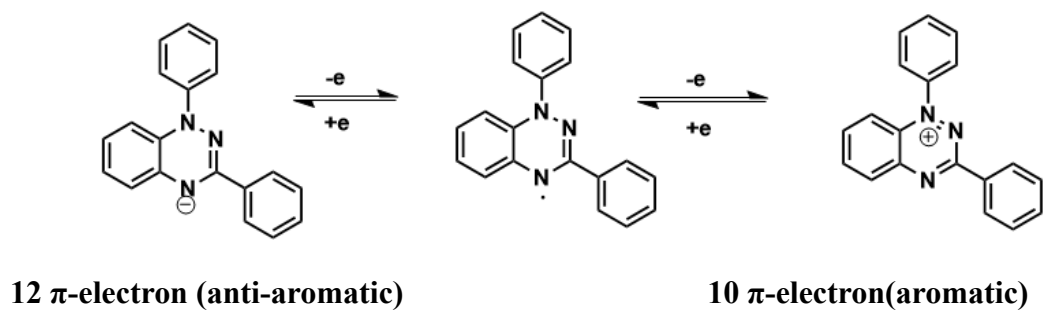


Figure 1.10 Electrochemical oxidation and reduction process of benzotriazinyl radicals

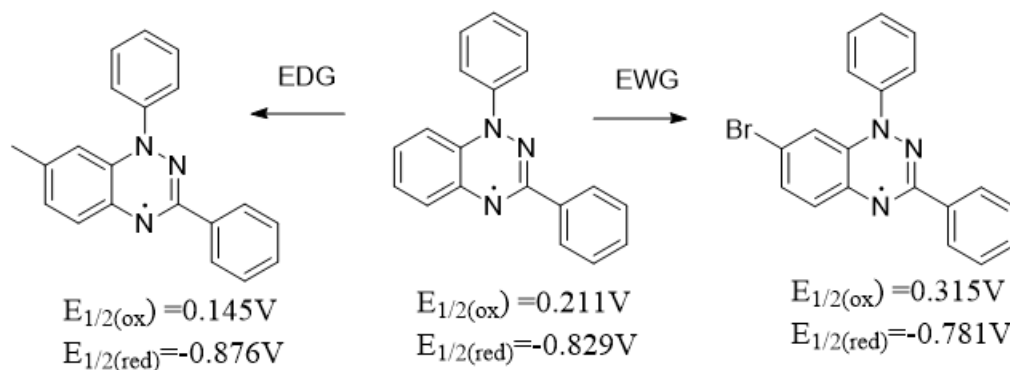


Figure 1.11 Effect of EWG and EDG substitution on electrochemistry (V vs SCE)

As the parent radical is an 11- π electron system, the ease and reversibility of the oxidation process has been rationalized by arguments based on aromaticity. Oxidation results in the formation of a 10 π -electron aromatic system during oxidation and a 12 π -electron antiaromatic anion during reduction⁴⁶ (**figure 1.8**). The aromatic stability of the oxidized form and the antiaromaticity of the reduced form underpin the radicals' reversible

electrochemistry and low oxidation potentials, marking them as efficient electron donors, and highlighting their promise for charge storage applications.^{51,110}

Cyclic voltammetry (CV) measurements were carried out using a BASI electrochemical workstation in a standard three-electrode cell configuration. A glassy carbon disk electrode (3 mm diameter) served as the working electrode, platinum wire as the counter electrode, and a silver/silver chloride (Ag/AgCl in 3 M KCl) electrode was used as reference. The working electrode was polished using 0.05 μm alumina slurry, rinsed with deionized water, and dried prior to use. All potential is reported versus Ag/AgCl unless otherwise noted. Electrochemical measurements were conducted in dry acetonitrile containing 0.1 M tetrabutylammonium hexafluorophosphate (TBAH) as the supporting electrolyte. Solutions were deoxygenated by bubbling with nitrogen for 20 minutes prior to measurement and maintained under a gentle nitrogen flow throughout data collection. Voltammograms were recorded at a scan rate of 10-500 mV s^{-1} over a potential window of -1.5 V to $+1.0$ V. In selected cases, additional CV scans were performed at varied scan rates (10–500 mV s^{-1}) to probe diffusion control via Randles–Sevcik analysis. $E_{1/2}$ values were determined as the average of cathodic and anodic peak potentials.

Table 2. 10 Select electrochemical parameters for 1.2, 1.3, 1.4, 1.5 and 1.0

Radial derivative	$E_{1/2}(\text{ox})/\text{V}^{\text{a}}$	$E_{1/2}(\text{red})/\text{V}^{\text{b}}$	$E_{\text{cell}}/\text{V}^{\text{c}}$	$i_{\text{a}}/i_{\text{c}}$ (100mV/s)		ΔE_{p} (100mV/s)	
				Ox	Red	Ox	Red
-Cl	0.32	-0.6	0.92	0.9	1.07	72	72
-NO ₂	0.538	-0.489	1.02	0.83	1.05	79	73
-OMe	0.095	-0.827	0.92	0.98	1.1	68	90
-Me	0.185	-0.827	1.01	1.1	2.0	69	89
-NH ₂	0.24	-0.613	0.85	0.99	1.98	86	87
-H (Parent BTR)	0.212	-0.878	1.09	0.9	4.5	226	257

^a $E_{1/2}$ calculated as the average of the peak potential of the anodic and cathodic waves of the electrochemical process. ^c $E_{\text{cell}} = |E_{1/2}(\text{ox}) - E_{1/2}(\text{red})|$. $i_{\text{a}}/i_{\text{c}}$ is the ratio of anodic and cathodic current. ΔE_{p} is the difference in anodic and cathodic peak potential, reported in mV

Substitution on the sixth position of the benzoannulated ring significantly influences the redox behavior of the radical core. Electron-withdrawing substituents, such as $-\text{Cl}$ and $-\text{NO}_2$, shift the oxidation potential anodically, making the radical more resistant to oxidation. For instance, the nitro-substituted derivative exhibits an oxidation potential of $+0.538\text{ V}$, over 300 mV more positive than the parent compound. Conversely, electron-donating groups such as $-\text{OMe}$ and $-\text{Me}$ lower the oxidation potential to $+0.095\text{ V}$ and $+0.185\text{ V}$, respectively, indicating increased ease of oxidation relative to the parent radical. A similar trend is observed in the reduction behavior. The strongly electron-withdrawing $-\text{NO}_2$ group stabilizes the radical anion form, resulting in a substantially anodically shifted reduction potential of -0.489 V . The $-\text{Cl}$ derivative also reduces more easily than the parent (-0.600 V), while the methoxy and methyl derivatives remain slightly easier to reduce than the parent radical, both exhibiting reduction potentials of -0.827 V . The overall electrochemical window, defined as the difference between oxidation and reduction half-wave potentials (E_{cell}), varies subtly among the derivatives. Substitution with $-\text{NO}_2$ results in a modestly narrower window of 1.02 V , while the $-\text{Cl}$ and $-\text{OMe}$ derivatives both show reduced cell potential of 0.92 V . The $-\text{Me}$ derivative maintains a cell potential of 1.01 V , closely resembling the parent radical in overall redox accessibility.

Cyclic voltammetry experiments underscore the tunability of redox properties in benzotriazinyl radicals through strategic para-substitution. Electron-deficient substituents shift both redox events anodically, stabilizing both oxidized and reduced forms, while electron-rich substituents favor oxidation at lower potentials. The relatively preserved redox spans suggest that the Blatter scaffold remains robust under electronic modulation

and may serve as a versatile core for molecular electronic or energy storage applications. These results demonstrate that substitution has a pronounced effect on both oxidation and reduction potentials, consistent with expected substituent effects on redox processes, and suggest tunability of redox behavior via strategic substitution, which may be of interest for the design of electroactive materials and redox-active molecular frameworks.

2.7 Heterogeneous rate constant and diffusion coefficient for 1.2, 1.3, 1.4, and 1.5

To calculate the diffusion coefficient, which gives one an idea of the rate of diffusion of the analyte, the Randles Sevcik equation for a quasi-reversible system¹¹¹ (equation S2) was utilized in which I_p = peak current (in A), n = number of electrons transferred, A = working electrode area (0.13cm^2), D = diffusion coefficient (in cm^2/s), C = concentration ($1 \times 10^{-6} \text{ mol}/\text{cm}^3$), v = scan rate (in V/s). A plot of peak current and square root of scan rate gives a slope that is inserted in equation 2 to solve for the diffusion coefficient.

$$I_p = (2.69 \times 10^5) \cdot n^{3/2} \cdot A \cdot D^{1/2} \cdot C \cdot v^{1/2} \quad \text{(equation 2)}$$

$$D = \left(\frac{\text{Slope}}{2.69 \times 10^5 \cdot n^{3/2} \cdot A \cdot C} \right)^2 \quad \text{(equation 3)}$$

Additionally, Nicholson's method is favored for determining standard rate constants in quasi reversible systems due to its straightforward approach. It demonstrates that the peak potential difference (ΔE_p) depends on a dimensionless kinetic parameter (ψ) and remains largely unaffected by the charge-transfer coefficient (α) within the range of 0.3 to 0.7¹¹. To apply this method, we measured ΔE_p across various scan rates and then calculated the associated ψ values using the equation below

A plot of inverse of square root of scan rate versus the associated Nicholson dimensionless values ψ , gave a slope that was inserted into equation 5 to calculate for the heterogenous rate constant (K^0)

$$\psi = \frac{(-0.6288 + 0.0021\Delta E_p)}{1 - 0.017\Delta E_p} \quad \text{(equation 4)}$$

$$\Psi = \frac{\gamma k^0}{\sqrt{\pi F \nu D / RT}} \quad \text{(equation 5)}$$

$$\gamma = \frac{D_{\text{red}}}{D_{\text{ox}}}$$

where $\gamma = D/D'$ the ratio of the diffusion constants for the reduction and re-oxidation ($x0/-$) or the ratio of the diffusion constants for the oxidation and re-reduction ($x0/+$)

$$k^0 = \frac{\text{slope} \cdot \sqrt{\pi F D / RT}}{\gamma} \quad \text{(equation 6)}$$

Table 2. 11 Diffusion coefficient and rate constant for 1.1, 1.3, 1.6, and 1.10

Derivative	D(x ^{0/-}) (× 10 ⁻⁶ cm ² /s)	D(x ^{0/+}) (× 10 ⁻⁶ cm ² /s)	k ⁰ (x ^{0/-}) (cm/s)	k ⁰ (x ^{0/+}) (cm/s)
-OMe	6.43	1.80	3.65×10 ⁻²	6.61×10 ⁻³
-Me	8.18	2.55	2.42×10 ⁻²	4.1×10 ⁻³
-Cl	6.73	9.09	1.04×10 ⁻²	3.07×10 ⁻²
-NO ₂	5.43	6.18	1.65×10 ⁻²	1.35×10 ⁻²

The electrochemical behavior of the substituted derivatives—1.2 (-OMe), 1.3 (-Me), 1.4 (-Cl), and 1.5 (-NO₂)—was analyzed to evaluate the influence of electron-donating and electron-withdrawing groups on diffusion coefficients and heterogeneous rate constants focusing on substituent-driven variations in electron transfer kinetics and mobility. Overall, electron-withdrawing groups (-Cl, -NO₂) tend to increase diffusion rates, possibly due to improved solvation and charge distribution, while electron-donating

groups (-OMe, -Me) influence electron transfer kinetics more significantly, with -OMe notably boosting reduction efficiency. These trends align with established substituent effects on redox processes and highlight the nuanced roles of resonance, inductive effects, and molecular size.

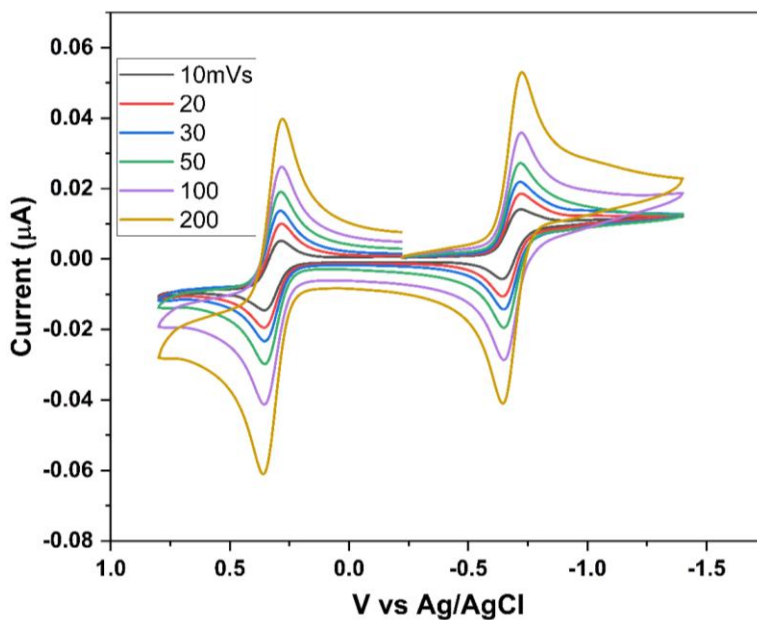


Figure 1. 12 Cyclic voltammograms of radical 1.4 in MeCN with 0.1 M [Bu₄N][PF₆] supporting electrolyte, glassy carbon working electrode, silver reference electrode, platinum counter electrode, 10-200 mV/s scan rate

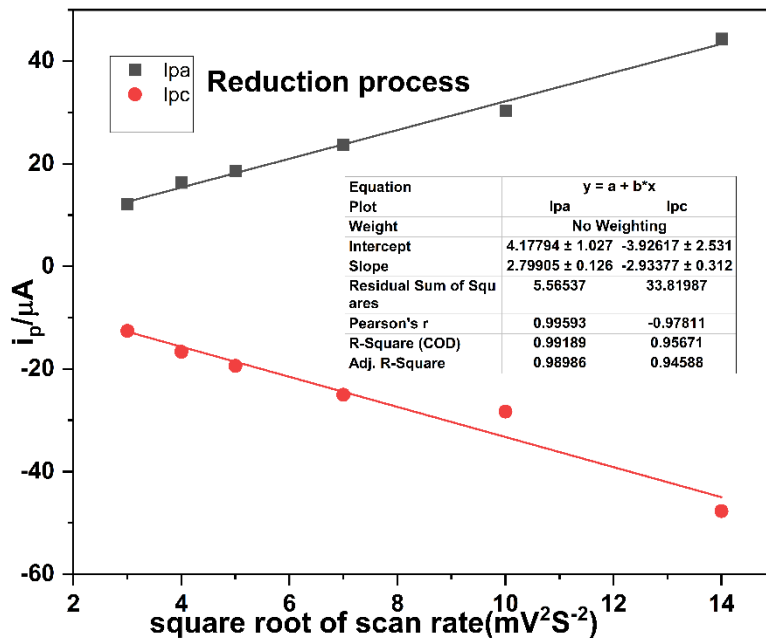


Figure 1. 13 Peak currents (i_{pc} and i_{pa}) from CV data vs. $v^{1/2}$ for the reduction process used to determine the diffusion coefficient from Randles Sevcik equation (see equation (S2) for radical 1.4. Lines are least-squares fits to the data

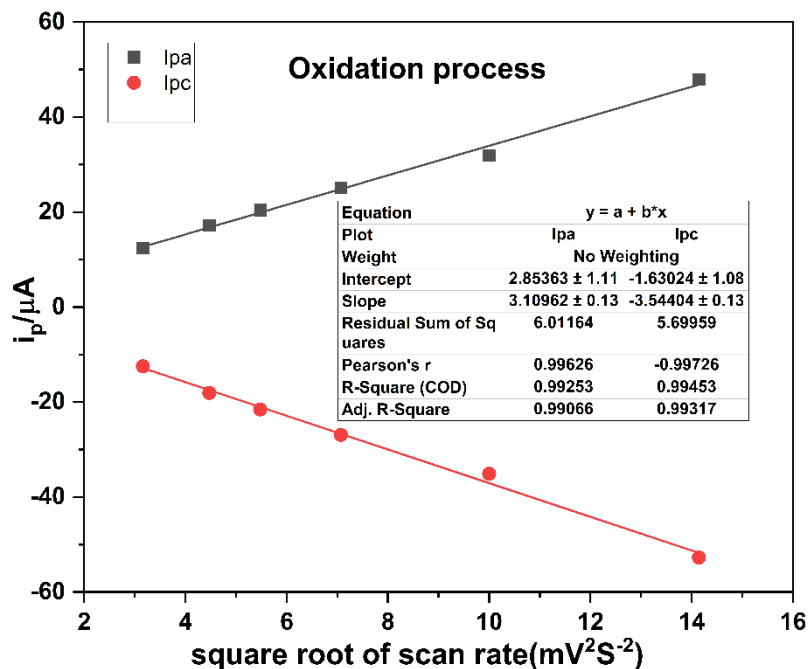


Figure 1. 14 Peak currents (i_{pc} and i_{pa}) from CV data vs. $v^{1/2}$ for the oxidation process used to determine the diffusion coefficient from Randles Sevcik equation (see equation (S2) for radical 1.4. Lines are least-squares fits to the data

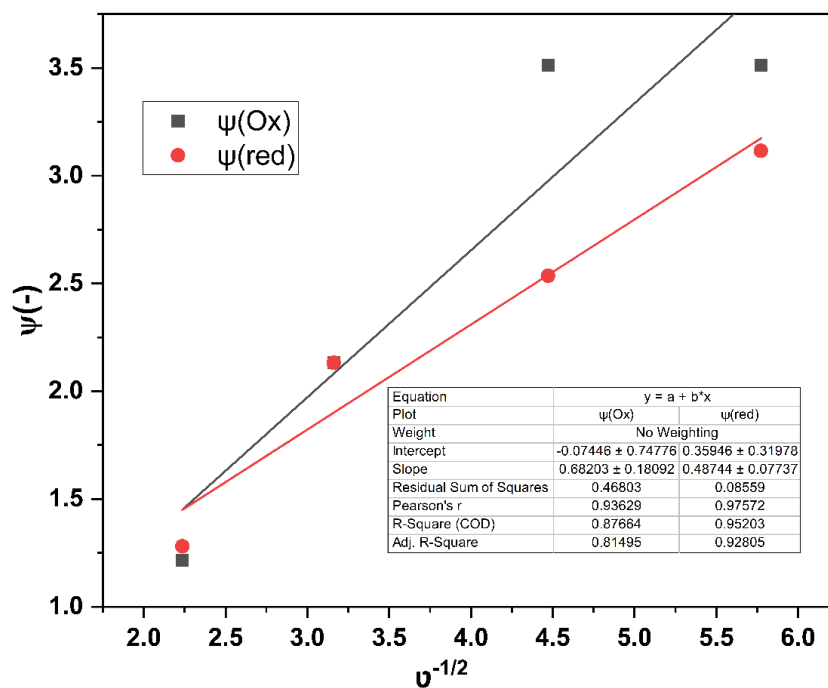


Figure 1. 15 Nicholson dimensionless coefficient Ψ (see Equation (S5 and S5) vs. $v^{-1/2}$ used to determine the electron transfer rate constants k^0 for 1.4

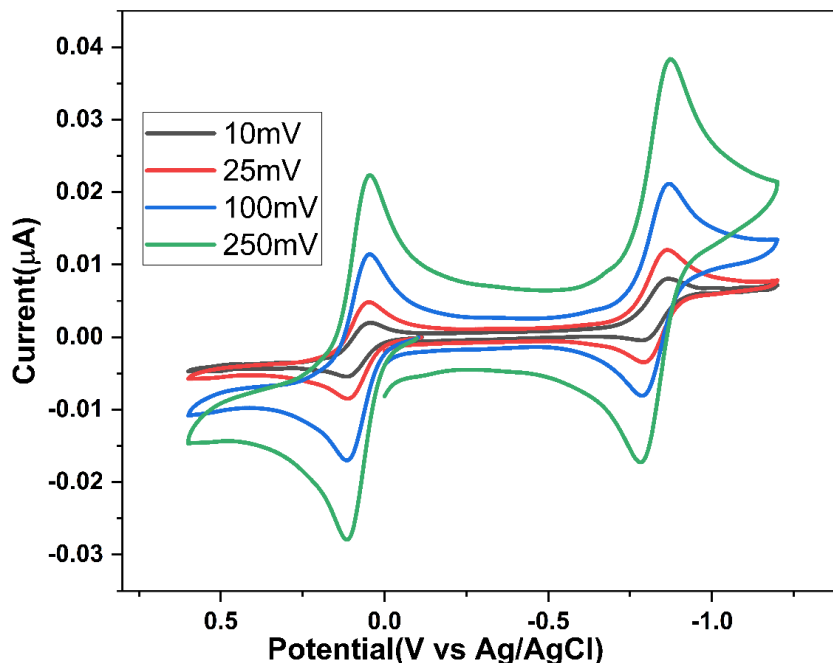


Figure 1. 16 Cyclic voltammograms of radical 1.2 in MeCN with 0.1 M [Bu₄N][PF₆] supporting electrolyte, glassy carbon working electrode, silver reference electrode, platinum counter electrode, 10-250 mV/s scan rate

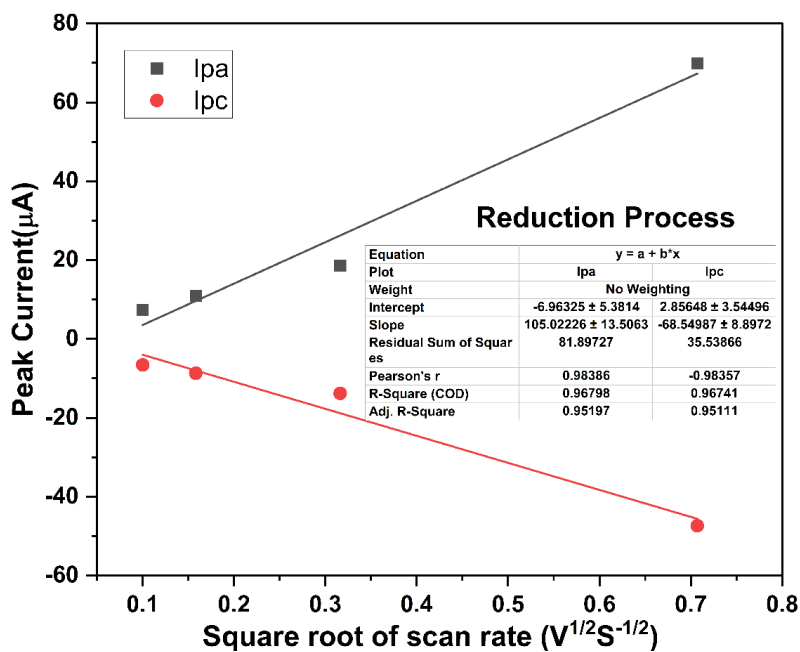


Figure 1. 17 Peak currents (i_{pc} and i_{pa}) from CV data vs. $v^{1/2}$ used to determine the diffusion coefficient from Randles Sevcik equation (see equation (S2)) for radical 1.2. Lines are least-squares fits to the data

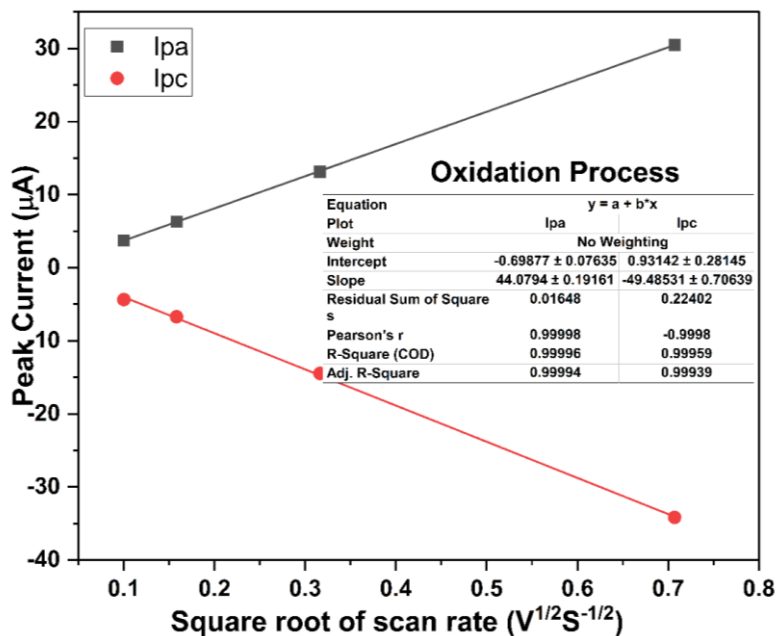


Figure 1. 18 Peak currents (i_{pc} and i_{pa}) from CV data vs. $v^{1/2}$ used to determine the diffusion coefficient from Randles Sevcik equation (see equation (S2) for radical 1.2). Lines are least-squares

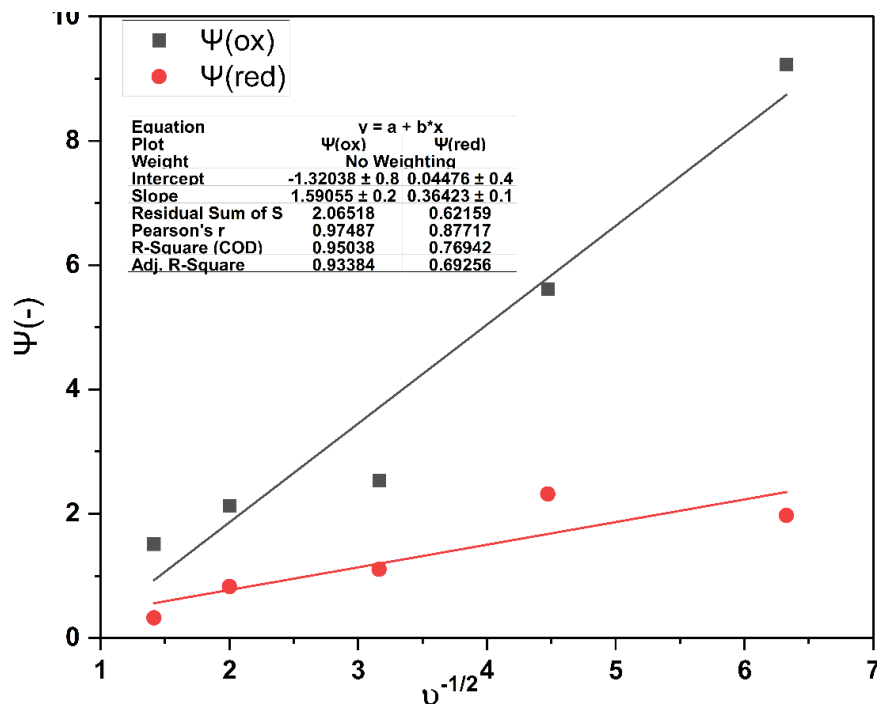


Figure 1. 19 Nicholson dimensionless coefficient Ψ (see Equation (S4 and S5) vs. $v^{-1/2}$ used to determine the electron transfer rate constants k^0

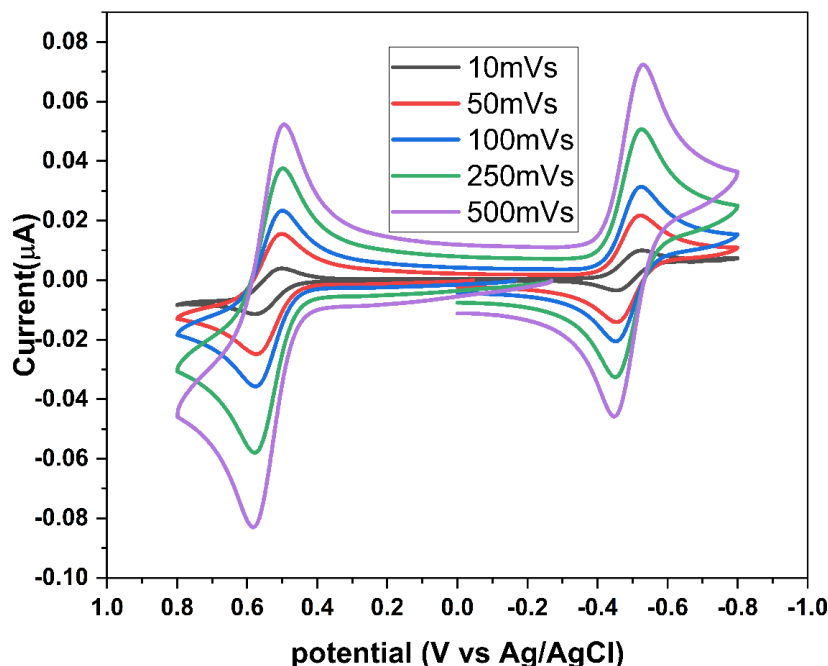


Figure 1. 20 Cyclic voltammograms of radical 1.5 in MeCN with 0.1 M [Bu₄N][PF₆] supporting electrolyte, glassy carbon working electrode, silver reference electrode, platinum counter electrode, 10-500 mV/s scan rate

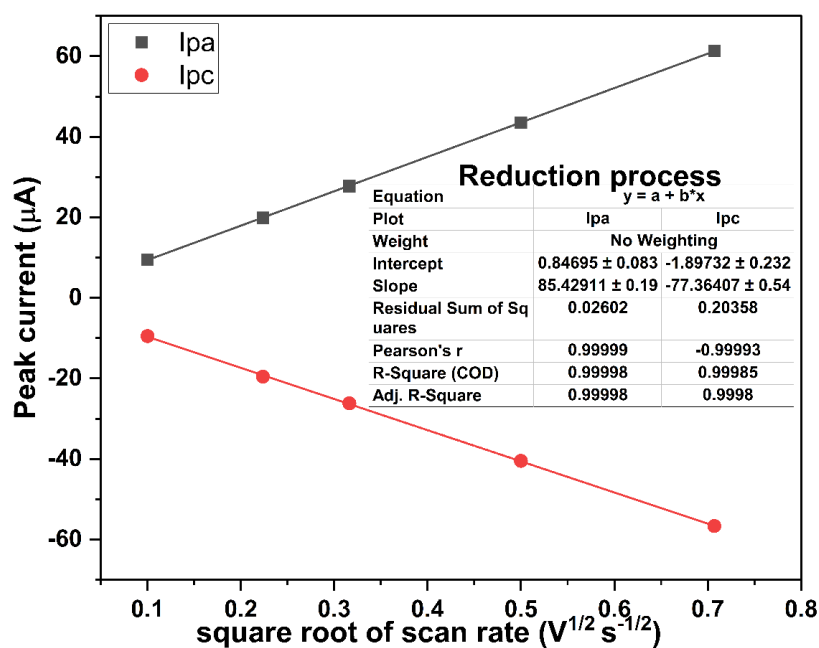


Figure 1. 21 Peak currents (i_{pc} and i_{pa}) from CV data vs. $v^{1/2}$ used to determine the diffusion coefficient from Randles Sevcik equation (see equation (S2) for radical 1.5. Lines are least-squares fits to the data

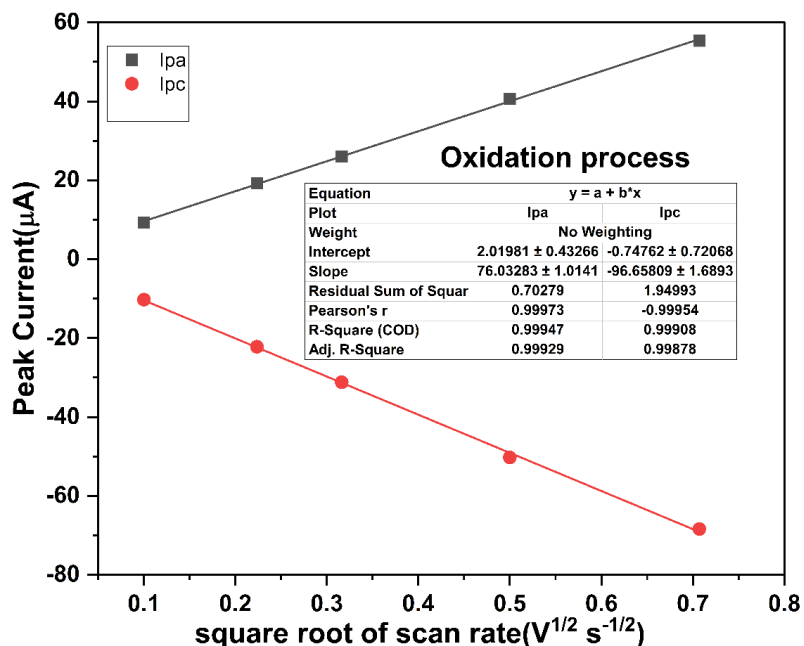


Figure 1.22 Peak currents (i_{pc} and i_{pa}) from CV data vs. $v^{1/2}$ used to determine the diffusion coefficient from Randles Sevcik equation (see equation (S2) for radical 1.5). Lines are least-squares fits to the data

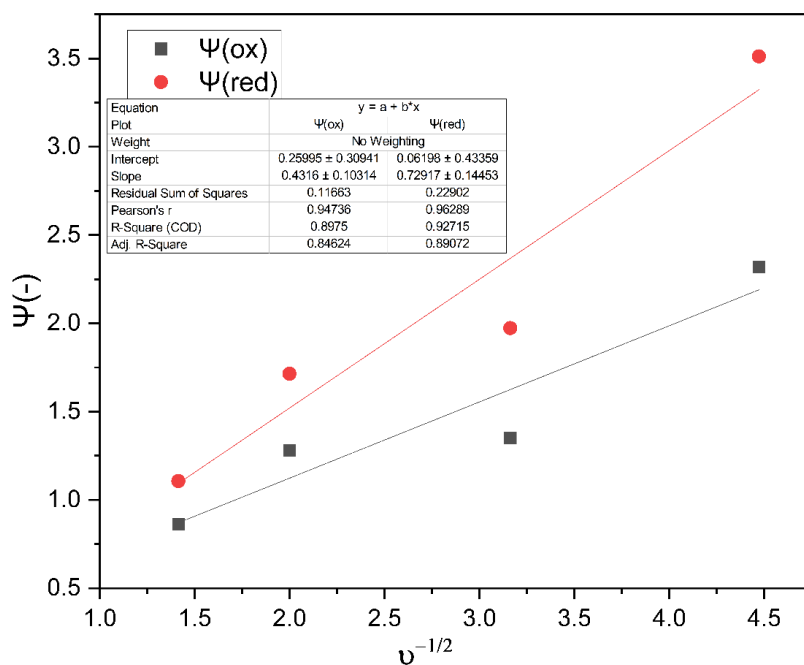


Figure 1.23 Nicholson dimensionless coefficient Ψ (see Equation (S4 and S5) vs. $v^{-1/2}$ used to determine the electron transfer rate constants k^0

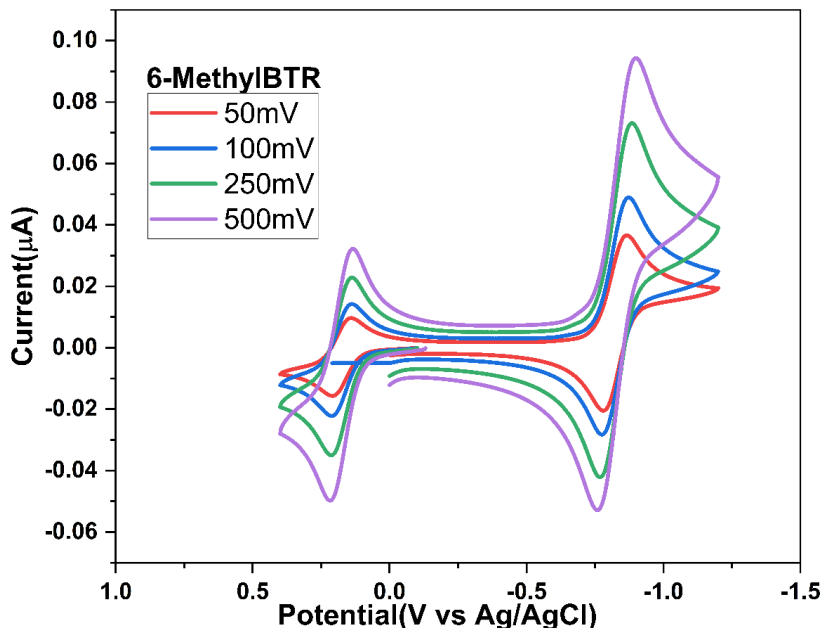


Figure 1. 24 Cyclic voltammograms of radical 1.3 in MeCN with 0.1 M [Bu₄N][PF₆] supporting electrolyte, glassy carbon working electrode, silver reference electrode, platinum counter electrode, 50-500 mV/s scan rate

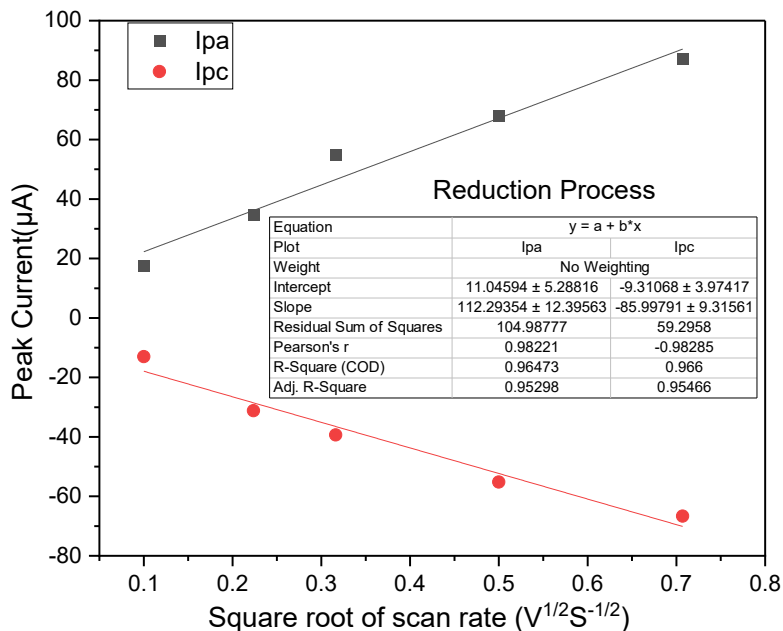


Figure 1. 25 Peak currents (i_{pc} and i_{pa}) from CV data vs. $v^{1/2}$ used to determine the diffusion coefficient from Randles Sevcik equation (see equation (S1) for radical 1.3. Lines are least-squares fits to the data

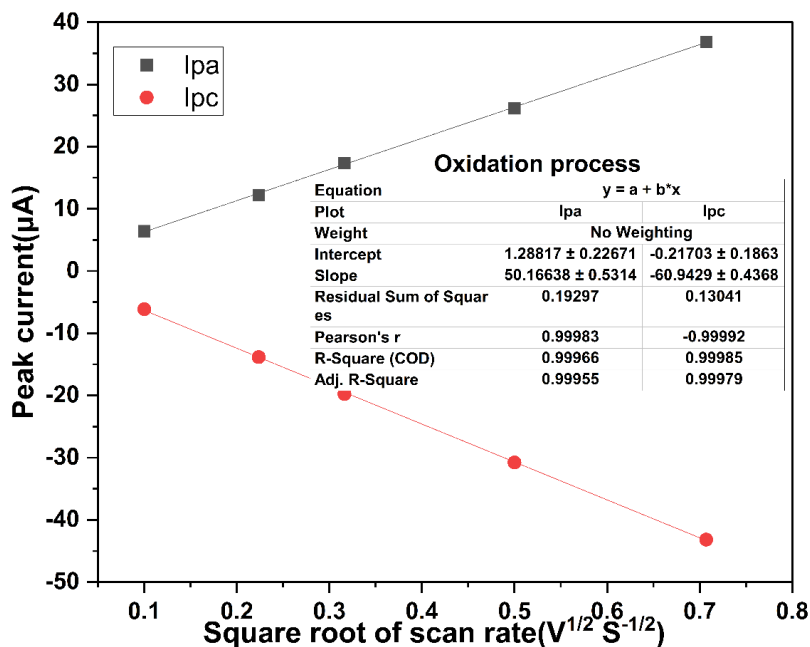


Figure 1. 26 Peak currents (i_{pc} and i_{pa}) from CV data vs. $v^{1/2}$ used to determine the diffusion coefficient from Randles Sevcik equation (see equation (S2)) for radical 1.3. Lines are least-squares fits to the data

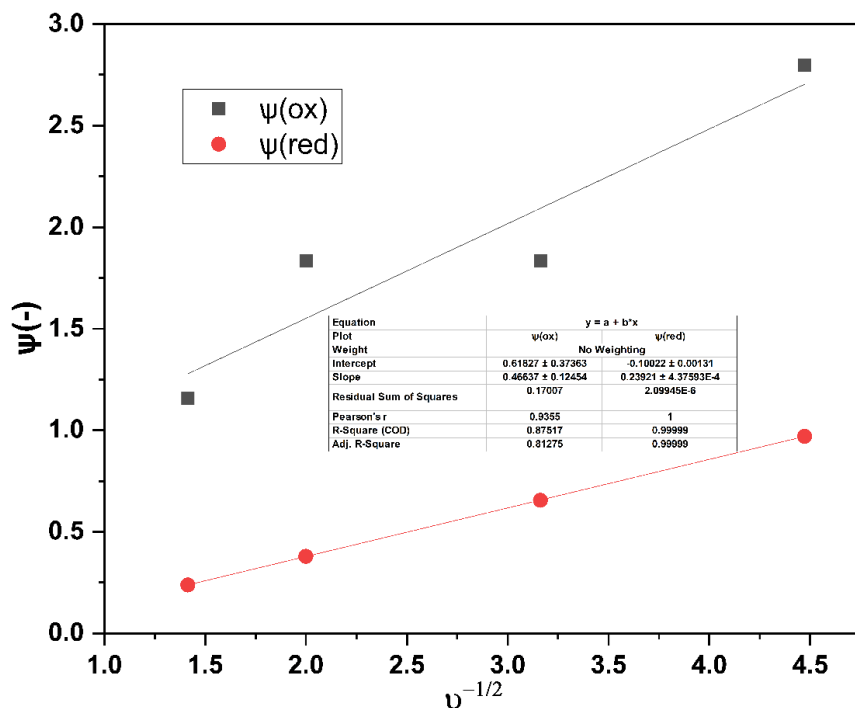


Figure 1. 27 Nicholson dimensionless coefficient Ψ (see Equation (S4 and S5)) vs. $v^{-1/2}$ used to determine the electron transfer rate constants k^0

2.8 Maximum solubility measurement for 1.4

Techno-economic analyses have shown that redox-active organic molecules (ROMs) must reach concentrations of roughly 1–2 molar to satisfy the energy-density requirements for commercially viable redox-flow batteries.¹¹² Among the series studied, compound 1.1 displays the highest “average” heterogeneous electron-transfer rate constant (k^0), suggesting faster kinetics which by extension might mean superior cell performance relative to the other derivatives. To determine whether this kinetic advantage can be realized in practice, the compound’s maximum solubility was determined as solubility sets the upper limit on the electrolyte’s volumetric energy density.

A calibration curve based on Beer's law was generated by recording the spectra of four CH_3CN solutions containing 1.4 at known concentrations (0.05 mM, 0.025 mM, 0.0125 mM, and 0.00625 mM). Peak absorbance values at 270 nm were plotted against the corresponding concentrations and fitted linearly to obtain a calibration equation. To determine solubility, 26 mg of 1.1 was dissolved in 0.3 mL CH_3CN to prepare a saturated solution. A 1 μL aliquot of this solution was then diluted to 10 mL with CH_3CN , and the spectrum of the diluted solution was recorded. Based on the calibration curve, the maximum solubility of 1.4 in CH_3CN was determined to be **0.02 M**

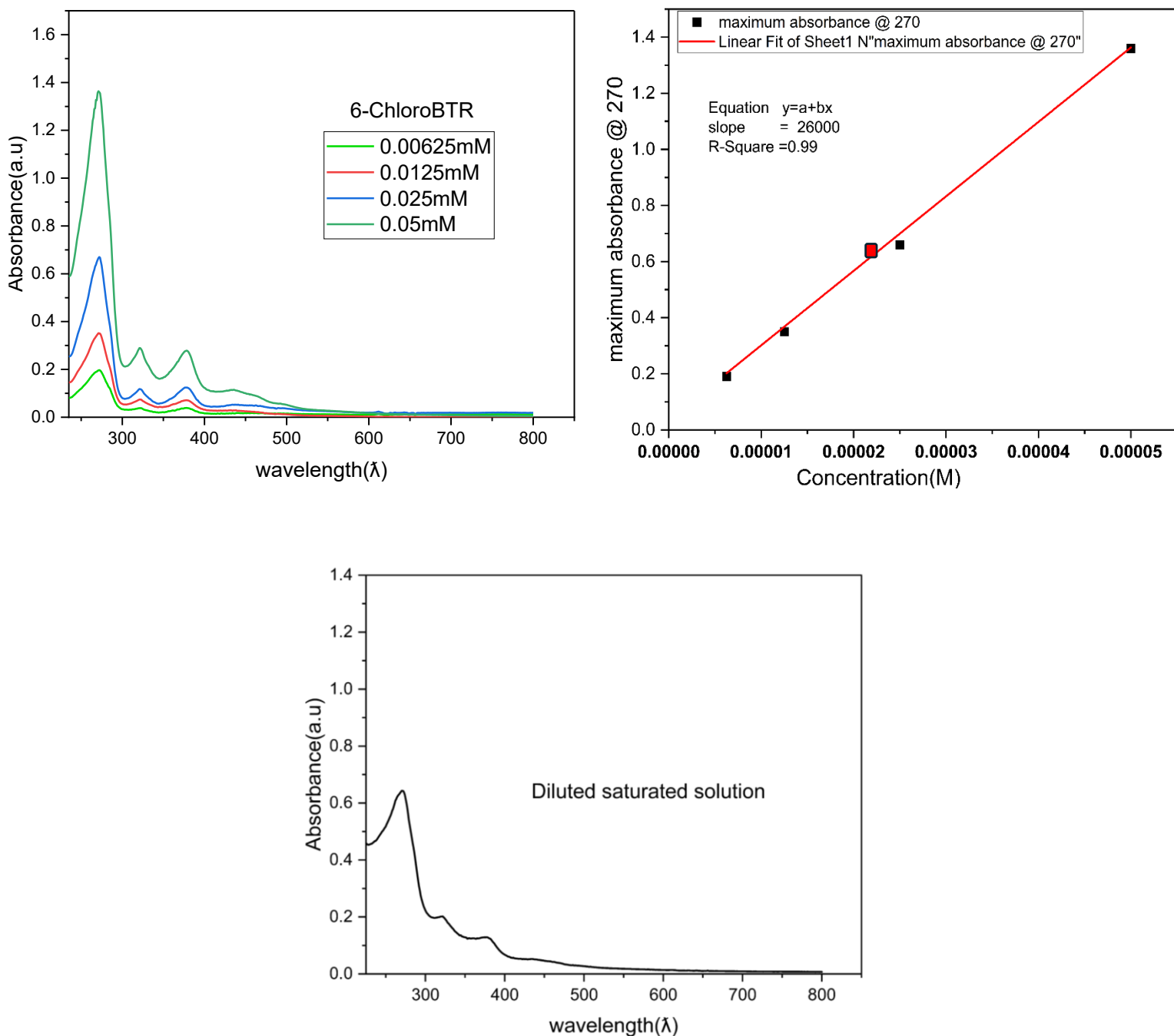


Figure 1. 28 Absorption spectra of 1.1 in CH₃CN at various concentrations. (top left). Calibration curve based on the peak absorbance maximum at 270 nm (top right). Absorption spectra for the saturated sample (bottom). red data point indicating sample concentration.

2.9 Conclusion

This work has demonstrated the successful synthesis and characterization of a series of functionalized benzotriazinyl radicals via a modular approach that offers tunability of both electronic and structural properties. The condensation–chlorination–amidrazone route provided access to several novel radicals, including 1.1, 1.2, 1.3, 1.4, and 1.4, with yields ranging from moderate to good. Importantly, the stepwise isolation of intermediates such as the amino leuco radical 1.12 enabled crystallographic confirmation of key structures, confirming insight into the mechanistic pathway of radical formation.

Spectroscopic and analytical data—including EPR, UV-Vis, IR, HRMS, and SC-XRD—collectively confirmed the successful formation and structural integrity of the radicals. Notably, the attempted synthesis of 6-functionalized amino radical revealed unexpected reactivity, forming an 8th amino leuco-radical intermediate that oxidized slowly in solution to the final product 1.1. This discovery highlighted the chemical sensitivity of the 8-amino substitution pattern and its role in influencing radical stability and transformation in situ.

These findings build upon and expand the understanding of structure–property relationships in the benzotriazinyl radical family. The knowledge gained here lays a strong foundation for the development of redox-active materials with potential applications in molecular electronics, magnetic materials, and organic energy storage systems.

3.0 Experimental

3.1.1 General Procedures and Characterization

All reagents were purchased from commercial suppliers (Sigma Aldrich, TCI, and Fisher Scientific) and used without further purification. ^1H and ^{13}C NMR spectra were recorded with a Bruker 500 or 400 MHz spectrometer with Me_4Si as the internal reference unless otherwise noted. FT-IR spectra were measured on a Thermo Nicolet 6700 Fourier transform infrared spectrometer (FT-IR). UV-vis spectra were obtained with an Agilent 8453 UV-Vis spectrometer. Mass spectra were recorded on an Agilent G6230B time-of-flight mass spectrometer (TOFMS) with electrospray ionization (ESI), atmospheric pressure photoionization (APPI), and atmospheric pressure chemical ionization (APCI) sources.

The following solvents were freshly distilled before Use: Ethanol. Chromatography (including flash chromatography) was performed with silica gel or alumina (neutral). All reactions were monitored by TLC performed on Aluminum-backed silica gel plates, and compounds were visualized under UV light. Quantum mechanical calculations were carried out at the UB3LYP/6-

31G(d,p) level of theory^{113,114} (unless stated otherwise) using the Gaussian 16 package. Geometry optimizations were performed without symmetry constraints Using time dependent DFT calculations supplied in the Gaussian 16.¹¹⁵

Syntheses

The synthesis and full characterization of compounds 1.1-1.5 and 1.0, using the methods discussed below have been previously reported.¹¹³

Benzaldehyde phenylhydrazone (1.17):¹¹⁶ Phenyl hydrazine (6.2 mL, 62 mmol) was added to a solution of benzaldehyde (6.0 mL, 60 mmol) in anhydrous ethanol (70 mL). The reaction solution was stirred at reflux under air for 40 minutes. It was then allowed to cool to room temperature, resulting in the formation of long white needle crystals. These were filtered, washed with hexanes, and dried under vacuum to yield purified 1.17 (8.01 g, 40.8 mmol, 68 %). ¹H NMR (500 MHz, cdcl₃) δ 7.94 (s, 1H), 7.92 – 7.90 (m, 2H), 7.86 (s, 1H), 7.65 – 7.60 (m, 2H), 7.58 – 7.51 (m, 3H), 7.51 (s, 1H), 7.40 – 7.35 (m, 2H), 7.13 (tt, *J* = 7.3, 1.1 Hz, 1H). ¹³C NMR (500 MHz, cdcl₃) δ 145.06, 137.66, 135.71, 129.70, 129.01, 128.83, 126.59, 120.53, 113.17, 77.67, 77.62, 77.41, 77.16, 0.40. FT-IR (ATR, v, cm⁻¹) 3312 (m), 3027 (w), 1602 (s), 1592 (s), 1566 (s), 1522 (s), 1494 (s), 1261 (s), 1066 (s), 929 (m), 750 (s), 691 (s), 504 (s) cm⁻¹.

Phenylhydrazone benzoyl chloride (1.18)¹¹⁶: A solution of N-chlorosuccinimide (9.0 g, 67 mmol) in dichloromethane (200 mL) was cooled to 0 °C in an ice bath. To this solution was added dimethyl sulfide (4.9 mL, 67 mmol), and the mixture was stirred for 10 minutes. A solution of 1.17 (10.3 g, 52 mmol) in 150 mL dichloromethane was then added dropwise over 10 minutes, and the reaction was stirred at 0 °C for a further 20 minutes. It was then warmed to room temperature and concentrated. The crude material was purified using silica gel flash chromatography (9:1 hexane: dichloromethane) to yield 1.18 as a white crystalline solid (5.72 g, 24.7 mmol, 60 %). ¹H NMR (500 MHz, CDCl₃) δ 8.06 (s, 1H), 7.99 – 7.89 (m, 2H), 7.47 – 7.37 (m, 3H), 7.37 – 7.30 (m, 2H), 7.25 – 7.18 (m, 2H), 6.97 (tt, *J* = 7.3, 1.2 Hz, 1H). ¹³C NMR (500 MHz, CDCl₃) δ 143.25, 134.35, 129.28, 129.10, 128.30, 126.31, 124.58, 121.07, 113.33. FT-IR (ATR, ν, cm⁻¹): 3306 (m), 3060 (w), 1601 (m), 1582 (m), 1505 (m), 1268 (m), 1137 (m), 942 (m), 755 (m), 684 (m), 510 (m) cm⁻¹

8-Amino-1,3-diphenyl-1,2,4-benzotriazinyl (1.1) A solution of m-Phenylamine (0.20 g, 1.8 mmol) and triethylamine (0.25 mL, 1.84 mmol) in 5 mL anhydrous ethanol was heated to reflux. A second solution of chlorohydrazone (0.20 g, 0.87 mmol) in 17.6 mL anhydrous ethanol was added dropwise to the refluxing solution over about 7 minutes. The reaction was then removed from the heat, treated with DBU (0.25 mL, 1.7 mmol), and then stirred for 18 hours at room temperature. The crude material was purified using silica gel chromatography (7:3 hexane: ethyl acetate) to yield 1.1 as a light green solid. (49 mg, 0.148 mmol, 17 %). FT-IR (ATR, ν, cm⁻¹): 3454 (w), 3380 (m), 3288 (w), 3162(w) 1624 (s), 1588 (m), 1517 (w), 1476 (s), 1455(s), 1341(w), 1323(w), 1262 (s),

1175 (m), 1206(w), 1168 (m), 1075 (m), 1030(w), 972(w), 759 (s), 739 (s), 712 (m), 696(s): (HRMS): m/z 299.13 (M⁺).

6-methyl-1,3-diphenyl-1,2,4-benzotriazinyl (1.3) A solution of 3-methylamine (0.19 mL, 1.8 mmol) and triethylamine (0.14 mL, 1.00 mmol) in 5 mL anhydrous ethanol was heated to reflux. A second solution of chlorohydrazone (0.20 g, 0.87 mmol) in 6 mL anhydrous ethanol was added dropwise to the refluxing solution over about 7 minutes. The reaction was then removed from the heat, treated with DBU (0.25 mL, 1.7 mmol), and then stirred for 18 hours at room temperature. The crude material was purified using silica gel chromatography (9:1 hexane: ethyl acetate) to yield **1.4** as a dark solid (155 mg, 0.52 mmol, 60 %). FT-IR (ATR, ν , cm^{-1}) 3058 (w), 2916 (w), 2851 (w), 1585 (w), 1487(s), 1451 (s), 1390(s), 1317 (m), 1179 (m), 1025 (m), 769 (s), 692 (s).: (HRMS): m/z 298.143 (M⁺).

6-methoxy-1,3-diphenyl-1,2,4-benzotriazinyl (1.4) A solution of 3-methylamine (0.19 mL, 1.8 mmol) and triethylamine (0.14 mL, 1.00 mmol) in 5 mL anhydrous ethanol was heated to reflux. A second solution of chlorohydrazone (0.20 g, 0.87 mmol) in 6 mL anhydrous ethanol was added dropwise to the refluxing solution over about 7 minutes. The reaction was then removed from the heat, treated with DBU (0.25 mL, 1.7 mmol), and then stirred for 18 hours at room temperature. The crude material was purified using silica gel chromatography (9:1 hexane: ethyl acetate) to yield **1.4** as a dark solid (133 mg, 0.42 mmol, 49 %). FT-IR (ATR, ν , cm^{-1}) 2922 (w), 2849 (w), 1595 (w), 1556 (w),

1485(m), 1455 (m), 1388 (m), 1356 (m), 1292 (w,) 1175 (m), 1130 (m), 1027 (m), 844 (m), 765 (m), 693 (m), 504 (s) : (HRMS): m/z 298.143 (M+).

6-chloro-1,3-diphenyl-1,2,4-benzotriazinyl (1.4) A solution of 4-chloroaniline (0.19 mL, 1.8 mmol) and triethylamine (0.14 mL, 1.0 mmol) in 5 mL anhydrous ethanol was heated to reflux. A second solution of 1.18 (0.20 g, 0.87 mmol) in 5 mL anhydrous ethanol was added dropwise to the refluxing solution over about 5 minutes. The reaction was then removed from the heat, treated with DBU (0.25 mL, 1.7 mmol), and then stirred for 18 hours at room temperature. The crude material was purified using silica gel chromatography (9:1 hexane: ethyl acetate) to yield **1.1** as a dark solid. (110 mg, 0.34 mmol, 40 %). FT-IR (ATR, ν , cm^{-1}) 3059 (w), 2917 (w), 2843 (w), 1588 (w), 1476(s), 1449 (m), 1384(s), 1318 (m), 1279 (m) 1072 (m), 1022 (m), 848 (s) , 694 (s) : (HRMS): m/z 318.089 (M+).

6-Nitro-1,3-diphenyl-1,2,4-benzotriazinyl (1.5) A solution of 3-NitroN-Phenylbenzamide phenylhydrazone (0.26g, 0.78 mmol), Mercury oxide HgO (0.78g, 3.2mmol) in 23mL anhydrous ethanol was refluxed for 3-4 days. The reaction was then removed from heat and concentrated. The crude material was purified using silica gel chromatography (9:1 hexane: ethyl acetate) to yield **1.3** as a dark solid. (85 mg, 0.26 mmol 33%) FT-IR (ATR, ν , cm^{-1}) 3212 (w), 3058 (w), 1734 (m), 1589 (m), 1525(s), 1340 (s), 1284(s), 1318 (m), 1252 (m) 1168 (m), 1108 (m), 987 (m) , 824 (m), 749(s) , 690 (s) : (HRMS): m/z 329.121 (M+).

3-Nitro-N-Phenylbenzamide phenylhydrazone (1.8) A solution of phenylchlorohydrazone (0.60 g, 2.6 mmol), 3-nitroaniline (0.74g, 5.4 mmol), and triethylamine (0.42 mL, 2.5 mmol) in ethanol (200 mL) was stirred in a nitrogen atmosphere for 3 hours at 70—90 °C.: The crude material was purified using silica gel chromatography (8:2 hexanes: ethyl acetate) to yield an orange/red crystalline solid (0.43g , 1.30 mmol 50-60%).¹H NMR (500 MHz, cdcl₃) δ 7.76 (dt, *J* = 7.4, 1.1 Hz, 0H), 7.74 – 7.71 (m, 2H), 7.69 – 7.57 (m, 1H), 7.41 – 7.38 (m, 3H), 7.36 (d, *J* = 8.2 Hz, 1H), 7.33 – 7.26 (m, 2H), 7.16 (d, *J* = 7.9 Hz, 2H), 6.96 – 6.88 (m, 2H), 5.79 (s, 1H)..¹³C NMR (500 MHz, cdcl₃) δ 149.27, 144.49, 142.84, 134.05, 130.35, 126.12, 115.41, 113.48, 110.34. FT-IR (ATR, ν, cm⁻¹) 3247 (s), 3059 (w), 1734 (m), 1593(s), 1516(s), 1332 (s), 1237(s), 1130 (s), 1058 (w) 734 (s), 685 (s), MS (ESI-TOF): m/z 333.138 (M+H).

Chapter 3

3.1 Conclusion and outlook

This work has demonstrated the successful synthesis, characterization, and electrochemical evaluation of a series of 6-position functionalized 1,3-diphenyl-1,2,4-benzotriazinyl radicals (6-X-BTR, X = H, Cl, CH₃, NH₂, NO₂, OMe) as candidate redox-active materials for non-aqueous, symmetric redox flow batteries (RFBs). The overall goal was to investigate how substituent effects at the 6-position influence redox potentials, electron-transfer kinetics, spin density distribution, and stability, with the broader aim of informing the design of high-performance organic redox-active molecules (ROMs) for energy storage.

The synthetic strategies employed enabled access to each target radical in moderate to good yields, with structural confirmation achieved via a combination of spectroscopic (UV-Vis, EPR, HRMS) and, in selected cases, single-crystal X-ray diffraction (SCXRD) analyses. Of note, the crystallographic characterization of an unexpected 8-amino-functionalized leuco radical intermediate revealed important steric and electronic factors that can influence the oxidation process to the target radical. Time-dependent UV-Vis monitoring confirmed a slow, oxygen-mediated conversion to the benzotriazinyl radical over 14–15 hours, underscoring the sensitivity of certain substitution patterns.

Electrochemical studies by cyclic voltammetry revealed that all stable radical derivatives exhibit bipolar electrochemistry, with reversible oxidation and reduction processes. The redox potentials were found to be tunable through electronic effects of the substituents: electron-withdrawing groups (e.g., $-\text{Cl}$, $-\text{NO}_2$) anodically shifted the reduction potential, thereby stabilizing the radical anion, while electron-donating groups had the opposite effect. The resulting cell voltages were in the range of ~ 1.0 V, which, while modest, are promising for symmetric RFB operation.

Heterogeneous electron-transfer rate constants (k^0), determined via the Nicholson method, indicated that the 6-Cl-BTR derivative exhibited faster electron-transfer kinetics for oxidation, while the 6-OMe-BTR has a faster electron transfer kinetic for reduction compared to a benchmark parent radical from literature, suggesting that judicious substituent choice can improve kinetic performance. Spin density mapping from room-temperature EPR, supported by DFT calculations, correlated substituent electronic effects with redistribution of spin density across the benzotriazinyl framework, offering a mechanistic basis for the observed electrochemical trends.

Overall, these results confirm that benzotriazinyl radicals remain a highly tunable platform for ROM development, combining chemical stability, reversible bipolar electrochemistry, and substituent-modulated kinetics. The findings highlight the potential of these radicals as building blocks for next-generation non-aqueous redox flow batteries, provided further improvements in voltage and solubility can be achieved.

In addition, improving the solubility of the derivatives remains an important goal. Incorporation of solubilizing groups—such as poly (ethylene glycol) (PEG) chains, sulfonates, or other polar substituents—into the BTR architecture could significantly enhance solubility in aqueous electrolytes. The leuco radical derivative also presents a promising avenue for further exploration, particularly for its potential in polymerization. A deeper investigation into the role of the leuco intermediate in dictating redox chemistry is warranted. Blocking the C-6 and C-8 positions may afford a more stable leuco radical that can be harnessed in polymeric materials. Furthermore, dual substitution at both C-6 and C-8 could enhance leuco radical stability while enabling fine control of redox behavior through combined electronic and steric effects. Such design strategies may yield novel leuco-radical-based materials with potential applications in slow-response oxygen sensors or advanced charge-storage platforms.

Through this work, it is now established that a 1,2-diamine affords a C-5 functionalized radical, whereas a 1,3-diamine does not yield the expected C-6 functionalized benzotriazinyl radical. Instead, the reaction produces a zwitterionic species along with a C-8 functionalized radical. The underlying cause of this divergence remains unclear and warrants further investigation. It is possible that differences in connectivity, electronic effects, and steric constraints between the 1,2- and 1,3-diamines alter the cyclization pathway, thereby directing product formation away from the anticipated C-6 substitution.

Detailed mechanistic studies—both experimental and computational—could clarify the origin of this selectivity and guide synthetic strategies for targeting specific substitution patterns.

References

- (1) International Energy Outlook 2016. **2016**.
- (2) Winsberg, J.; Hagemann, T.; Janoschka, T.; Hager, M. D.; Schubert, U. S. Redox-Flow Batteries: From Metals to Organic Redox-Active Materials. *Angew. Chem. Int. Ed.* **2017**, *56* (3), 686–711. <https://doi.org/10.1002/anie.201604925>.
- (3) Verbruggen, A. Renewable and Nuclear Power: A Common Future? *Energy Policy* **2008**, *36* (11), 4036–4047. <https://doi.org/10.1016/j.enpol.2008.06.024>.
- (4) Huang, Y.; Gu, S.; Yan, Y.; Li, S. F. Y. Nonaqueous Redox-Flow Batteries: Features, Challenges, and Prospects. *Curr. Opin. Chem. Eng.* **2015**, *8*, 105–113. <https://doi.org/10.1016/j.coche.2015.04.001>.
- (5) Nykvist, B.; Nilsson, M. Rapidly Falling Costs of Battery Packs for Electric Vehicles. *Nat. Clim. Change* **2015**, *5* (4), 329–332. <https://doi.org/10.1038/nclimate2564>.
- (6) *Materials and Systems for Organic Redox Flow Batteries: Status and Challenges*. <https://doi.org/10.1021/acsenergylett.7b00650>.
- (7) Wang, W.; Luo, Q.; Li, B.; Wei, X.; Li, L.; Yang, Z. Electroactive Materials for Next-Generation Redox Flow Batteries: From Inorganic to Organic. *Adv. Funct. Mater.* **2013**, *23* (8), 970–986. <https://doi.org/10.1002/adfm.201200694>.

- (8) Soloveichik, G. L. Flow Batteries: Current Status and Trends. *Chem. Rev.* **2015**, *115* (20), 11533–11558. <https://doi.org/10.1021/cr500720t>.
- (9) Weber, A. Z.; Mench, M. M.; Meyers, J. P.; Ross, P. N.; Gostick, J. T.; Liu, Q. Redox Flow Batteries: A Review. *J. Appl. Electrochem.* **2011**, *41* (10), 1137–1164. <https://doi.org/10.1007/s10800-011-0348-2>.
- (10) *Blatter Radicals as Bipolar Materials for Symmetrical Redox-Flow Batteries.* <https://doi.org/10.1021/jacs.1c13543>.
- (11) RWE. *RWE connects its first utility-scale battery storage project to the California grid.* <https://americas.rwe.com/press/2023-06-14-rwe-connects-its-first-utility-scale-battery-storage-project-to-the-california-grid/> (accessed 2025-07-26).
- (12) Ding, Y.; Zhang, C.; Zhang, L.; Zhou, Y.; Yu, G. Molecular Engineering of Organic Electroactive Materials for Redox Flow Batteries. *Chem. Soc. Rev.* **2018**, *47* (1), 69–103. <https://doi.org/10.1039/C7CS00569E>.
- (13) Bartolozzi, M. Development of Redox Flow Batteries. A Historical Bibliography. *J. Power Sources* **1989**, *27* (3), 219–234. [https://doi.org/10.1016/0378-7753\(89\)80037-0](https://doi.org/10.1016/0378-7753(89)80037-0).
- (14) Skyllas-Kazacos, M.; Rychcik, M.; Robins, R. G.; Fane, A. G.; Green, M. A. New All-Vanadium Redox Flow Cell. *J. Electrochem. Soc.* **1986**, *133* (5), 1057. <https://doi.org/10.1149/1.2108706>.

- (15) Rychcik, M.; Skyllas-Kazacos, M. Characteristics of a New All-Vanadium Redox Flow Battery. *J. Power Sources* **1988**, *22* (1), 59–67. [https://doi.org/10.1016/0378-7753\(88\)80005-3](https://doi.org/10.1016/0378-7753(88)80005-3).
- (16) Alotto, P.; Guarnieri, M.; Moro, F. Redox Flow Batteries for the Storage of Renewable Energy: A Review. *Renew. Sustain. Energy Rev.* **2014**, *29*, 325–335. <https://doi.org/10.1016/j.rser.2013.08.001>.
- (17) Li, M.; Odom, S.; Pancoast, A.; Robertson, L.; Vaid, T.; Agarwal, G.; Doan, H.; Wang, Y.; Suduwella, T.; Bheemireddy, S.; Ewoldt, R.; Assary, R.; Zhang, L.; Sigman, M.; Minteer, S. Experimental Protocols for Studying Organic Non-Aqueous Redox Flow Batteries. *ACS ENERGY Lett.* **2021**, *6* (11), 3932–3943. <https://doi.org/10.1021/acsenergylett.1c01675>.
- (18) Rhodes, Z.; Cabrera-Pardo, J.; Li, M.; Minteer, S. Electrochemical Advances in Non-Aqueous Redox Flow Batteries. *Isr. J. Chem.* **2021**, *61* (1–2), 101–112. <https://doi.org/10.1002/ijch.202000049>.
- (19) Singh, P. Application of Non-Aqueous Solvents to Batteries. *J. Power Sources* **1984**, *11* (1), 135–142. [https://doi.org/10.1016/0378-7753\(84\)80079-8](https://doi.org/10.1016/0378-7753(84)80079-8).
- (20) Matsuda, Y.; Tanaka, K.; Okada, M.; Takasu, Y.; Morita, M.; Matsumura-Inoue, T. A Rechargeable Redox Battery Utilizing Ruthenium Complexes with Non-Aqueous Organic Electrolyte. *J. Appl. Electrochem.* **1988**, *18* (6), 909–914. <https://doi.org/10.1007/BF01016050>.

- (21) Liang, Z.; Jha, R.; Suduwella, T.; Attanayake, N.; Wang, Y.; Zhang, W.; Cao, C.; Kaur, A.; Landon, J.; Odom, S. A Prototype of High-Performance Two-Electron Non-Aqueous Organic Redox Flow Battery Operated at -40 Degrees C. *J. Mater. Chem. A* **2022**, *10* (46), 24685–24693. <https://doi.org/10.1039/d2ta07876g>.
- (22) S. Tracy, J.; S. Horst, E.; A. Roytman, V.; Dean Toste, F. Development of High-Voltage Bipolar Redox-Active Organic Molecules through the Electronic Coupling of Catholyte and Anolyte Structures. *Chem. Sci.* **2022**, *13* (36), 10806–10814. <https://doi.org/10.1039/D2SC03450F>.
- (23) Zhang, J.; Yang, Z.; Shkrob, I. A.; Assary, R. S.; Tung, S. on; Silcox, B.; Duan, W.; Zhang, J.; Su, C. C.; Hu, B.; Pan, B.; Liao, C.; Zhang, Z.; Wang, W.; Curtiss, L. A.; Thompson, L. T.; Wei, X.; Zhang, L. Annulated Dialkoxybenzenes as Catholyte Materials for Non-Aqueous Redox Flow Batteries: Achieving High Chemical Stability through Bicyclic Substitution. *Adv. Energy Mater.* **2017**, *7* (21), 1701272. <https://doi.org/10.1002/aenm.201701272>.
- (24) Winsberg, J.; Hagemann, T.; Janoschka, T.; Hager, M. D.; Schubert, U. S. Redox-Flow Batteries: From Metals to Organic Redox-Active Materials. *Angew. Chem. Int. Ed.* **2017**, *56* (3), 686–711. <https://doi.org/10.1002/anie.201604925>.
- (25) Chai, J.; Lashgari, A.; Jiang, J. “Jimmy.” Electroactive Materials for Next-Generation Redox Flow Batteries: From Inorganic to Organic. In *Clean Energy Materials*; ACS Symposium Series; American Chemical Society, 2020; Vol. 1364, pp 1–47. <https://doi.org/10.1021/bk-2020-1364.ch001>.

- (26) Sikukuu Nambafu, G. Organic Molecules as Bifunctional Electroactive Materials for Symmetric Redox Flow Batteries: A Mini Review. *Electrochem. Commun.* **2021**, *127*, 107052. <https://doi.org/10.1016/j.elecom.2021.107052>.
- (27) Lai, Y. Y.; Li, X.; Zhu, Y. Polymeric Active Materials for Redox Flow Battery Application. *ACS Appl. Polym. Mater.* **2020**, *2* (2), 113–128. <https://doi.org/10.1021/acsapm.9b00864>.
- (28) Yang, Y.; Zheng, G.; Cui, Y. A Membrane-Free Lithium/Polysulfide Semi-Liquid Battery for Large-Scale Energy Storage. *Energy Environ. Sci.* **2013**, *6* (5), 1552–1558. <https://doi.org/10.1039/C3EE00072A>.
- (29) Duan, W.; Vemuri, R. S.; Milshtein, J. D.; Laramie, S.; Dmello, R. D.; Huang, J.; Zhang, L.; Hu, D.; Vijayakumar, M.; Wang, W.; Liu, J.; Darling, R. M.; Thompson, L.; Smith, K.; Moore, J. S.; Brushett, F. R.; Wei, X. A Symmetric Organic-Based Nonaqueous Redox Flow Battery and Its State of Charge Diagnostics by FTIR. *J. Mater. Chem. A* **2016**, *4* (15), 5448–5456. <https://doi.org/10.1039/C6TA01177B>.
- (30) *Quinones for Aqueous Organic Redox Flow Battery: A Prospective on Redox Potential, Solubility, and Stability - Hasan - Advanced Materials Interfaces - Wiley Online Library*. <https://onlinelibrary.wiley.com/doi/full/10.1002/admi.202300268> (accessed 2023-08-15).
- (31) Zhou, W.; Liu, W.; Qin, M.; Chen, Z.; Xu, J.; Cao, J.; Li, J. Fundamental Properties of TEMPO-Based Catholytes for Aqueous Redox Flow Batteries: Effects of Substituent Groups and Electrolytes on Electrochemical Properties, Solubilities and

Battery Performance. *RSC Adv.* **2020**, *10* (37), 21839–21844.

<https://doi.org/10.1039/D0RA03424J>.

(32) *Reversible Reduction of the TEMPO Radical: One Step Closer to an All-Organic Redox Flow Battery* | *ACS Sustainable Chemistry & Engineering*.

<https://pubs.acs.org/doi/10.1021/acssuschemeng.0c05687> (accessed 2023-08-15).

(33) Wei, X.; Xu, W.; Vijayakumar, M.; Cosimbescu, L.; Liu, T.; Sprenkle, V.; Wang, W. TEMPO-Based Catholyte for High-Energy Density Nonaqueous Redox Flow Batteries. *Adv. Mater.* **2014**, *26*. <https://doi.org/10.1002/adma.201403746>.

(34) Wei, X.; Xu, W.; Vijayakumar, M.; Cosimbescu, L.; Liu, T.; Sprenkle, V.; Wang, W. TEMPO-Based Catholyte for High-Energy Density Nonaqueous Redox Flow Batteries. *Adv. Mater. Deerfield Beach Fla* **2014**, *26* (45), 7649–7653.

<https://doi.org/10.1002/adma.201403746>.

(35) Chen, H.; Niu, Z.; Ye, J.; Zhang, C.; Zhang, X.; Zhao, Y. Multicore Ferrocene Derivative as a Highly Soluble Cathode Material for Nonaqueous Redox Flow Batteries. *ACS Appl. Energy Mater.* **2020**, *4*. <https://doi.org/10.1021/acsaem.0c02733>.

(36) Rubio-Presa, R.; Lubián, L.; Borlaf, M.; Ventosa, E.; Sanz, R. Addressing Practical Use of Viologen-Derivatives in Redox Flow Batteries through Molecular Engineering. *ACS Mater. Lett.* **2023**, *5* (3), 798–802.

<https://doi.org/10.1021/acsmaterialslett.2c01105>.

- (37) Lv, X.-L.; Sullivan, P.; Fu, H.-C.; Hu, X.; Liu, H.; Jin, S.; Li, W.; Feng, D. Dextrosil-Viologen: A Robust and Sustainable Anolyte for Aqueous Organic Redox Flow Batteries. *ACS Energy Lett.* **2022**, *7* (8), 2428–2434. <https://doi.org/10.1021/acsenergylett.2c01198>.
- (38) Janoschka, T.; Morgenstern, S.; Hiller, H.; Friebe, C.; Wolkersdörfer, K.; Häupler, B.; Hager, M. D.; Schubert, U. S. Synthesis and Characterization of TEMPO- and Viologen-Polymers for Water-Based Redox-Flow Batteries. *Polym. Chem.* **2015**, *6* (45), 7801–7811. <https://doi.org/10.1039/C5PY01602A>.
- (39) Hu, S.; Wang, L.; Yuan, X.; Xiang, Z.; Huang, M.; Luo, P.; Liu, Y.; Fu, Z.; Liang, Z. Viologen-Decorated TEMPO for Neutral Aqueous Organic Redox Flow Batteries. *Energy Mater. Adv.* **2021**, *2021*. <https://doi.org/10.34133/2021/9795237>.
- (40) Kowalski, J.; Casselman, M.; Kaur, A. P.; Milshtein, J.; Elliott, C.; Modekrutti, S.; Attanayake, N. H.; Zhang, N.; Parkin, S.; Risko, C.; Brushett, F.; Odom, S. A Stable Two-Electron-Donating Phenothiazine for Application in Nonaqueous Redox Flow Batteries. *J Mater Chem A* **2017**, *5*. <https://doi.org/10.1039/C7TA05883G>.
- (41) Yang, G.; Zhu, Y.; Hao, Z.; Lu, Y.; Zhao, Q.; Zhang, K.; Chen, J. Organic Electroactive Materials for Aqueous Redox Flow Batteries. *Adv. Mater.* *n/a* (n/a), 2301898. <https://doi.org/10.1002/adma.202301898>.
- (42) Zhang, C.; Niu, Z.; Peng, S.; Ding, Y.; Zhang, L.; Guo, X.; Zhao, Y.; Yu, G. Phenothiazine-Based Organic Catholyte for High-Capacity and Long-Life Aqueous

Redox Flow Batteries. *Adv. Mater. Deerfield Beach Fla* **2019**, *31* (24), e1901052.

<https://doi.org/10.1002/adma.201901052>.

(43) Shoaib, M.; Vallayil, P.; Jaiswal, N.; Iyapazham Vaigunda Suba, P.;

Sankararaman, S.; Ramanujam, K.; Thangadurai, V. Advances in Redox Flow Batteries – A Comprehensive Review on Inorganic and Organic Electrolytes and Engineering

Perspectives. *Adv. Energy Mater.* **2024**, *14* (32), 2400721.

<https://doi.org/10.1002/aenm.202400721>.

(44) Rugolo, J.; Aziz, M. J. Electricity Storage for Intermittent Renewable Sources.

Energy Environ. Sci. **2012**, *5* (5), 7151. <https://doi.org/10.1039/c2ee02542f>.

(45) Hasan, F.; Mahanta, V.; Abdelazeez, A. A. A. Quinones for Aqueous Organic Redox Flow Battery: A Prospective on Redox Potential, Solubility, and Stability. *Adv.*

Mater. Interfaces **2023**, *10* (24), 2300268. <https://doi.org/10.1002/admi.202300268>.

(46) Rogers, F. J. M.; Norcott, P. L.; Coote, M. L. Recent Advances in the Chemistry of Benzo[*e*][1,2,4]Triazinyl Radicals. *Org. Biomol. Chem.* **2020**, *18* (41), 8255–8277.

<https://doi.org/10.1039/d0ob01394c>.

(47) Keane, L.-A. J.; Mirallai, S. I.; Sweeney, M.; Carty, M. P.; Zissimou, G. A.;

Berezin, A. A.; Koutentis, P. A.; Aldabbagh, F. Anti-Cancer Activity of Phenyl and Pyrid-2-Yl 1,3-Substituted Benzo[1,2,4]Triazin-7-Ones and Stable Free Radical

Precursors. *Molecules* **2018**, *23* (3), 574. <https://doi.org/10.3390/molecules23030574>.

- (48) Gomberg, M. AN INSTANCE OF TRIVALENT CARBON: TRIPHENYLMETHYL. *J. Am. Chem. Soc.* **1900**, *22* (11), 757–771. <https://doi.org/10.1021/ja02049a006>.
- (49) Hicks, R. G. What's New in Stable Radical Chemistry? *Org. Biomol. Chem.* **2006**, *5* (9), 1321–1338. <https://doi.org/10.1039/B617142G>.
- (50) Blatter, H. M.; Lukaszewski, H. A New Stable Free Radical. *Tetrahedron Lett.* **1968**, *9* (22), 2701–2705. [https://doi.org/10.1016/S0040-4039\(00\)89678-1](https://doi.org/10.1016/S0040-4039(00)89678-1).
- (51) Ji, Y.; Long, L.; Zheng, Y. Recent Advances of Stable Blatter Radicals: Synthesis, Properties and Applications. *Mater. Chem. Front.* **2020**, *4* (12), 3433–3443. <https://doi.org/10.1039/D0QM00122H>.
- (52) Zheng, Y.; Miao, M.; Kemei, M. C.; Seshadri, R.; Wudl, F. The Pyreno-Triazinyl Radical – Magnetic and Sensor Properties. *Isr. J. Chem.* **2014**, *54* (5–6), 774–778. <https://doi.org/10.1002/ijch.201400034>.
- (53) Constantinides, C. P.; Koutentis, P. A.; Rawson, J. M. Antiferromagnetic Interactions in 1D Heisenberg Linear Chains of 7-(4-Fluorophenyl) and 7-Phenyl-Substituted 1,3-Diphenyl-1,4-Dihydro- 1,2,4-Benzotriazin-4-Yl Radicals. *Chem. – Eur. J.* **2012**, *18* (48), 15433–15438. <https://doi.org/10.1002/chem.201202784>.
- (54) Wang, H.; Sayed, S. Y.; Lubber, E. J.; Olsen, B. C.; Shirurkar, S. M.; Venkatakrisnan, S.; Tefashe, U. M.; Farquhar, A. K.; Smotkin, E. S.; McCreery, R. L.; Buriak, J. M. Redox Flow Batteries: How to Determine Electrochemical Kinetic

Parameters. *ACS Nano* **2020**, *14* (3), 2575–2584.

<https://doi.org/10.1021/acsnano.0c01281>.

(55) Steen, J. S.; Nuismer, J. L.; Eiva, V.; Wiglema, A. E. T.; Daub, N.; Hjelm, J.; Otten, E. Blatter Radicals as Bipolar Materials for Symmetrical Redox-Flow Batteries. *J. Am. Chem. Soc.* **2022**, *144* (11), 5051–5058. <https://doi.org/10.1021/jacs.1c13543>.

(56) Gopalakrishna, T. Y.; Zeng, W.; Lu, X.; Wu, J. From Open-Shell Singlet Diradicaloids to Polyradicaloids. *Chem. Commun.* **2018**, *54* (18), 2186–2199. <https://doi.org/10.1039/C7CC09949E>.

(57) Low, J. Z.; Kladnik, G.; Patera, L. L.; Sokolov, S.; Lovat, G.; Kumarasamy, E.; Repp, J.; Campos, L. M.; Cvetko, D.; Morgante, A.; Venkataraman, L. The Environment-Dependent Behavior of the Blatter Radical at the Metal–Molecule Interface. *Nano Lett.* **2019**, *19* (4), 2543–2548. <https://doi.org/10.1021/acs.nanolett.9b00275>.

(58) Verwendung benzotriazinyl-haltiger Polymere als Ladungsspeicher. **2017**.

(59) Ciccullo, F.; Calzolari, A.; Bader, K.; Neugebauer, P.; Gallagher, N. M.; Rajca, A.; Van Slageren, J.; Casu, M. B. Interfacing a Potential Purely Organic Molecular Quantum Bit with a Real-Life Surface. *ACS Appl. Mater. Interfaces* **2019**, *11* (1), 1571–1578. <https://doi.org/10.1021/acsami.8b16061>.

(60) Ballester, M. Inert Free Radicals (IFR): A Unique Trivalent Carbon Species. *Acc. Chem. Res.* **1985**, *18* (12), 380–387. <https://doi.org/10.1021/ar00120a004>.

- (61) Mukai, K. Anomalous Magnetic Properties of Stable Crystalline Phenoxy Radicals. *Bull. Chem. Soc. Jpn.* **1969**, *42* (1), 40–46. <https://doi.org/10.1246/bcsj.42.40>.
- (62) Manner, V. W.; Markle, T. F.; Freudenthal, J. H.; Roth, J. P.; Mayer, J. M. The First Crystal Structure of a Monomeric Phenoxy Radical: 2,4,6-Tri-Tert-Butylphenoxy Radical. *Chem. Commun.* **2007**, No. 2, 256–258. <https://doi.org/10.1039/B712872J>.
- (63) Brown, G. M.; Freeman, G. R.; Walter, R. I. Crystal Structure of Tri(*p*-Biphenyl)Aminium Perchlorate. *J. Am. Chem. Soc.* **1977**, *99* (21), 6910–6915. <https://doi.org/10.1021/ja00463a022>.
- (64) Allemand, P. M.; Srdanov, G.; Wudl, F. Molecular Engineering in the Design of Short-Range Ferromagnetic Exchange in Organic Solids: The 1,3,5-Triphenylverdazyl System. *J. Am. Chem. Soc.* **1990**, *112* (25), 9391–9392. <https://doi.org/10.1021/ja00181a050>.
- (65) Togashi, K.; Imachi, R.; Tomioka, K.; Tsuboi, H.; Ishida, T.; Nogami, T.; Takeda, N.; Ishikawa, M. Organic Radicals Exhibiting Intermolecular Ferromagnetic Interactions with High Probability: 4-Arylmethyleneamino-2,2,6,6-Tetramethylpiperidin-1-Yloxy and Related Compounds. *Bull. Chem. Soc. Jpn.* **1996**, *69* (10), 2821–2830. <https://doi.org/10.1246/bcsj.69.2821>.
- (66) Tamura, M.; Nakazawa, Y.; Shiomi, D.; Nozawa, K.; Hosokoshi, Y.; Ishikawa, M.; Takahashi, M.; Kinoshita, M. Bulk Ferromagnetism in the β -Phase Crystal of the *p*-Nitrophenyl Nitronyl Nitroxide Radical. *Chem. Phys. Lett.* **1991**, *186* (4), 401–404. [https://doi.org/10.1016/0009-2614\(91\)90198-I](https://doi.org/10.1016/0009-2614(91)90198-I).

- (67) Rawson, J. Benzo-Fused Dithiazolyl Radicals: From Chemical Curiosities to Materials Chemistry. *Coord. Chem. Rev.* **1999**, *189* (1), 135–168.
[https://doi.org/10.1016/S0010-8545\(99\)00118-6](https://doi.org/10.1016/S0010-8545(99)00118-6).
- (68) Gomberg, M. Triphenylmethyl, Ein Fall von Dreiwertigem Kohlenstoff. *Berichte Dtsch. Chem. Ges.* **1900**, *33* (3), 3150–3163.
<https://doi.org/10.1002/cber.19000330369>.
- (69) *The Chemistry of Free Radicals by Waters W.A.:: (1948) | Kerr & Sons Booksellers ABA.* <https://www.abebooks.com/Chemistry-Free-Radicals-Waters-W.A-Oxford/13231229484/bd> (accessed 2025-08-10).
- (70) Bank, S.; Ehrlich, C. L.; Zubieta, J. A. Substituent Effect on the Electrochemical Oxidation of Trityl Anions. *J. Org. Chem.* **1979**, *44* (9), 1454–1458.
<https://doi.org/10.1021/jo01323a020>.
- (71) Wu, P.; O'Malley, P. J. Environmental Effects on Phenoxy Free Radical Spin Densities and Hyperfine Couplings. *J. Mol. Struct. THEOCHEM* **2005**, *730* (1–3), 251–254. <https://doi.org/10.1016/j.theochem.2005.06.034>.
- (72) Nishide, H.; Miyasaka, M.; Tsuchida, E. Average Octet Radical Polymer: A Stable Polyphenoxy with Star-Shaped π Conjugation. *Angew. Chem. Int. Ed.* **1998**, *37* (17), 2400–2402. [https://doi.org/10.1002/\(SICI\)1521-3773\(19980918\)37:17<2400::AID-ANIE2400>3.0.CO;2-0](https://doi.org/10.1002/(SICI)1521-3773(19980918)37:17<2400::AID-ANIE2400>3.0.CO;2-0).

- (73) Nishide, H.; Miyasaka, M.; Tsuchida, E. High-Spin Polyphenoxyls Attached to Star-Shaped Poly(Phenylenevinylene)s. *J. Org. Chem.* **1998**, *63* (21), 7399–7407. <https://doi.org/10.1021/jo981090h>.
- (74) Kaneko, T.; Makino, T.; Miyaji, H.; Teraguchi, M.; Aoki, T.; Miyasaka, M.; Nishide, H. Ladderlike Ferromagnetic Spin Coupling Network on a π -Conjugated Pendant Polyradical. *J. Am. Chem. Soc.* **2003**, *125* (12), 3554–3557. <https://doi.org/10.1021/ja026929w>.
- (75) Nishide, H.; Miyasaka, M.; Doi, R.; Araki, T. Poly(1,2-Phenylenevinylene) Ferromagnetically 3,5-Bearing Phenoxy Radicals. *Macromolecules* **2002**, *35* (3), 690–698. <https://doi.org/10.1021/ma011209f>.
- (76) Nishide, H.; Kaneko, T.; Nii, T.; Katoh, K.; Tsuchida, E.; Lahti, P. M. Poly(Phenylenevinylene)-Attached Phenoxy Radicals: Ferromagnetic Interaction through Planarized and π -Conjugated Skeletons. *J. Am. Chem. Soc.* **1996**, *118* (40), 9695–9704. <https://doi.org/10.1021/ja961721u>.
- (77) Miyasaka, M.; Yamazaki, T.; Tsuchida, E.; Nishide, H. Regioregular Polythiophene with Pendant Phenoxy Radicals: A New High-Spin Organic Polymer. *Macromolecules* **2000**, *33* (22), 8211–8217. <https://doi.org/10.1021/ma000993l>.
- (78) Nishide, H.; Kaneko, T.; Nii, T.; Katoh, K.; Tsuchida, E.; Yamaguchi, K. Through-Bond and Long-Range Ferromagnetic Spin Alignment in a π -Conjugated Polyradical with a Poly(Phenylenevinylene) Skeleton. *J. Am. Chem. Soc.* **1995**, *117* (1), 548–549. <https://doi.org/10.1021/ja00106a070>.

- (79) Nishide, H.; Iwasa, S.; Pu, Y.-J.; Suga, T.; Nakahara, K.; Satoh, M. Organic Radical Battery: Nitroxide Polymers as a Cathode-Active Material. *Electrochimica Acta* **2004**, *50* (2), 827–831. <https://doi.org/10.1016/j.electacta.2004.02.052>.
- (80) Walter, R. I. Triarylamminium Salt Free Radicals¹. *J. Am. Chem. Soc.* **1955**, *77* (22), 5999–6002. <https://doi.org/10.1021/ja01627a061>.
- (81) Magnan, F.; Dhindsa, J. S.; Anghel, M.; Bazylewski, P.; Fanchini, G.; Gilroy, J. B. A Divergent Strategy for the Synthesis of Redox-Active Verdazyl Radical Polymers. *Polym. Chem.* **2021**, *12* (18), 2786–2797. <https://doi.org/10.1039/d1py00217a>.
- (82) Ullman, E. F.; Osiecki, J. H.; Boocock, D. G. B.; Darcy, R. Stable Free Radicals. X. Nitronyl Nitroxide Monoradicals and Biradicals as Possible Small Molecule Spin Labels. *J. Am. Chem. Soc.* **1972**, *94* (20), 7049–7059. <https://doi.org/10.1021/ja00775a031>.
- (83) Nakahara, K.; Iriyama, J.; Iwasa, S.; Suguro, M.; Satoh, M.; Cairns, E. J. Cell Properties for Modified PTMA Cathodes of Organic Radical Batteries. *J. Power Sources* **2007**, *165* (1), 398–402. <https://doi.org/10.1016/j.jpowsour.2006.11.044>.
- (84) Alberola, A.; Less, R. J.; Pask, C. M.; Rawson, J. M.; Palacio, F.; Oliete, P.; Paulsen, C.; Yamaguchi, A.; Farley, R. D.; Murphy, D. M. A Thiazyl-Based Organic Ferromagnet. *Angew. Chem.* **2003**, *115* (39), 4930–4933. <https://doi.org/10.1002/ange.200352194>.

- (85) Areephong, J.; Mattson, K. M.; Treat, N. J.; Poelma, S. O.; Kramer, J. W.; Sprafke, H. A.; Latimer, A. A.; Read De Alaniz, J.; Hawker, C. J. Triazine-Mediated Controlled Radical Polymerization: New Unimolecular Initiators. *Polym. Chem.* **2016**, *7* (2), 370–374. <https://doi.org/10.1039/C5PY01563D>.
- (86) Zheng, Y.; Miao, M.; Dantelle, G.; Eisenmenger, N. D.; Wu, G.; Yavuz, I.; Chabinyk, M. L.; Houk, K. N.; Wudl, F. A Solid-State Effect Responsible for an Organic Quintet State at Room Temperature and Ambient Pressure. *Adv. Mater.* **2015**, *27* (10), 1718–1723. <https://doi.org/10.1002/adma.201405093>.
- (87) Ren, Y. Recent Development of Benzotriazole-Based Medicinal Drugs. *Med. Chem.* **2014**, *4* (9). <https://doi.org/10.4172/2161-0444.1000207>.
- (88) Waldrep, T. W.; Beck, J. R.; Lynch, M. P.; Wright, F. L. Synthesis and Herbicidal Activity of 1-Aryl-5-Halo and 1-Aryl-5-(Trifluoromethyl)-1H-Pyrazole-4-Carboxamides. *J. Agric. Food Chem.* **1990**, *38* (2), 541–544. <https://doi.org/10.1021/jf00092a045>.
- (89) Hutchison, K. A. Conductive, Magnetic and Luminescent Materials Based on 1,3-Diphenyl-1,2,4-Benzotriazine. Ph.D., University of California, Santa Barbara, United States -- California, 1998.
<https://www.proquest.com/docview/304417886/abstract/595F1E578AD849BDPQ/1>
(accessed 2025-08-11).
- (90) Hanack, M.; Michel, U.; Winter, W. Darstellung und Molekülstruktur eines spirocyclischen Trisepoxids. *Chem. Ber.* **1981**, *114* (7), 2392–2398.
<https://doi.org/10.1002/cber.19811140705>.

- (91) Neugebauer, F. A.; Umminger, I. Über 1,4-Dihydro-1,2,4-benzotriazinyl-Radikale. *Chem. Ber.* **1980**, *113* (4), 1205–1225.
<https://doi.org/10.1002/cber.19801130402>.
- (92) Karecla, G.; Papagiorgis, P.; Panagi, N.; Zissimou, G. A.; Constantinides, C. P.; Koutentis, P. A.; Itskos, G.; Hayes, S. C. Emission from the Stable Blatter Radical. *New J. Chem.* **2017**, *41* (16), 8604–8613. <https://doi.org/10.1039/C7NJ00677B>.
- (93) Kadirov, M. K.; Il'yasov, A. V.; Vafina, A. A.; Buzykin, B. I.; Gazetdinova, N. G.; Kitaev, Yu. P. Double Electron-Nuclear Resonance of Free Radical 1,3-Diphenyl-1,4-Dihydro-1,2,4-Benzotriazin-4-Yl. *Bull. Acad. Sci. USSR Div. Chem. Sci.* **1984**, *33* (3), 649–650. <https://doi.org/10.1007/BF00995717>.
- (94) Kadirov, M. K.; Buzykin, B. I.; Gazetdinova, N. G. Electron Spin and Electron Nuclear Double Resonances of the Stable 1-(4-Nitrophenyl)-3-Phenyl-1,4-Dihydro-1,2,4-Benzotriazin-4-Yl Free Radical. *Russ. Chem. Bull.* **2002**, *51* (10), 1796–1799.
<https://doi.org/10.1023/A:1021331930462>.
- (95) Neugebauer, F. A.; Rimmler, G. ENDOR and Triple Resonance Studies of 1,4-Dihydro-1,2,4-Benzotriazinyl Radicals and 1,4-Dihydro-1,2,4-Benzotriazine Radical Cations. *Magn. Reson. Chem.* **1988**, *26* (7), 595–600.
<https://doi.org/10.1002/mrc.1260260712>.
- (96) Mukai, K.; Inoue, K.; Achiwa, N.; Jamali, J. B.; Krieger, C.; Neugebauer, F. A. Magnetic-Properties of 1,4-Dihydro-1,2,4-Benzotriazin -4-Yl Radicals. *Chem. Phys. Lett.* **1994**, *224* (5), 569–575. [https://doi.org/10.1016/0009-2614\(94\)00586-9](https://doi.org/10.1016/0009-2614(94)00586-9).

- (97) Neugebauer, F. A.; Umminger, I. 1,4-Dihydro-1,2,4-benzotriazin-Radikalkationen. *Chem. Ber.* **1981**, *114* (7), 2423–2430.
<https://doi.org/10.1002/cber.19811140709>.
- (98) Krieger, C.; Neugebauer, F. A. Columnar Stacking of 1,3-Diphenyl-1,2,4-Benzotriazin-4(1H)-Yl Radicals. *Acta Crystallogr. C* **1996**, *52* (12), 3124–3126.
<https://doi.org/10.1107/S0108270196011092>.
- (99) Hutchison, K. A.; Srdanov, G.; Menon, R.; Gabriel, J.-C. P.; Knight, B.; Wudl, F. A Pressure Sensitive Two-Dimensional Tetracyanoquinodimethane (TCNQ) Salt of a Stable Free Radical. *J. Am. Chem. Soc.* **1996**, *118* (51), 13081–13082.
<https://doi.org/10.1021/ja963174i>.
- (100) Hutchison, K.; Srdanov, G.; Hicks, R.; Yu, H.; Wudl, F.; Strassner, T.; Nendel, M.; Houk, K. N. Tetraphenylhexaazaanthracene: A Case for Dominance of Cyanine Ion Stabilization Overwhelming 16π Antiaromaticity. *J. Am. Chem. Soc.* **1998**, *120* (12), 2989–2990. <https://doi.org/10.1021/ja973558o>.
- (101) Constantinides, C. P.; Zissimou, G. A.; Berezin, A. A.; Ioannou, T. A.; Manoli, M.; Tsokkou, D.; Theodorou, E.; Hayes, S. C.; Koutentis, P. A. Tetraphenylhexaazaanthracenes: 16π Weakly Antiaromatic Species with Singlet Ground States. *Org. Lett.* **2015**, *17* (16), 4026–4029. <https://doi.org/10.1021/acs.orglett.5b01923>.
- (102) Krieger, C.; Neugebauer, F. A. Columnar Stacking of 1,3-Diphenyl-1,2,4-Benzotriazin-4(1H)-Yl Radicals. *Acta Crystallogr. Sect. C* **1996**, *52* (12), 3124–3126.
<https://doi.org/10.1107/S0108270196011092>.

- (103) Sheldrick, G. M. Crystal Structure Refinement with SHELXL. *Acta Crystallogr. Sect. C Struct. Chem.* **2015**, *71* (1), 3–8. <https://doi.org/10.1107/S2053229614024218>.
- (104) Dolomanov, O. V.; Bourhis, L. J.; Gildea, R. J.; Howard, J. a. K.; Puschmann, H. OLEX2: A Complete Structure Solution, Refinement and Analysis Program. *J. Appl. Crystallogr.* **2009**, *42* (2), 339–341. <https://doi.org/10.1107/S0021889808042726>.
- (105) Sheldrick, G. M. Crystal Structure Refinement with SHELXL. *Acta Crystallogr. Sect. C Struct. Chem.* **2015**, *71* (1), 3–8. <https://doi.org/10.1107/S2053229614024218>.
- (106) Muench, S.; Wild, A.; Friebe, C.; Häupler, B.; Janoschka, T.; Schubert, U. S. Polymer-Based Organic Batteries. *Chem. Rev.* **2016**, *116* (16), 9438–9484. <https://doi.org/10.1021/acs.chemrev.6b00070>.
- (107) Janoschka, T.; Hager, M. D.; Schubert, U. S. Powering up the Future: Radical Polymers for Battery Applications. *Adv. Mater.* **2012**, *24* (48), 6397–6409. <https://doi.org/10.1002/adma.201203119>.
- (108) Savva, A. C.; Mirallai, S. I.; Zissimou, G. A.; Berezin, A. A.; Demetriades, M.; Kourtellaris, A.; Constantinides, C. P.; Nicolaidis, C.; Trypiniotis, T.; Koutentis, P. A. Preparation of Blatter Radicals via Aza-Wittig Chemistry: The Reaction of N-Aryliminophosphoranes with 1-(Het)Aroyl-2-Aryldiazenes. *J. Org. Chem.* **2017**, *82* (14), 7564–7575. <https://doi.org/10.1021/acs.joc.7b01297>.

- (109) Sharmoukh, W. Redox Flow Batteries as Energy Storage Systems: Materials, Viability, and Industrial Applications. *RSC Adv.* **2025**, *15* (13), 10106–10143. <https://doi.org/10.1039/d5ra00296f>.
- (110) Berezin, A. A.; Constantinides, C. P.; Mirallai, S. I.; Manoli, M.; Cao, L. L.; Rawson, J. M.; Koutentis, P. A. Synthesis and Properties of Imidazolo-Fused Benzotriazinyl Radicals. *Org. Biomol. Chem.* **2013**, *11* (39), 6780–6795. <https://doi.org/10.1039/C3OB41169A>.
- (111) Nicholson, R. S. Theory and Application of Cyclic Voltammetry for Measurement of Electrode Reaction Kinetics. *Anal. Chem.* **1965**, *37* (11), 1351–1355. <https://doi.org/10.1021/ac60230a016>.
- (112) Singh, V.; Byon, H. R. Solubility and Stability of Redox-Active Organic Molecules in Redox Flow Batteries. *ACS Appl. Energy Mater.* **2024**, *7* (18), 7562–7575. <https://doi.org/10.1021/acsaem.3c02171>.
- (113) Becke, A. D. Density-functional Thermochemistry. III. The Role of Exact Exchange. *J. Chem. Phys.* **1993**, *98* (7), 5648–5652. <https://doi.org/10.1063/1.464913>.
- (114) Lee, C.; Yang, W.; Parr, R. G. Development of the Colle-Salvetti Correlation-Energy Formula into a Functional of the Electron Density. *Phys. Rev. B* **1988**, *37* (2), 785–789. <https://doi.org/10.1103/PhysRevB.37.785>.
- (115) Gaussian 16, Revision B.01, Frisch, M.J., Trucks, G.W., Schlegel, H.B., Scuseria, G.E., Robb, M.A., Cheeseman, J.R.; Scalmani, G.; Barone, V.; Petersson, G.A.;

Nakatsuji, H.; Li, X.; Caricato, M.; Marenich, A.V.; Bloino, J., Janesko, B.G., Gomperts, R., Mennucci, B., Hratchian, H.P., Ortiz, J.V., Izmaylov, A.F., Sonnenberg, J.L., Williams-Young, D., Ding, F., Lipparini, F., Egidi, F., Goings, J., Peng, B., Petrone, A., Henderson, T., Ranasinghe, D., Zakrzewski, V.G., Gao, J., Rega, N., Zheng, G., Liang, W., Hada, M., Ehara, M., Toyota, K., Fukuda, R., Hasegawa, J., Ishida, M., Nakajima, T., Honda, Y., Kitao, O., Nakai, H., Vreven, T., Throssell, K., Montgomery Jr., J.A., Peralta, J.E., Ogliaro, F., Bearpark, M.J., Heyd, J.J., Brothers, E.N., Kudin, K.N., Staroverov, V.N., Keith, T.A., Kobayashi, R., Normand, J., Raghavachari, K., Rendell, A.P., Burant, J.C., Iyengar, S.S., Tomasi, J., Cossi, M., Millam, J.M., Klene, M., Adamo, C., Cammi, R., Ochterski, J.W., Martin, R.L., Morokuma, K., Farkas, O., Foresman, J.B., Fox, D.J. Gaussian, Inc., Wallingford CT (2016) GaussView 5.0. Wallingford, E.U.A. - References - Scientific Research Publishing.

<https://scirp.org/reference/referencespapers?referenceid=2418053>.

(116) Content.Pdf. <https://dspace.library.uvic.ca/server/api/core/bitstreams/8b42d9ee-16c8-4195-9982-ef650bbd8c1f/content>.

Appendix A DFT calculation output parameters

Output parameters for 1.5(Nitro)

1\1\GINC-CPU-14\FOpt\UB3LYP\6-31G\C19H13N4O2(2)\KONYENWE\29-May-2024\0
\\# opt=tight ub3lyp/6-31g\6-NitroBTR\0,2\C,3.0028346398,-2.15704076
92,0.0650179538\C,1.6425815612,-2.4206896872,-0.0563219311\C,0.7311724
625,-1.352693238,-0.0572741271\C,1.2267103741,-0.0132089563,0.03964822
84\C,2.6091588712,0.2201661843,0.193698997\C,3.4947871965,-0.849101999
4,0.2031053401\H,1.2714628672,-3.4322488527,-0.1401527717\H,2.98280675
52,1.227700183,0.3127096965\H,4.5588760285,-0.6945275513,0.3195960986\
C,1.466897919,2.9236569732,-0.9654233073\C,0.5893620007,2.4024867561,-
0.0043173023\C,-0.0330313507,3.244856064,0.9257193434\C,0.2450491182,4
.6137761543,0.9062693633\C,1.1360407597,5.1412273544,-0.0369609229\C,1
.7424105458,4.2945538729,-0.9723376548\H,1.9109421144,2.2702930271,-1.
7078364203\H,-0.2331165309,5.2670598281,1.6281977931\H,1.3501221125,6.
2046025009,-0.0477874684\H,2.418437161,4.6999121607,-1.7175312358\C,-4
.7552137007,-2.4151762674,-0.0967419423\C,-5.6748263415,-1.3593167334,
-0.0630003253\C,-5.2146576058,-0.036609122,-0.0282974517\C,-3.84449446
66,0.2314691544,-0.0266541406\C,-2.9171312709,-0.8266928977,-0.0588150
859\C,-3.3837405228,-2.1532180165,-0.0946923667\H,-5.1065129787,-3.441
6173414,-0.1243339452\H,-3.48188908,1.2517412342,-0.0047844562\H,-2.66
03569312,-2.9586905465,-0.1210258818\N,0.2706351718,0.9991220296,0.004
9891681\N,-0.6235263189,-1.6188421624,-0.1279146559\N,-1.0925136835,0.
7382764873,0.011599005\C,-1.4615478139,-0.5654672331,-0.0546050856\H,-
0.7285819669,2.8234544646,1.640796298\H,-6.7406853514,-1.5649705738,-0
.0647502926\H,-5.9234647228,0.7849595058,-0.0045740045\N,3.9468767394,
-3.2666287105,0.065075823\O,5.1819120673,-2.9997017356,0.178520981\O,3
.4886128016,-4.4416238108,-0.0486370335\\Version=ES64L-G16RevA.03\Stat
e=2-A\HF=-1100.8617719\S2=0.770095\S2-1=0.\S2A=0.750213\RMSE=8.433e-09

\RMSF=3.948e-07\Dipole=-1.0160278,2.8023961,0.0815374\Quadrupole=-3.7844185,1.416863,2.3675555,19.1848663,-2.9325319,0.7973238\PG=C01 [X(C19H13N4O2)]\@

Output parameters for 1.6(OMe)

1\1\GINC-CPU-3\FOpt\UB3LYP\6-31G(d,p)\C20H16N3O1(2)\PRIMAL\13-Nov-2023
 \0\# opt ub3lyp/6-31g(d,p)\M-DIBTR\0,2\C,-7.2202313037,-2.628258581
 7,-0.5625934669\C,-5.9019680441,-3.0119651443,-0.3250139474\C,-4.88563
 72235,-2.0557443302,-0.1883071505\C,-5.2289972393,-0.6707101176,-0.261
 7169486\C,-6.5479124259,-0.2970944753,-0.5387339439\C,-7.5413424131,-1
 .2637282164,-0.6839855003\H,-5.6424345762,-4.0619327049,-0.2618260121\
 H,-6.8078373447,0.7478592362,-0.6506740519\H,-8.5538252367,-0.94453247
 6,-0.8965195735\C,-5.2985876832,2.2076692309,0.8445355086\C,-4.3389290
 869,1.6457795135,-0.0063892733\C,-3.4911608085,2.4720827112,-0.7533679
 039\C,-3.6215146547,3.8555662856,-0.6619986436\C,-4.5895917412,4.42253
 58068,0.1701141451\C,-5.4229311309,3.5940732911,0.9233200715\H,-5.9240
 350855,1.564765519,1.4537120283\H,-2.9653015924,4.4929709534,-1.246935
 5502\H,-4.6883469918,5.5015674033,0.2367427604\H,-6.1643609348,4.02544
 4077,1.5890715212\C,0.420902896,-3.6874479458,0.1521973388\C,1.4406732
 071,-2.7393270511,0.2551000703\C,1.1205098771,-1.3799751552,0.27935544
 32\C,-0.2082917237,-0.9698407254,0.2006684985\C,-1.2376244475,-1.91814
 19606,0.0951276803\C,-0.9095965238,-3.2816992023,0.0725910433\H,0.6622
 47472,-4.7464208811,0.1332262032\H,-0.4627303657,0.0833125393,0.224509
 6883\H,-1.7116831541,-4.0060330151,-0.0070804737\N,-4.1730561905,0.229
 7993599,-0.0830827525\N,-3.5909479485,-2.4667414272,-0.01929077\N,-2.8
 753557138,-0.1811760333,-0.0242854321\C,-2.6645303552,-1.5029181446,0.
 0062252381\H,-2.7394658124,2.0181361131,-1.3879578074\H,2.4777056282,-
 3.056913091,0.317202042\H,1.9085651633,-0.6368428313,0.3622914111\O,-8
 .1251110776,-3.6415391258,-0.676368334\C,-9.4810426242,-3.3137618236,-
 0.9390536679\H,-10.0147620189,-4.2638420756,-0.9866984781\H,-9.9122531
 459,-2.6986268777,-0.1390056077\H,-9.5937832146,-2.7892712272,-1.89644
 49427\Version=ES64L-G16RevA.03\State=2-A\HF=-1011.2227412\S2=0.766002
 \S2-1=0.\S2A=0.750168\RMSD=2.874e-09\RMSF=2.078e-05\Dipole=-1.3426816,
 1.0659114,-0.227931\Quadrupole=10.399594,-0.0646247,-10.3349693,0.5263
 1,0.1511448,0.7120339\PG=C01 [X(C20H16N3O1)]\@

Output parameters for 1.1(CI)

1\1\GINC-CPU-3\FOpt\UB3LYP\6-31G(d,p)\C19H13Cl1N3(2)\PRIMAL\13-Nov-2023\0\# opt ub3lyp/6-31g(d,p)\6-Cl-BTR\0,2\C,-7.2947782368,-2.5836700632,-0.1739654351\C,-5.9823042723,-2.9928268264,-0.00910863\C,-4.9474196265,-2.0368495734,0.0281850456\C,-5.2852545815,-0.6555886526,-0.0716537748\C,-6.6183718433,-0.2697232161,-0.2739339699\C,-7.6233682923,-1.2297318314,-0.3203916484\H,-5.7155764778,-4.0387759344,0.0784814987\H,-6.8728428066,0.774513389,-0.4020812396\H,-8.6545338234,-0.9343036525,-0.4739737758\C,-5.2416954478,2.2646376694,0.9415306597\C,-4.3646185509,1.6590710824,0.0343834565\C,-3.5824872925,2.4415057543,-0.8219885044\C,-3.6970666187,3.8289857112,-0.7816380138\C,-4.5843036675,4.4401215353,0.107284019\C,-5.3518480212,3.6543570041,0.9683698332\H,-5.8140745176,1.6545834192,1.6316096365\H,-3.0927125987,4.4342071312,-1.450401984\H,-4.6713169914,5.5218366221,0.1337763057\H,-6.0291423673,4.1218599709,1.6764842838\C,0.3531143641,-3.7177105438,0.105961183\C,1.3849873927,-2.7771864821,0.1116850429\C,1.0791789755,-1.414259204,0.1054020031\C,-0.2480913768,-0.9927213355,0.0927576093\C,-1.2896912032,-1.9336732426,0.0850792765\C,-0.9761453183,-3.3009154107,0.092701721\H,0.5839190675,-4.779048192,0.111210227\H,-0.4910480402,0.0633885162,0.0931219476\H,-1.7869227272,-4.0198385196,0.0885392312\N,-4.2147082046,0.2373158497,0.0072053973\N,-3.6516275849,-2.4594852933,0.1314582872\N,-2.9177367924,-0.1846683089,0.0035029488\C,-2.7142119526,-1.5059701206,0.0680281472\H,-2.8929755506,1.9531265,-1.5003234611\H,2.4210278115,-3.1035082654,0.1221516158\H,1.8773127669,-0.6775303815,0.112763651\Cl,-8.5783332033,-3.7826790952,-0.2190680308\Version=ES64L-G16RevA.03\State=2-A\HF=-1356.2920881\S2=0.766285\S2-1=0.\S2A=0.750165\RMSD=4.618e-09\RMSF=8.524e-06\Dipole=-0.028384,1.4977915,-0.0700321\Quadrupole=-0.0252604,5.6514135,-5.6261531,-6.875613,-2.4279885,-0.4068007\PG=C01 [X(C19H13Cl1N3)]\@

Output parameters for 1.3(Me)

```
1\1\GINC-CPU-78\FOpt\UB3LYP\6-31G\C20H16N3(2)\KONYENWE\29-May-2024\0\
# opt=tight ub3lyp/6-31g\6-MethylBTR\0,2\C,3.023296553,-2.2030285249
,0.044600167\C,1.6514617267,-2.4118953235,-0.0862326404\C,0.7358286588
,-1.3407371201,-0.0807668987\C,1.2308276841,-0.0084348982,0.0310057086
\C,2.6091223475,0.2072642724,0.2018251547\C,3.4848841663,-0.8761651411
,0.2038268077\H,1.239021734,-3.4102275901,-0.1809566759\H,2.9922298168
,1.2093582641,0.3429596256\H,4.5471128569,-0.6938586743,0.3375055747\C
,1.5261911875,2.9210347238,-0.927907829\C,0.5810164896,2.4144682013,-0
.0221212473\C,-0.1126739985,3.2831618574,0.8333782247\C,0.1594119525,4
.6524393847,0.7971167494\C,1.1169393291,5.1623097357,-0.0890360347\C,1
.7947826723,4.2928721205,-0.9515284897\H,2.0267849575,2.253222588,-1.6
191298132\H,-0.3758103831,5.3211105066,1.4632702047\H,1.3264409035,6.2
265605457,-0.1128012396\H,2.5226695966,4.6816830147,-1.6561104308\C,-4
.7486048292,-2.4135961083,-0.0496527803\C,-5.6715318868,-1.3620068112,
0.0107317788\C,-5.2137947233,-0.0386804832,0.0515914123\C,-3.844155710
5,0.2333306645,0.0330502736\C,-2.9133167749,-0.8200402593,-0.02546833\
C,-3.3777483163,-2.1466384566,-0.0675960751\H,-5.0969483695,-3.4412652
094,-0.0823603655\H,-3.4828572153,1.2540142209,0.0587567043\H,-2.65044
93802,-2.9477063181,-0.1147014062\N,0.2683897418,1.0168129644,0.003116
5736\N,-0.620241413,-1.6088099276,-0.1483212521\N,-1.0927157652,0.7458
187309,0.0375082914\C,-1.4554294243,-0.5543074291,-0.0427424559\H,-0.8
584651712,2.8762214051,1.5043012839\H,-6.7368574552,-1.5710388705,0.02
46002405\H,-5.9243155546,0.7809425603,0.0956106257\C,3.9996353586,-3.3
570583985,0.0238261888\H,4.6897389836,-3.3130694962,0.875122088\H,3.47
92817308,-4.3186479014,0.0612380394\H,4.6110862835,-3.3455067995,-0.88
82326131\Version=ES64L-G16RevA.03\State=2-A\HF=-935.7512651\S2=0.7692
86\S2-1=0.\S2A=0.750212\RMSD=6.056e-09\RMSF=1.209e-07\Dipole=1.1156028
,0.6578668,0.0900837\Quadrupole=5.1719643,4.2401489,-9.4121132,-0.5518
872,-2.5584107,0.6117771\PG=C01 [X(C20H16N3)]\@
```

Appendix B $^1\text{H-NMR}$ and $^{13}\text{C-NMR}$ spectra

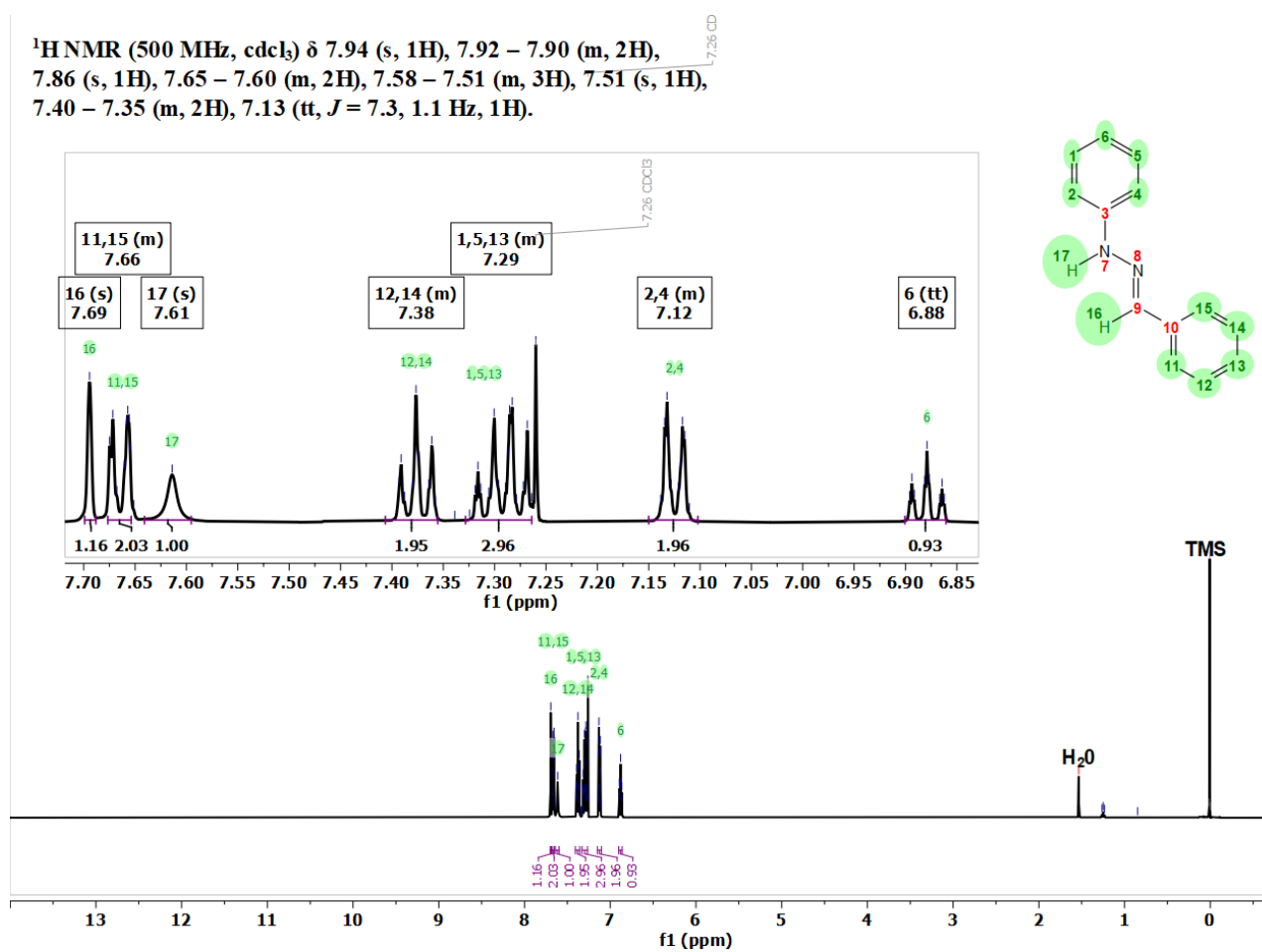


Figure B. 1 $^1\text{H-NMR}$ spectrum of **2.35** in CDCl_3

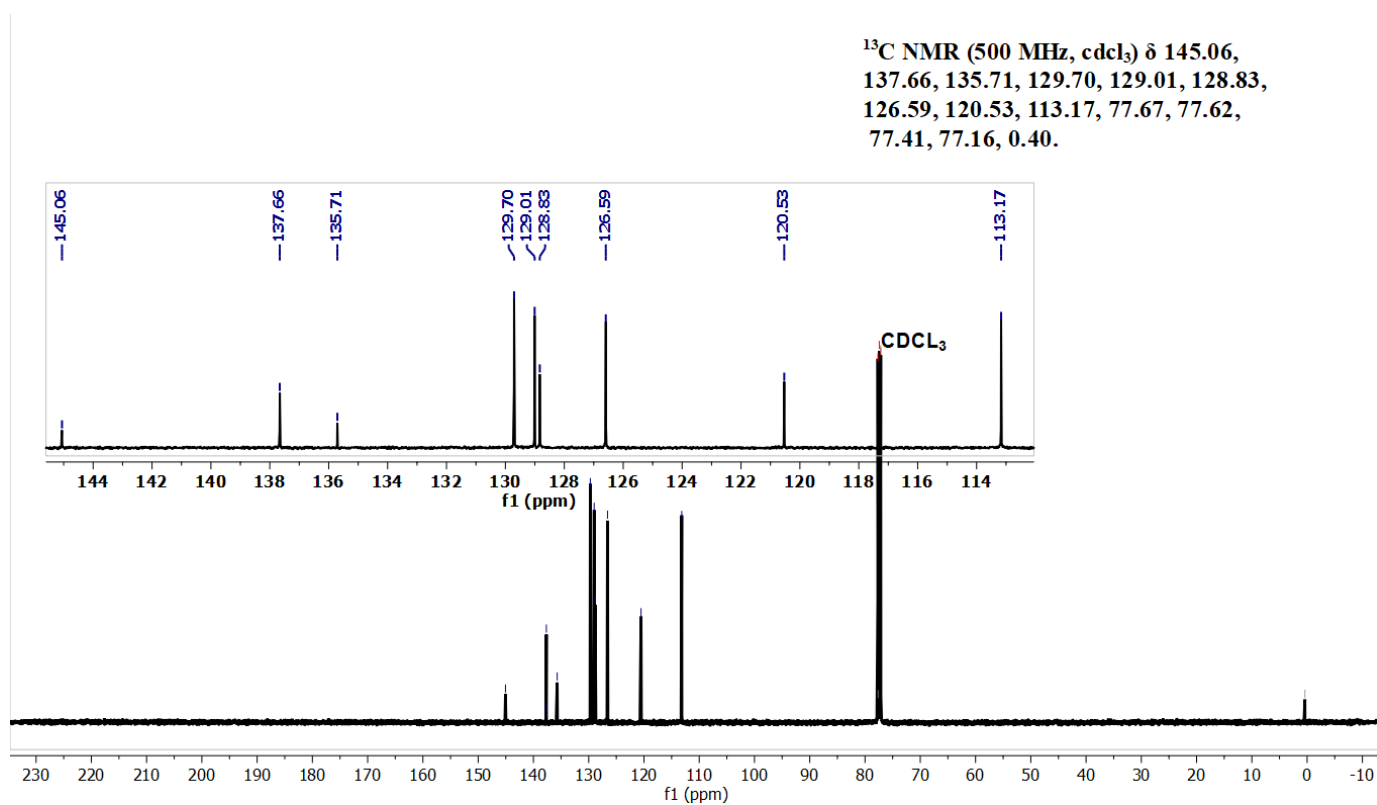


Figure B. 2 ^{13}C -NMR spectrum of **2.35** in CDCl_3

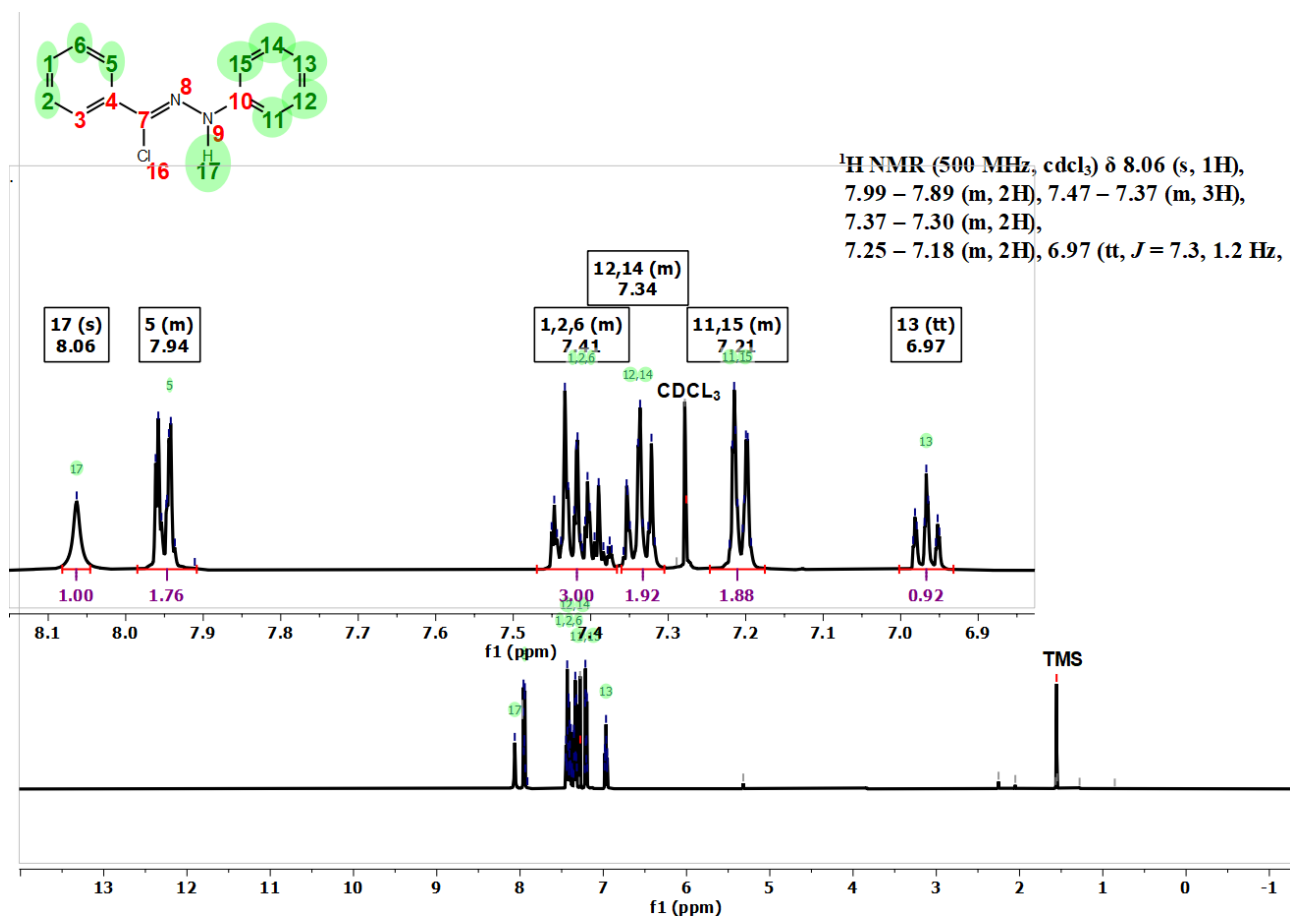


Figure B. 3 Figure B. 4 H-NMR spectrum of **2.36** in CDCl₃

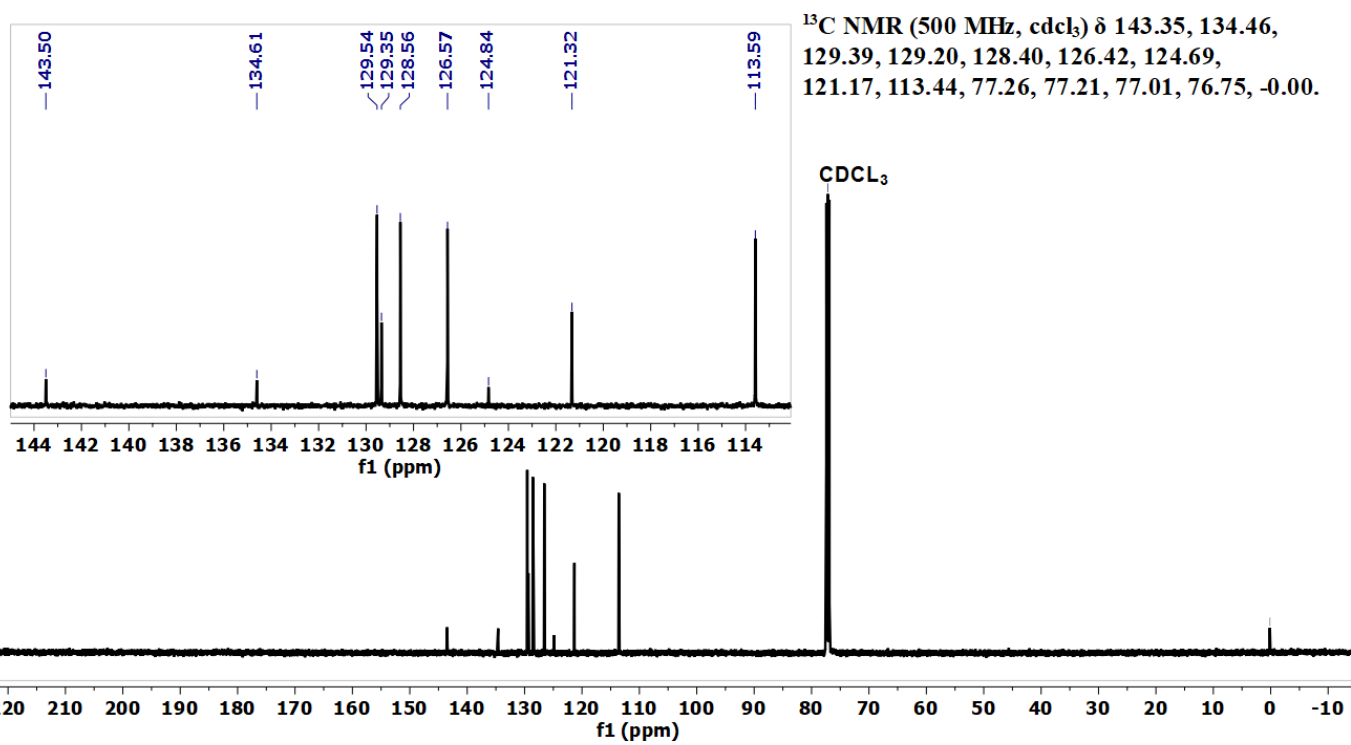


Figure B. 5 ^{13}C -NMR spectrum of 2.36 in CDCl_3

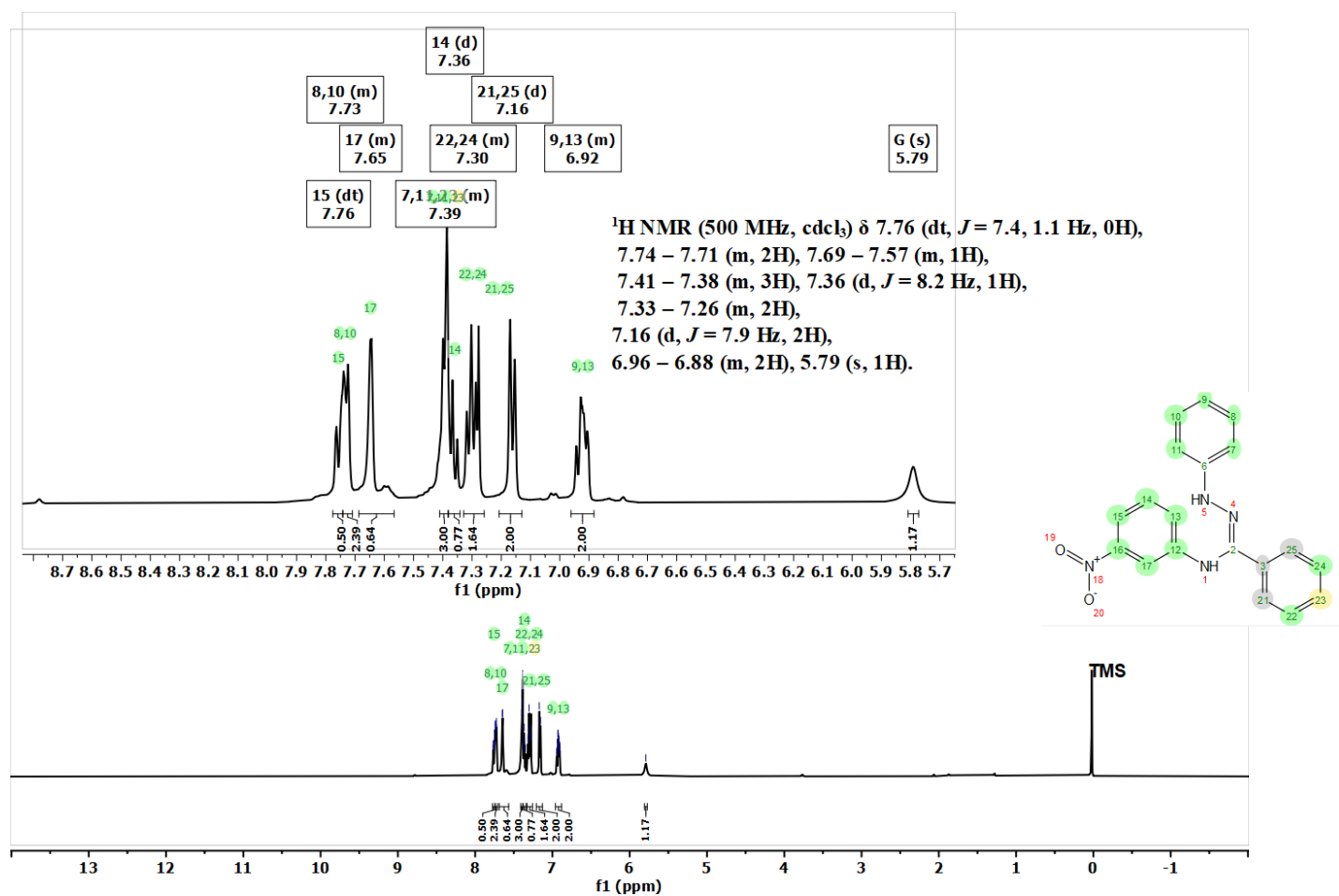


Figure B. ⁶H-NMR spectrum of **1.8** in CDCl_3

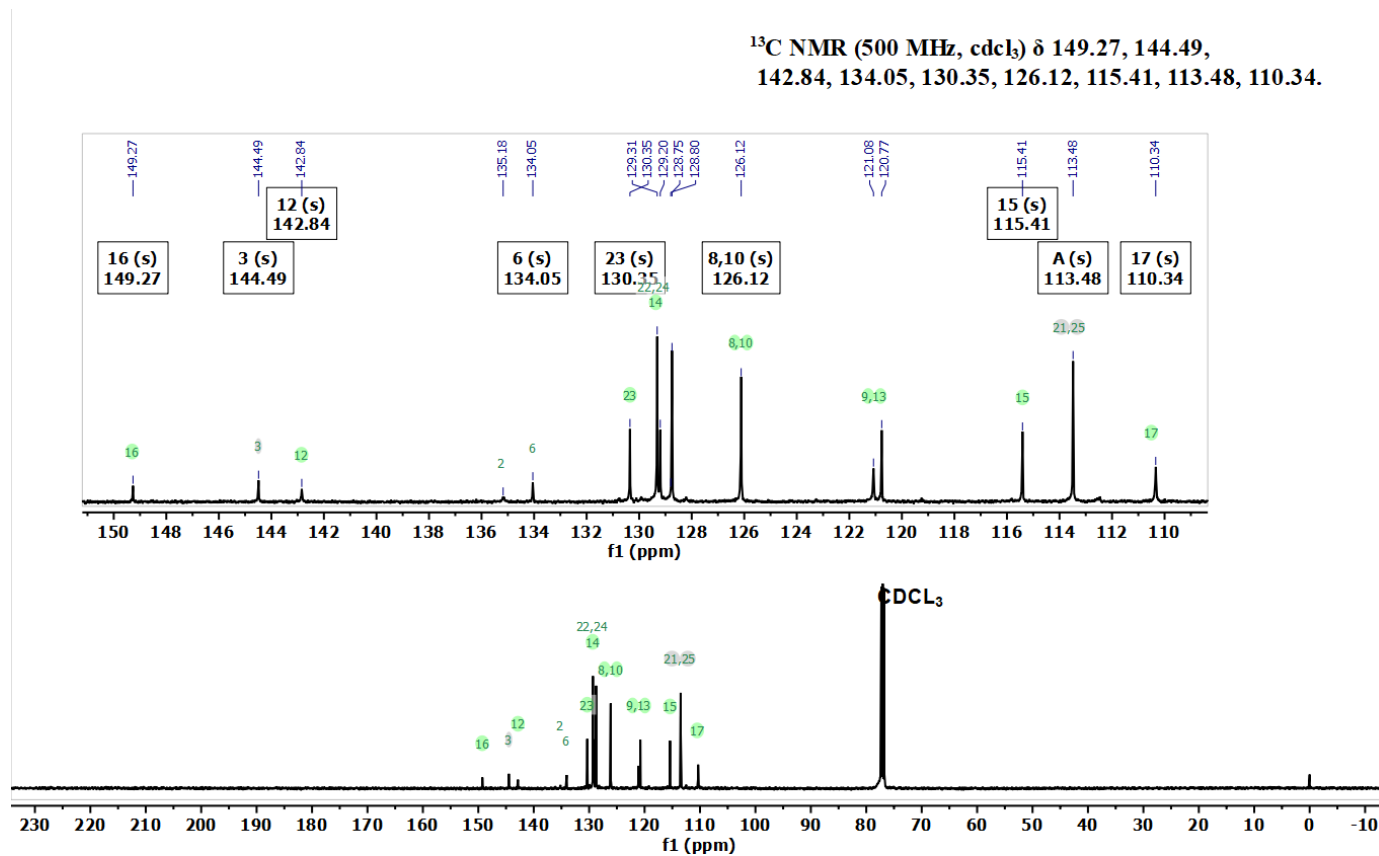


Figure B. 7 ^{13}C -NMR spectrum of **1.8** in CDCl_3

Appendix C Complete listings of bond lengths and angles

Table 4 Bond Lengths for . 1.1

Atom Atom Length/Å			Atom Atom Length/Å		
N4	C1	1.378(4)	C6	C7	1.391(5)
N4	C13	1.406(4)	C8	C9	1.402(4)
N2	N1	1.463(3)	C8	C13	1.392(4)
N2	C1	1.294(4)	C9	C10	1.402(4)
N1	C8	1.427(4)	C10	C11	1.381(5)
N1	C14	1.420(4)	C11	C12	1.391(5)
N4	C9	1.379(4)	C12	C13	1.385(4)
C1	C2	1.480(4)	C14	C15	1.399(4)
C2	C3	1.392(5)	C14	C19	1.396(4)
C2	C7	1.393(4)	C15	C16	1.383(5)

Table 4 Bond Lengths for . 1.1

Atom Atom Length/Å			Atom Atom Length/Å		
C3	C4	1.379(5)	C16	C17	1.391(5)
C4	C5	1.369(5)	C17	C18	1.387(5)
C5	C6	1.385(5)	C18	C19	1.389(5)

Table 5 Bond Angles for 1.1.

Atom Atom Atom Angle/°				Atom Atom Atom Angle/°			
C1	N4	C13	118.6(3)	C13	C8	C9	120.5(3)
C1	N2	N1	114.1(2)	N4	C9	C8	120.8(3)
C8	N1	N2	114.5(2)	N4	C9	C10	121.4(3)
C14	N1	N2	111.0(2)	C10	C9	C8	117.7(3)
C14	N1	C8	118.4(2)	C11	C10	C9	120.7(3)
N4	C1	C2	117.8(3)	C10	C11	C12	121.7(3)
N2	C1	N4	123.9(3)	C13	C12	C11	117.7(3)
N2	C1	C2	118.2(3)	C8	C13	N4	115.2(3)

Table 5 Bond Angles for 1.1.

Atom Atom Atom Angle/°				Atom Atom Atom Angle/°			
C3	C2	C1	122.5(3)	C12	C13	N4	123.3(3)
C7	C2	C1	118.3(3)	C12	C13	C8	121.5(3)
C7	C2	C3	119.1(3)	C15	C14	N1	119.9(3)
C4	C3	C2	120.7(3)	C19	C14	N1	121.0(3)
C5	C4	C3	119.8(3)	C19	C14	C15	119.1(3)
C4	C5	C6	120.8(3)	C16	C15	C14	120.2(3)
C5	C6	C7	119.6(3)	C15	C16	C17	120.6(3)
C6	C7	C2	119.9(3)	C18	C17	C16	119.3(3)
C9	C8	N1	120.9(3)	C17	C18	C19	120.5(3)
C13	C8	N1	118.6(3)	C18	C19	C14	120.2(3)

Table 6 Hydrogen Bonds for 1.1

D	H	A	d(D-H)/Å	d(H-A)/Å	d(D-A)/Å	D-H-A/°
N4	H4B	N2 ¹	0.89(5)	2.22(5)	3.081(4)	163(4)

¹-X,-1/2+Y,1/2-Z

Table 7 Torsion Angles for 1.1

A	B	C	D	Angle/°	A	B	C	D	Angle/°
N4	C1	C2	C3	-36.2(5)	C3	C4	C5	C6	2.9(6)
N4	C1	C2	C7	140.7(3)	C4	C5	C6	C7	-2.3(6)
N2	N1	C8	C9	142.3(3)	C5	C6	C7	C2	-0.9(5)
N2	N1	C8	C13	-35.5(4)	C7	C2	C3	C4	-2.9(5)
N2	N1	C14	C15	-29.1(4)	C8	N1	C14	C15	-164.6(3)
N2	N1	C14	C19	151.8(3)	C8	N1	C14	C19	16.2(4)
N2	C1	C2	C3	144.0(3)	C8	C9	C10	C11	2.2(5)
N2	C1	C2	C7	-39.1(4)	C9	C8	C13	N4	-172.7(3)
N1	N2	C1	N4	-9.7(4)	C9	C8	C13	C12	5.9(5)
N1	N2	C1	C2	170.1(3)	C9	C10	C11	C12	1.3(5)
N1	C8	C9	N4	0.3(5)	C10	C11	C12	C13	-1.3(5)
N1	C8	C9	C10	176.5(3)	C11	C12	C13	N4	176.2(3)
N1	C8	C13	N4	5.1(4)	C11	C12	C13	C8	-2.3(5)

Table 7 Torsion Angles for 1.1

A	B	C	D	Angle/°	A	B	C	D	Angle/°
N1	C8	C13	C12	-176.3(3)	C13	N4	C1	N2	-21.9(5)
N1	C14	C15	C16	178.3(3)	C13	N4	C1	C2	158.3(3)
N1	C14	C19	C18	-178.1(3)	C13	C8	C9	N4	178.1(3)
N4	C9	C10	C11	178.4(3)	C13	C8	C9	C10	-5.7(5)
C1	N4	C13	C8	23.6(4)	C14	N1	C8	C9	-83.6(4)
C1	N4	C13	C12	-155.0(3)	C14	N1	C8	C13	98.6(3)
C1	N2	N1	C8	37.5(4)	C14	C15	C16	C17	0.1(5)
C1	N2	N1	C14	-99.8(3)	C15	C14	C19	C18	2.8(5)
C1	C2	C3	C4	174.0(3)	C15	C16	C17	C18	2.0(5)
C1	C2	C7	C6	-173.6(3)	C16	C17	C18	C19	-1.8(5)
C2	C3	C4	C5	-0.2(6)	C17	C18	C19	C14	-0.6(5)
C3	C2	C7	C6	3.4(5)	C19	C14	C15	C16	-2.5(5)

Table 4 Bond Lengths for cu_KinglseyR1_a (1).

Atom Atom Length/Å			Atom Atom Length/Å		
C11	C12	1.7414(15)	C6	C7	1.3872(19)
N1	N2	1.3612(16)	C6	C16	1.385(2)
N1	C4	1.4370(16)	C7	C8	1.382(2)
N1	C15	1.3875(17)	C8	C9	1.367(2)
N2	C5	1.3349(17)	C9	C17	1.371(3)
N3	C5	1.3373(18)	C10	C11	1.4052(19)
N3	C10	1.3656(18)	C10	C15	1.4173(18)
C1	C2	1.366(3)	C11	C12	1.369(2)
C1	C19	1.372(3)	C12	C13	1.390(2)
C2	C3	1.384(2)	C13	C14	1.379(2)
C3	C4	1.373(2)	C14	C15	1.393(2)
C4	C18	1.380(2)	C16	C17	1.382(3)
C5	C6	1.484(2)	C18	C19	1.385(2)

Table 5 Bond Angles for 1.4.

Atom Atom Atom Angle/°				Atom Atom Atom Angle/°			
N2	N1	C4	113.91(11)	C9	C8	C7	120.09(15)
N2	N1	C15	122.82(10)	C8	C9	C17	119.75(16)
C15	N1	C4	123.14(11)	N3	C10	C11	119.62(12)
C5	N2	N1	115.76(11)	N3	C10	C15	121.89(12)
C5	N3	C10	115.70(11)	C11	C10	C15	118.49(13)
C2	C1	C19	120.19(14)	C12	C11	C10	119.81(13)
C1	C2	C3	120.40(15)	C11	C12	C11	119.59(11)
C4	C3	C2	119.23(15)	C11	C12	C13	121.84(13)
C3	C4	N1	119.24(13)	C13	C12	C11	118.56(12)
C3	C4	C18	120.92(13)	C14	C13	C12	119.35(14)
C18	C4	N1	119.82(12)	C13	C14	C15	120.30(13)
N2	C5	N3	127.68(13)	N1	C15	C10	116.03(12)
N2	C5	C6	114.51(12)	N1	C15	C14	123.78(12)
N3	C5	C6	117.79(11)	C14	C15	C10	120.17(12)

Table 5 Bond Angles for 1.4.

Atom Atom Atom Angle/°	Atom Atom Atom Angle/°
C7 C6 C5 119.86(13)	C17 C16 C6 120.38(15)
C16 C6 C5 121.89(13)	C9 C17 C16 120.61(17)
C16 C6 C7 118.21(14)	C4 C18 C19 118.95(15)
C8 C7 C6 120.94(14)	C1 C19 C18 120.30(16)

Table 6 Torsion Angles for 1.4.

A B C D Angle/°	A B C D Angle/°
C11 C12 C13 C14 -179.42(11)	C5 N3 C10 C15 1.34(19)
N1 N2 C5 N3 -0.1(2)	C5 C6 C7 C8 176.88(13)
N1 N2 C5 C6 178.37(11)	C5 C6 C16 C17 -175.81(17)
N1 C4 C18 C19 -179.65(15)	C6 C7 C8 C9 -0.5(2)
N2 N1 C4 C3 -55.07(17)	C6 C16 C17 C9 -1.5(3)
N2 N1 C4 C18 123.07(15)	C7 C6 C16 C17 1.8(3)
N2 N1 C15 C10 -3.71(18)	C7 C8 C9 C17 0.8(3)

Table 6 Torsion Angles for 1.4.

A	B	C	D	Angle/°	A	B	C	D	Angle/°
N2	N1	C15	C14	175.13(12)	C8	C9	C17	C16	160.2(3)
N2	C5	C6	C7	179.67(12)	C10	N3	C5	N2	-2.1(2)
N2	C5	C6	C16	-2.8(2)	C10	N3	C5	C6	179.50(11)
N3	C5	C6	C7	-1.73(19)	C10	C11	C12	C11	-179.98(10)
N3	C5	C6	C16	175.80(14)	C10	C11	C12	C13	-0.6(2)
N3	C10	C11	C12	178.59(12)	C11	C10	C15	N1	-179.02(11)
N3	C10	C15	N1	1.35(19)	C11	C10	C15	C14	2.09(19)
N3	C10	C15	C14	-177.54(12)	C11	C12	C13	C14	1.2(2)
C1	C2	C3	C4	-0.4(3)	C12	C13	C14	C15	-0.1(2)
C2	C1	C19	C18	180.5(3)	C13	C14	C15	N1	179.66(13)
C2	C3	C4	N1	179.59(15)	C13	C14	C15	C10	-1.5(2)
C2	C3	C4	C18	1.5(2)	C15	N1	N2	C5	3.13(18)
C3	C4	C18	C19	-1.5(3)	C15	N1	C4	C3	120.93(15)
C4	N1	N2	C5	179.16(11)	C15	N1	C4	C18	-60.92(19)

Table 6 Torsion Angles for 1.4.

A	B	C	D	Angle/°	A	B	C	D	Angle/°
C4	N1	C15	C10	-179.37(12)	C15	C10	C11	C12	-1.1(2)
C4	N1	C15	C14	-0.5(2)	C16	C6	C7	C8	-0.7(2)
C4	C18	C19	C1	0.5(3)	C19	C1	C2	C3	-0.6(3)
C5	N3	C10	C11	-178.29(12)					

Table 7 Hydrogen Atom Coordinates ($\text{\AA} \times 10^4$) and Isotropic Displacement Parameters ($\text{\AA}^2 \times 10^3$) for 1.4.

Atom	<i>x</i>	<i>y</i>	<i>z</i>	U(eq)
H1	2781.61	7452.38	10143.98	84
H13	2092.04	5174.22	10666.26	85
H12	2313.48	4057.11	9201.18	72
H6	5338.85	798.27	5442.84	64
H7	7323.85	-1647.65	6093.36	75
H2	8944.2	-2701.93	7995.54	84

Table 7 Hydrogen Atom Coordinates ($\text{\AA}\times 10^4$) and Isotropic Displacement Parameters ($\text{\AA}^2\times 10^3$) for 1.4.

Atom	<i>x</i>	<i>y</i>	<i>z</i>	U(eq)
H5	1861.95	5042.18	3232.79	62
H4	-593.39	8849.03	3890.89	66
H3	907.17	7758.81	5855.4	63
H9	6501.09	1085.77	8661.09	83
H8	8542	-1331.64	9268.05	96
H11	3978.04	7525.89	6690.26	75
H10	3739.82	8625.45	8172.67	85

Appendix D SC-XRD Crystallographic data for 1.8 and 2.11

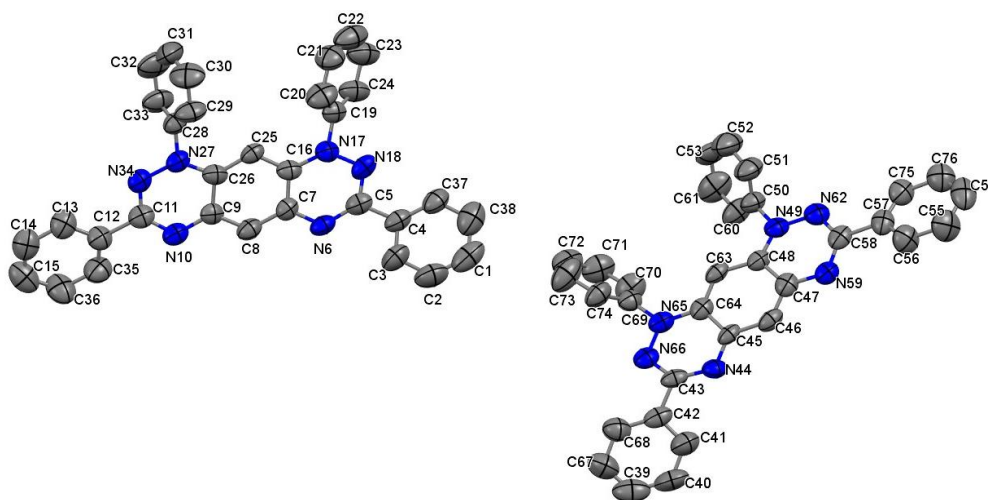


Figure 1. 29 The Crystal Structure of 1,3,7,9-Tetraphenyl-1H-benzo[1,2-e:5,4-e'] bis([1,2,4]triazine)-9-ium-6-ide (2.11-TPHA) (50% Probability Ellipsoids and Hydrogen Atoms Omitted for Clarity. Two molecules seen in the asymmetric unit cell

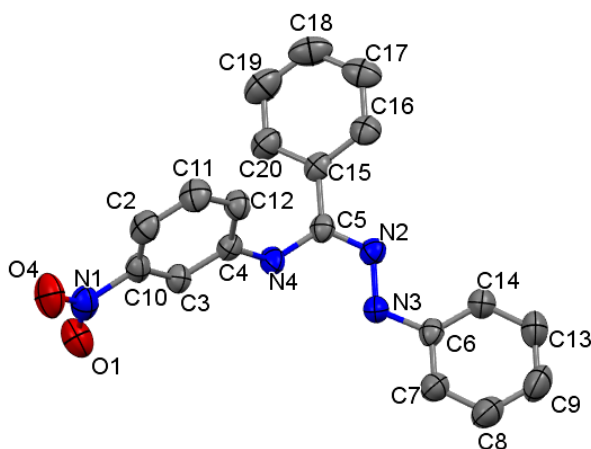
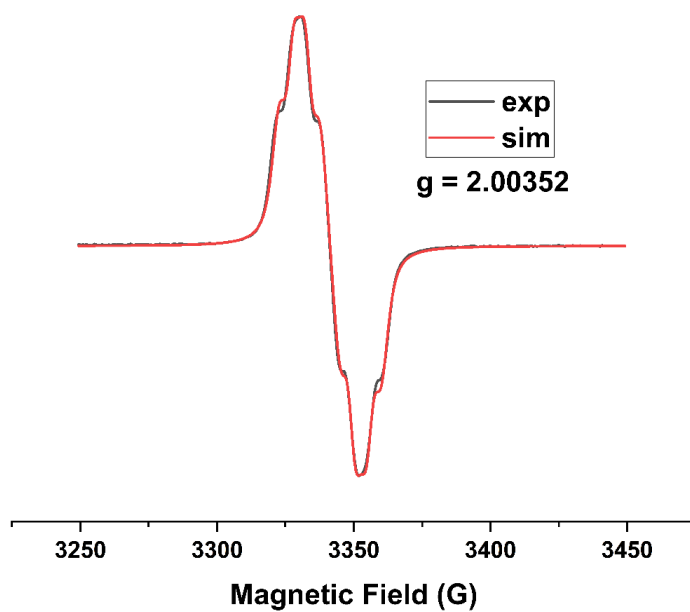
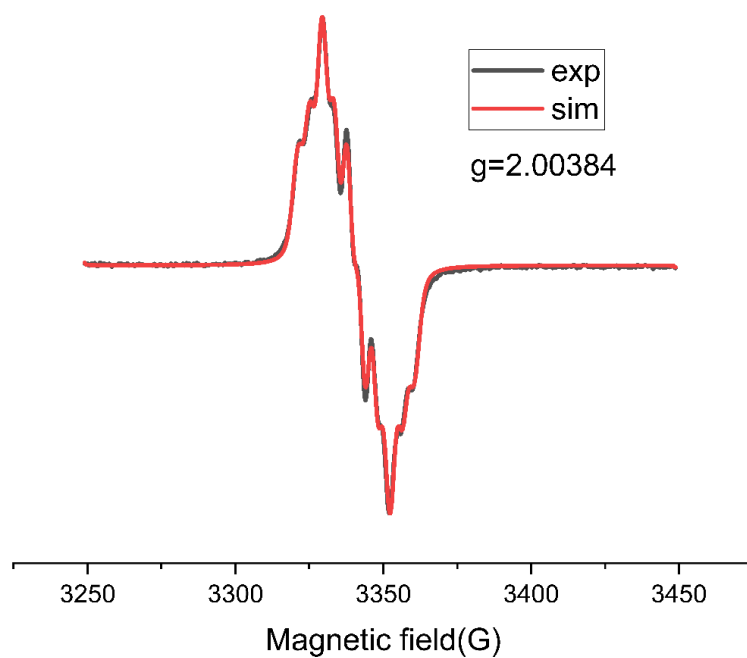


Figure 1. 30 Crystal Structure of 1.8 (50% Probability Ellipsoids and Hydrogen Atoms omitted for Clarity)

Appendix E X-band CW-EPR Spectrum of radicals 1.1-1.5**Figure 1. 31** X-band CW-EPR spectrum of 1.3 in toluene at 298 K**Figure 1. 32** X-band CW- EPR spectrum of 1.2 in toluene at 298 K

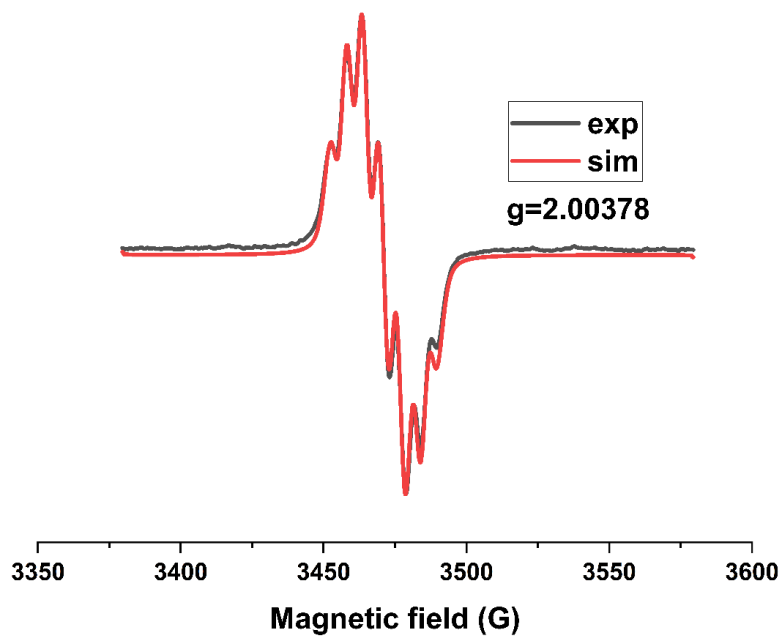


Figure 1. 5 CW X-band EPR spectrum of 1.5 in toluene at 298 K

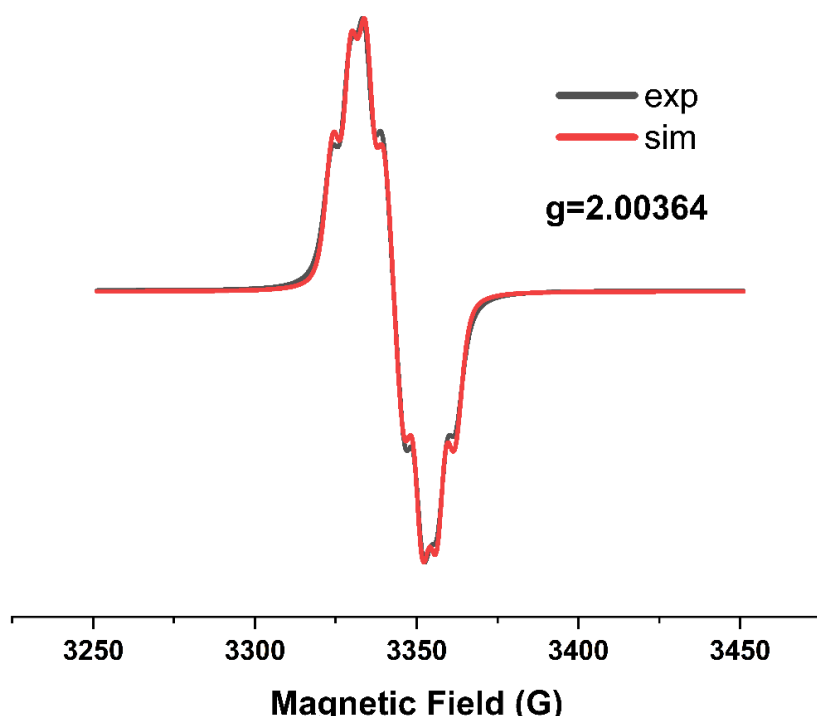


Figure 1. 33 CW X-band EPR spectrum of 1.4 in toluene at 298 K

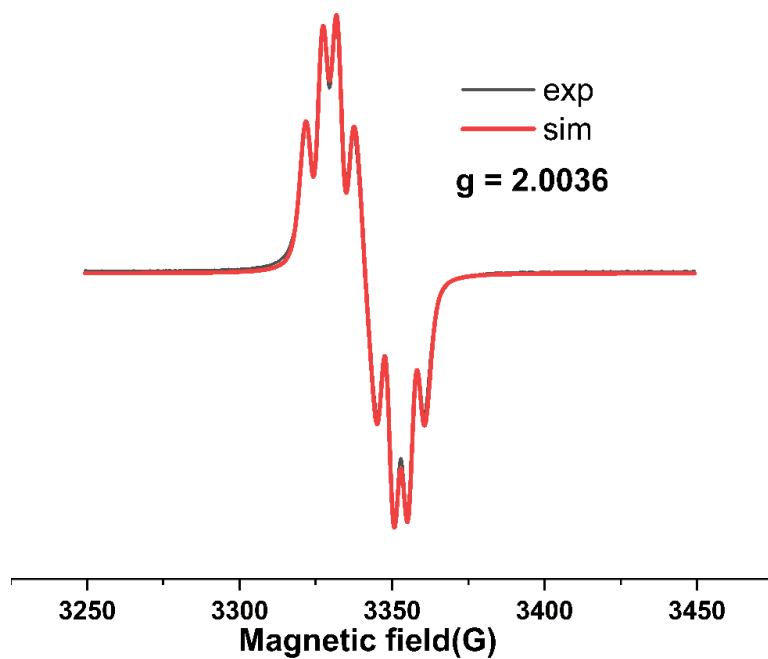


Figure 1. 34 Experimental and simulated EPR spectrum of 1.1 in toluene at 298 K

Appendix G Complete FTIR (ATR) Data

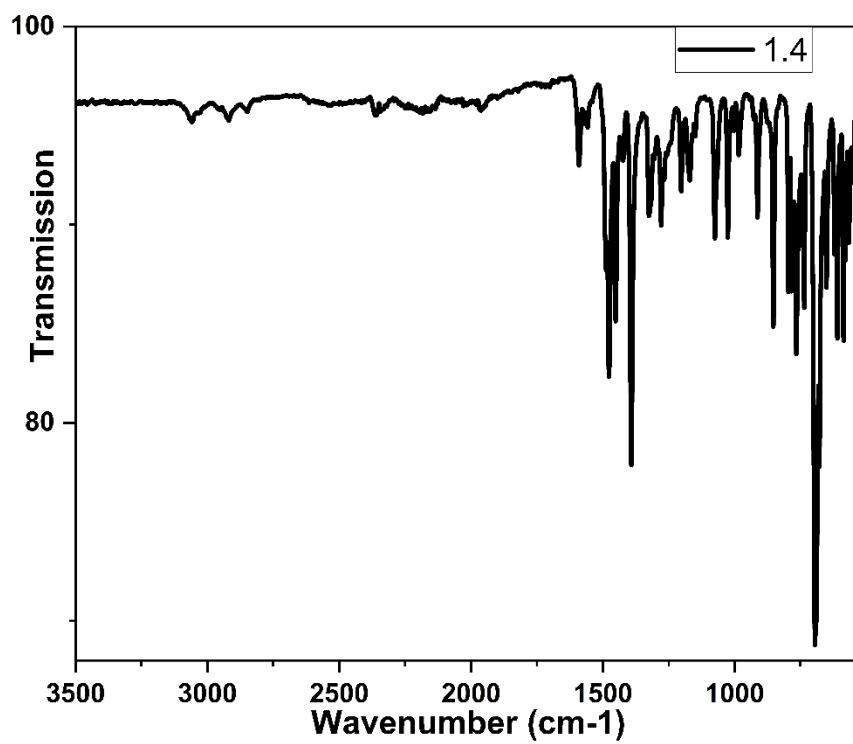


Figure G. 1 FTIR Spectrum for 1.4

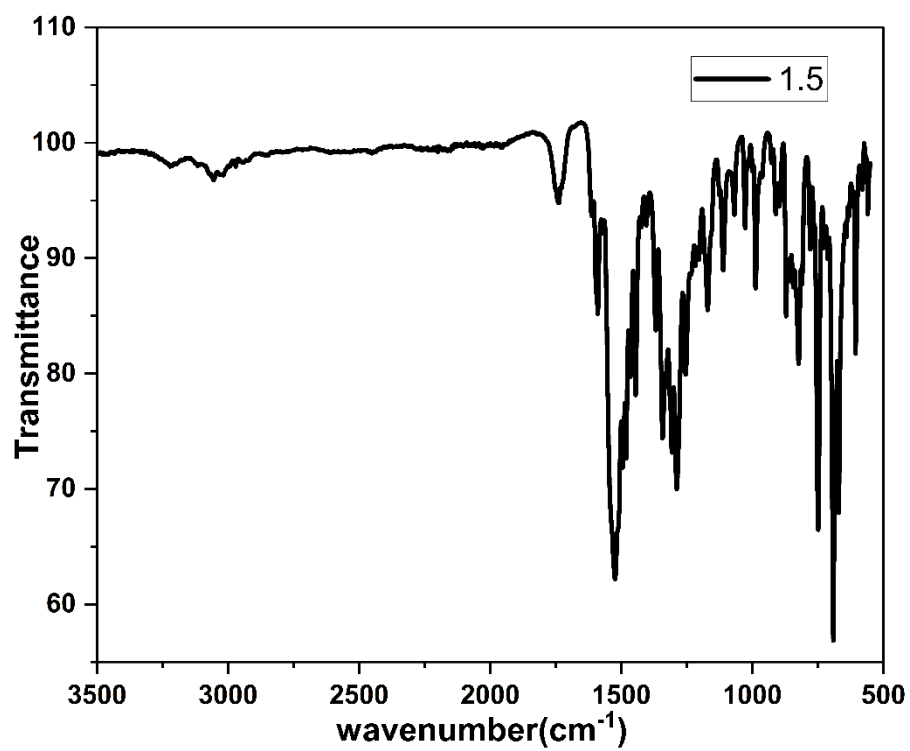


Figure G. 2 FTIR Spectrum for 1.5

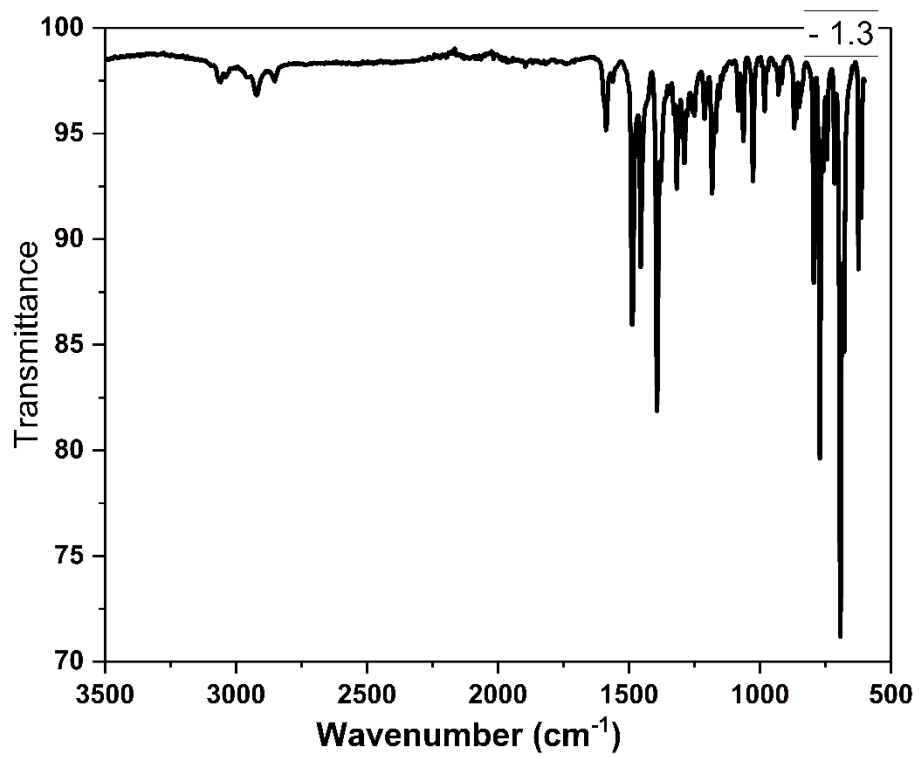


Figure G. 3 FTIR Spectrum for 1.3

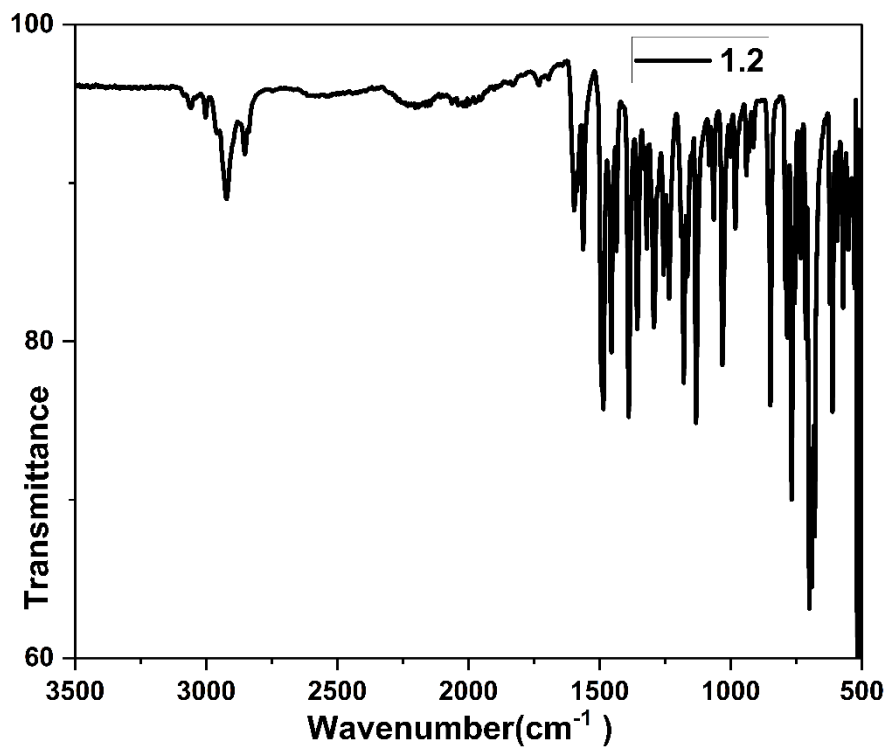


Figure G. 4 FTIR Spectrum for 1.2

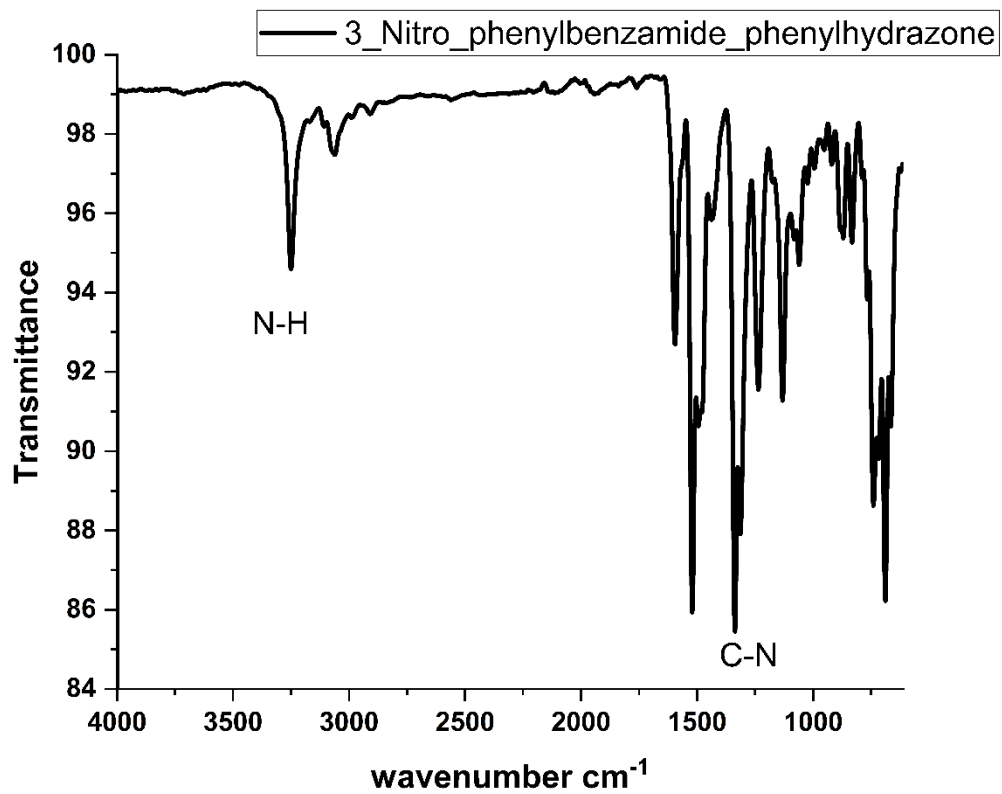


Figure G. 5 FTIR spectrum for 3-Nitro-N-Phenylbenzamide phenylhydrazone (1.8)

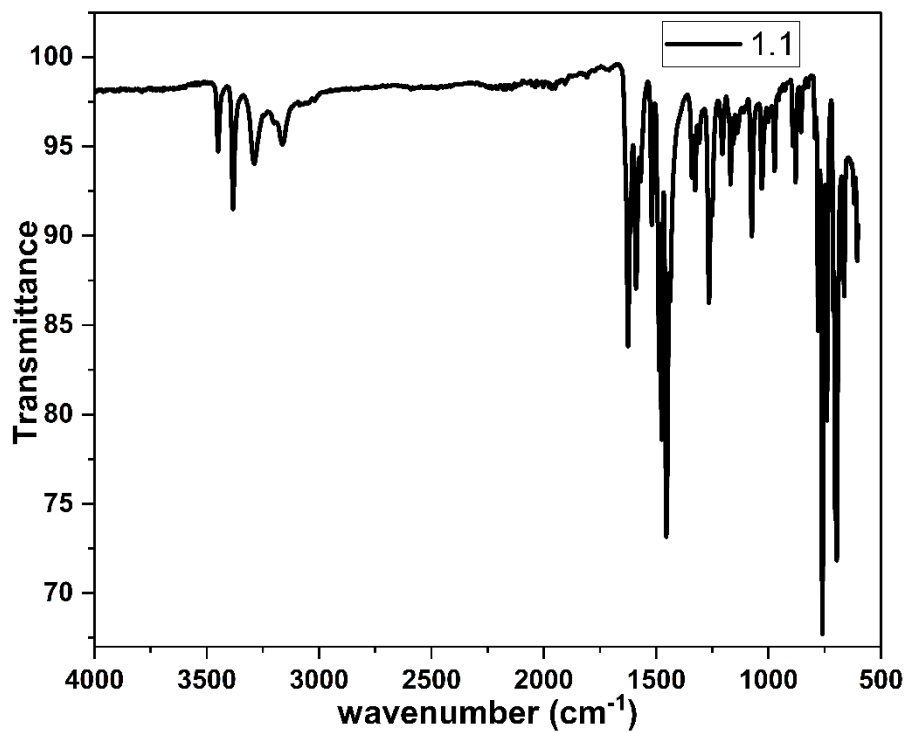


Figure G. 6 FTIR Spectrum for 1.1

Appendix H: Complete HRMS Data

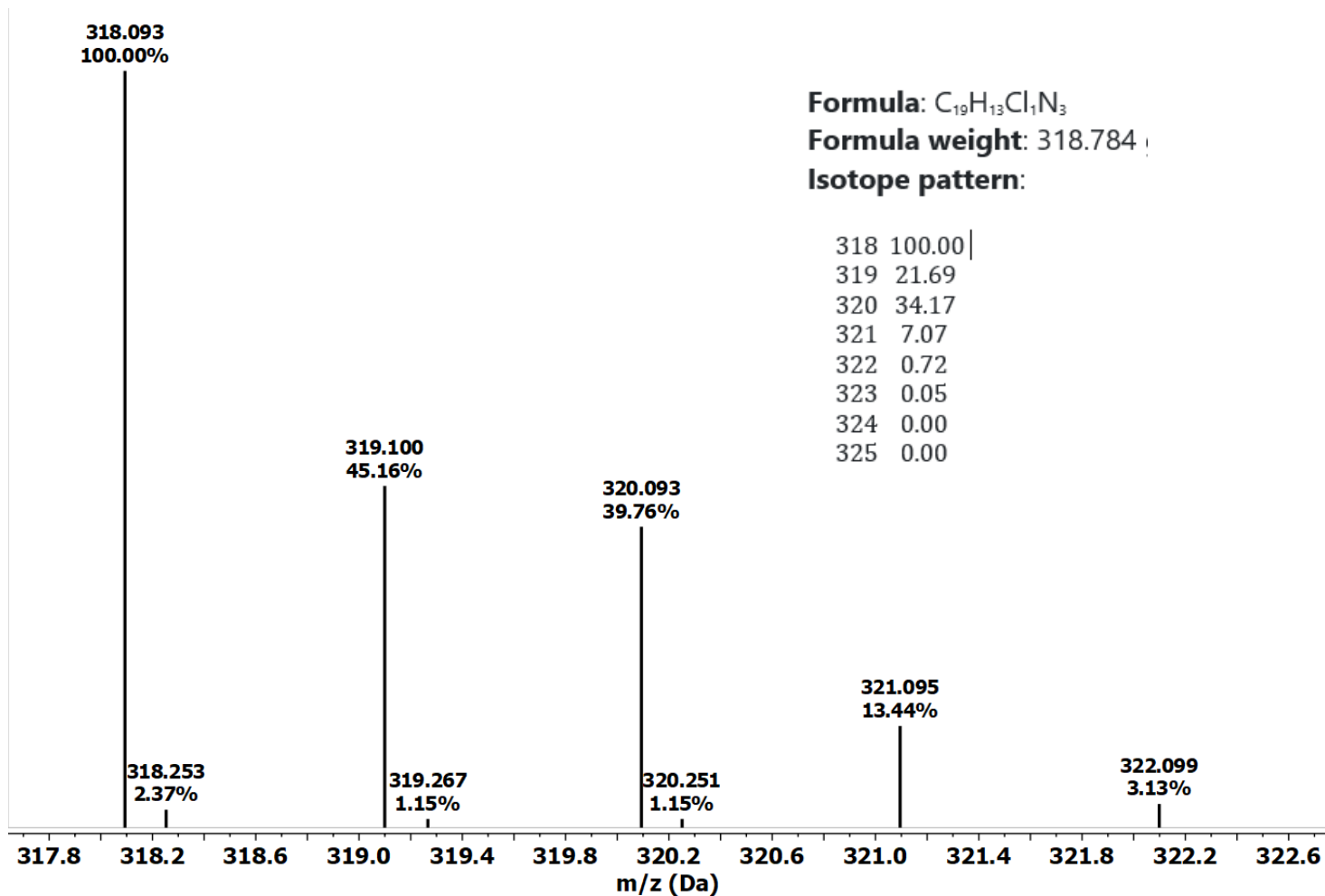


Figure H. 1 ESI-TOF Spectral data for 1.4

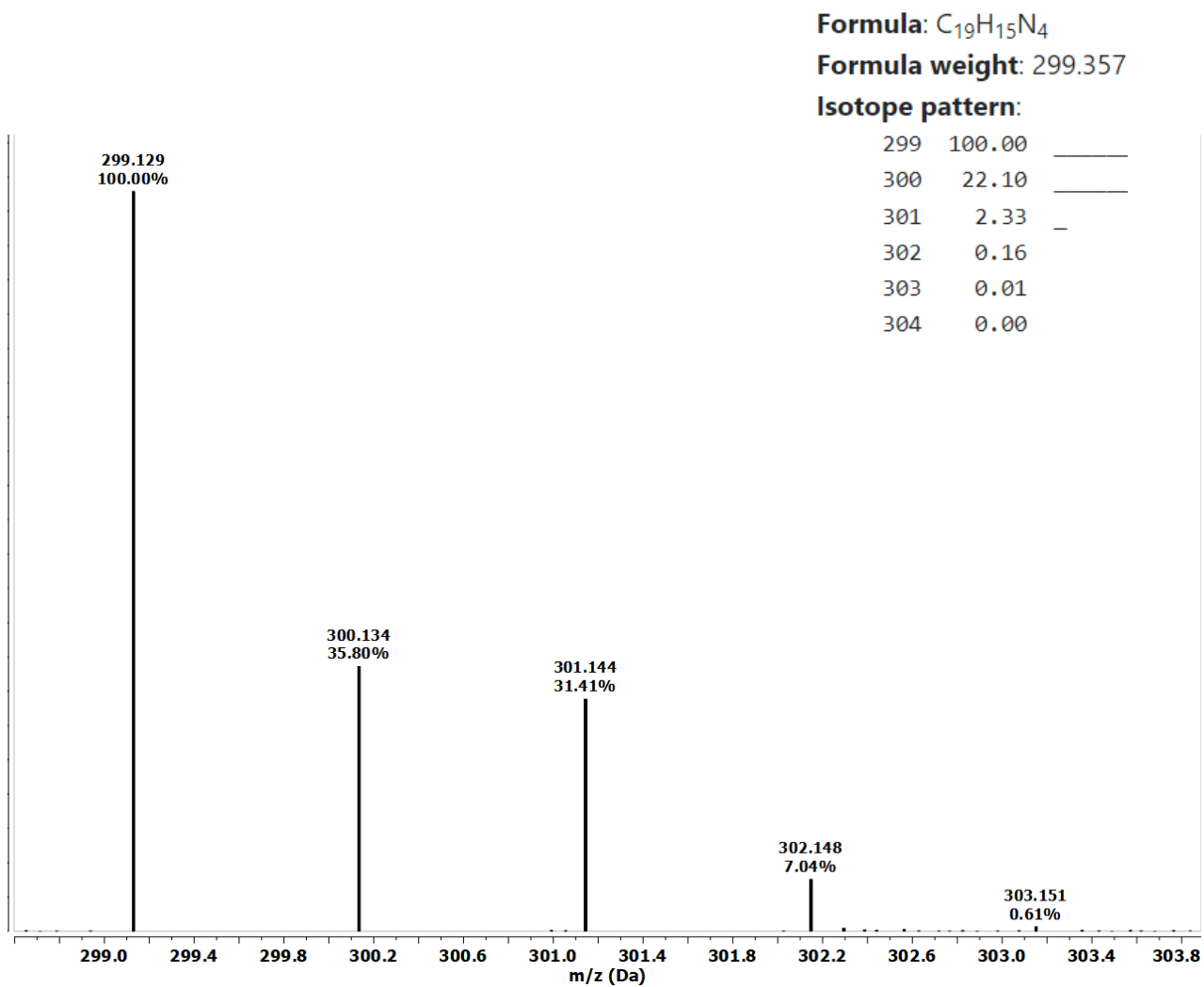


Figure H. 2 ESI-TOF Spectral data for 1.1

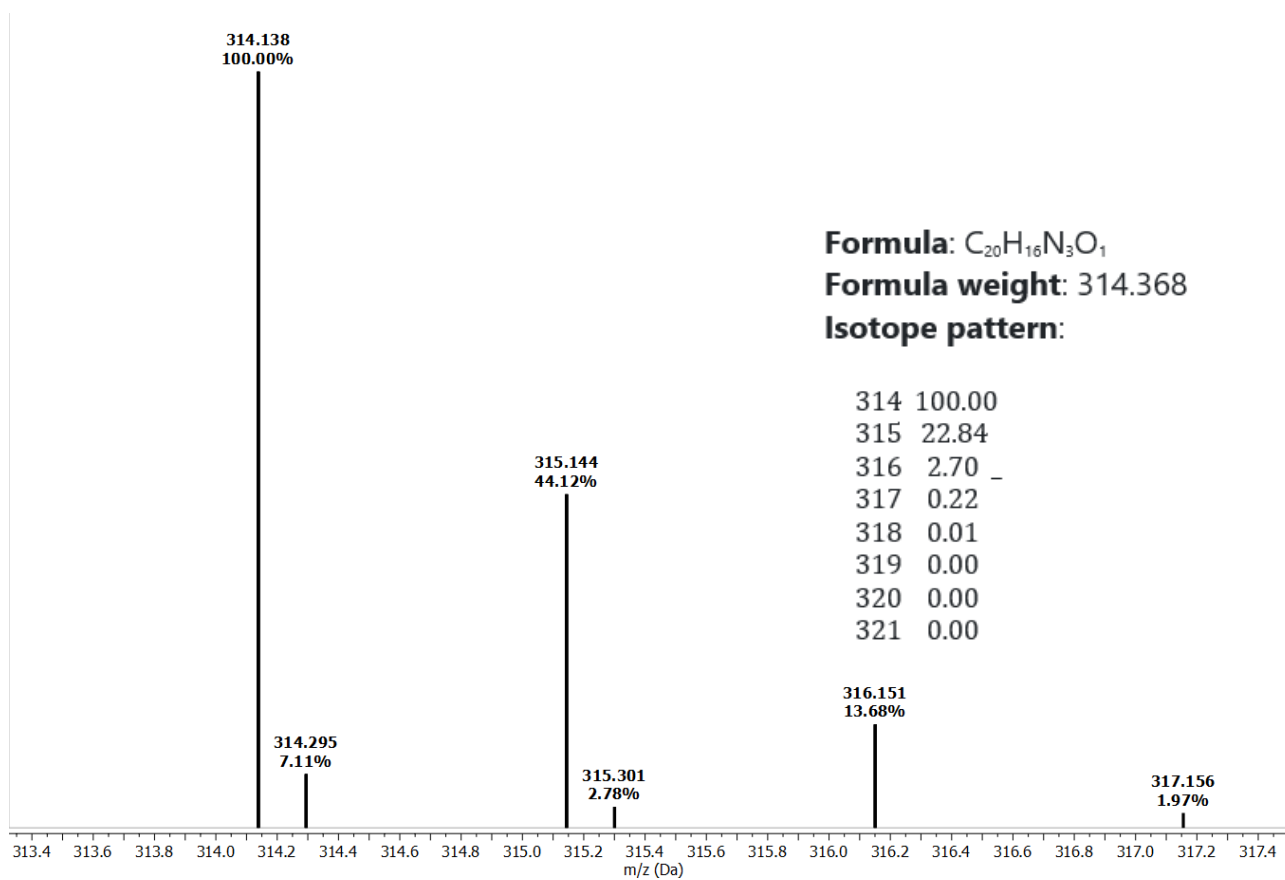


Figure H. 3 ESI-TOF Spectral data for 1.2

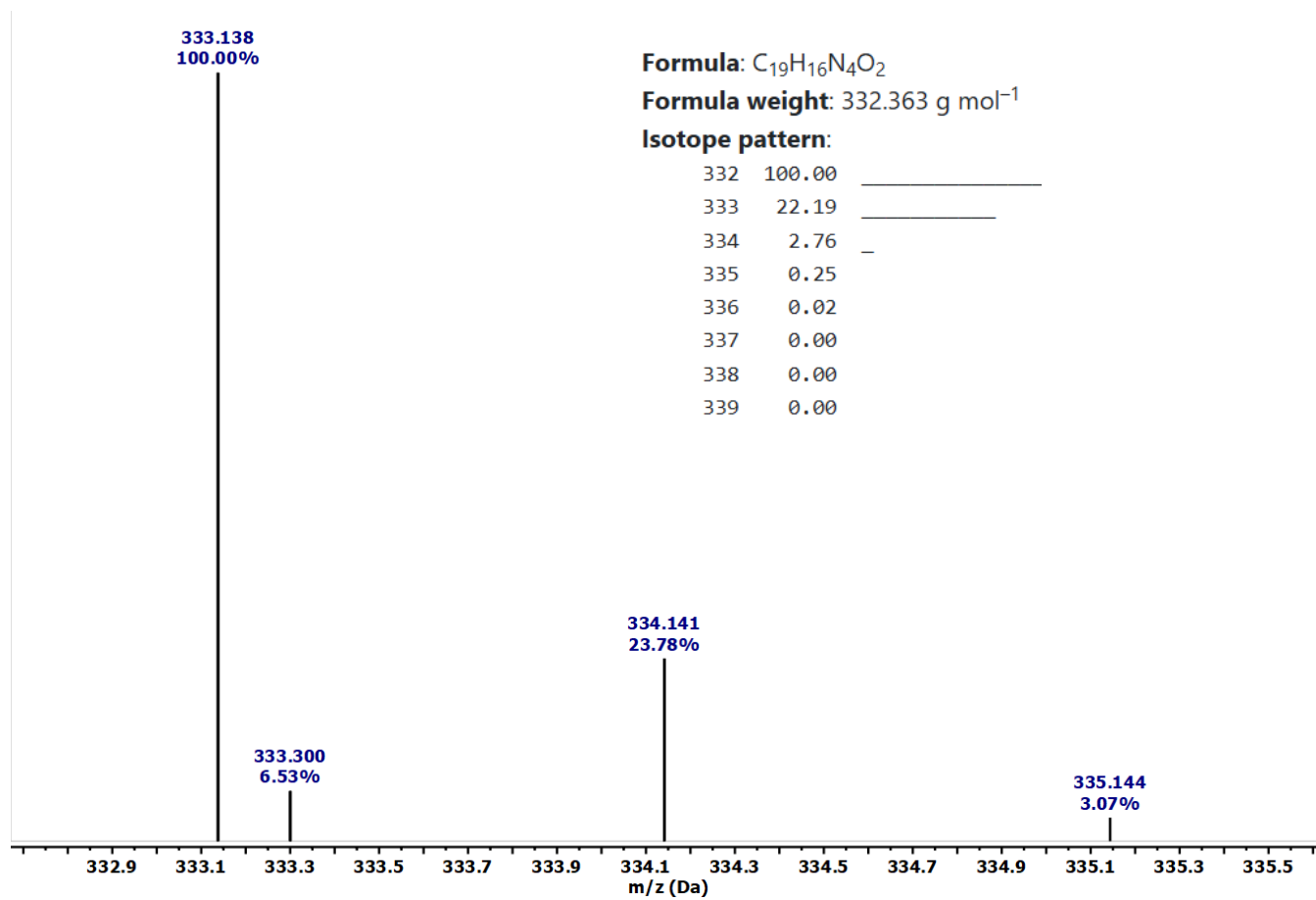


Figure H. 4 ESI-TOF Spectral data for 1.8

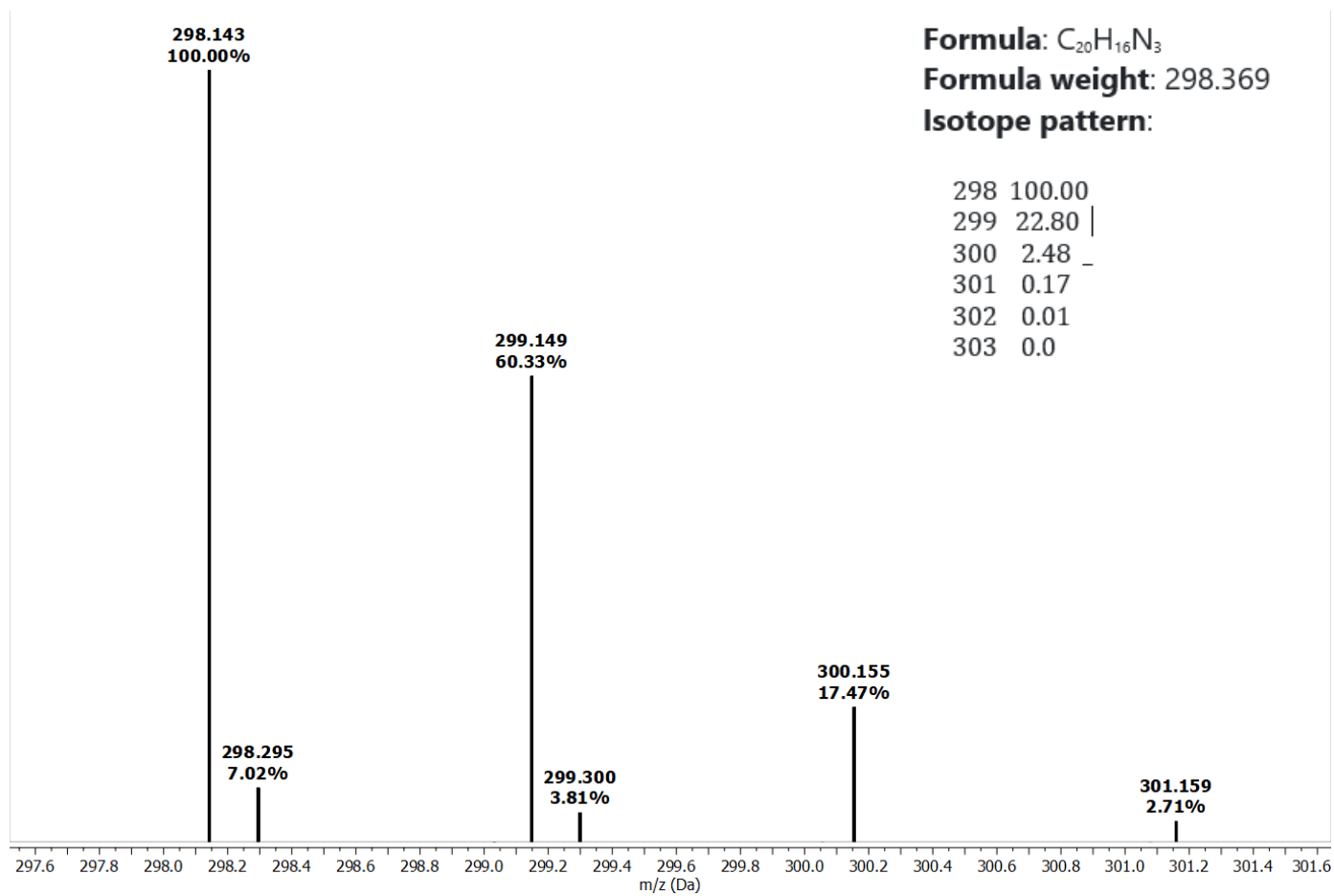


Figure H. 5 ESI-TOF Spectral data for 1.2

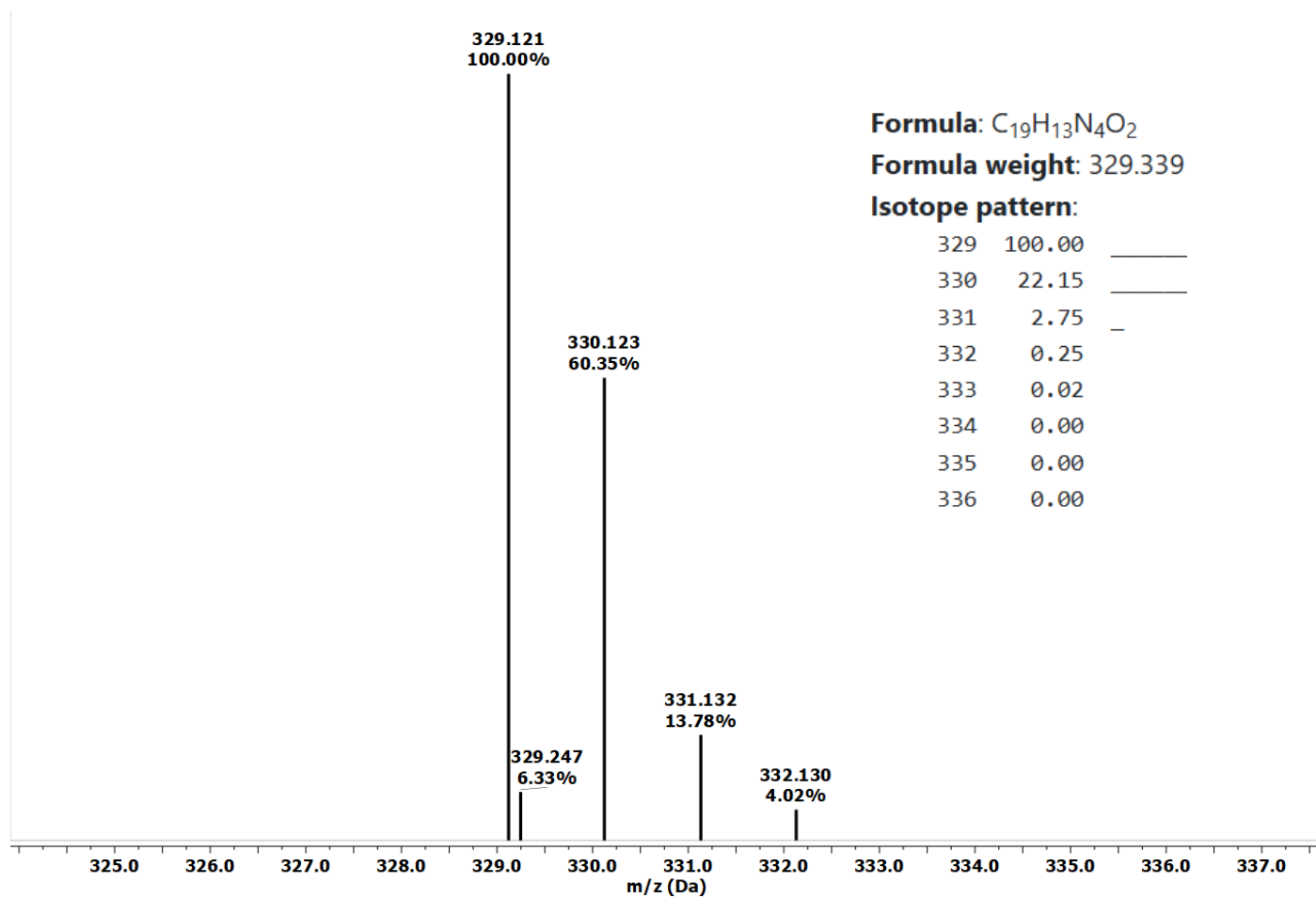


Figure H. 6 ESI-TOF Spectral data for 1.5

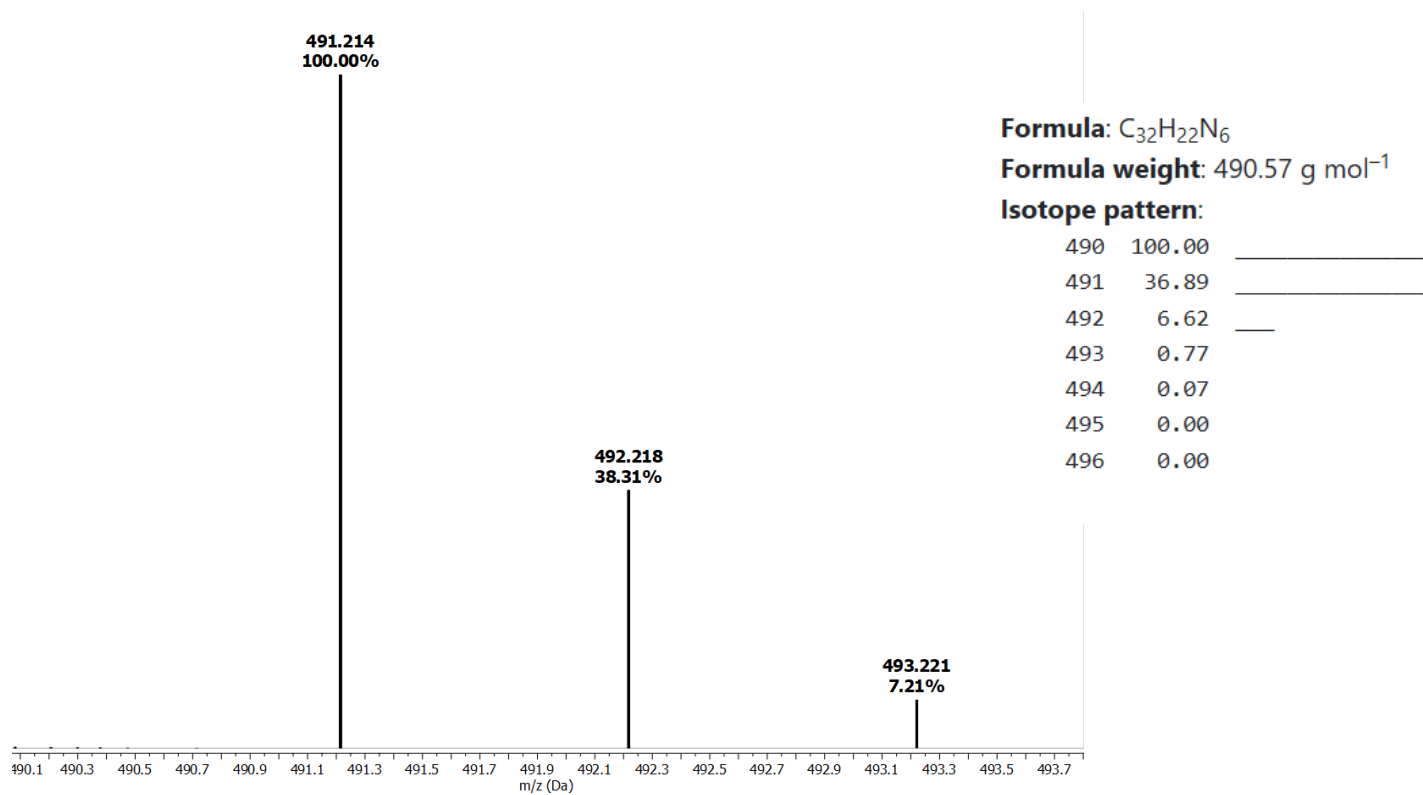


Figure H. 7 ESI-TOF Spectral data for 2.11

Appendix F Absorption Spectroscopic and cyclic voltammetry data for radical 1.1 and 1.12

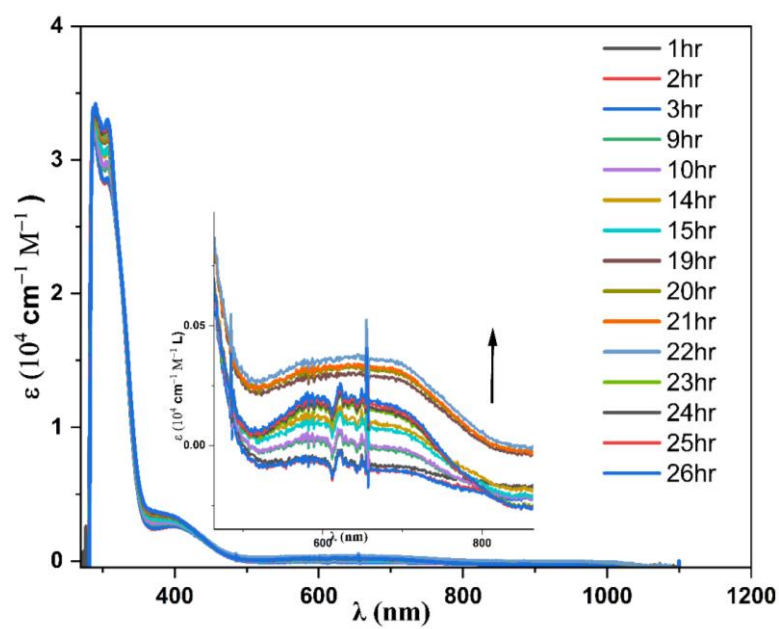


Figure 1. 35 Electronic absorption spectra of 1.12 in acetonitrile at 300k

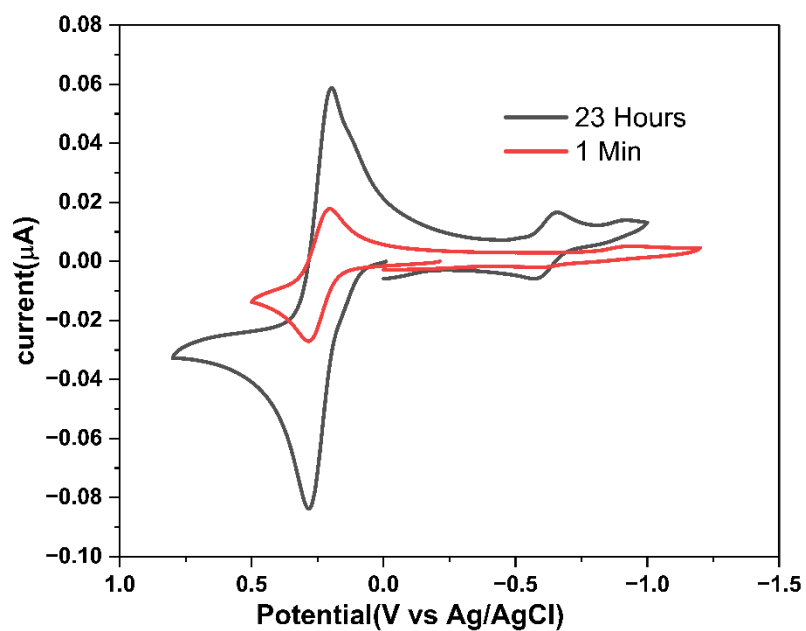


Figure 1. 36 Time-dependent Cyclic voltammogram of radical **1.1** in MeCN with 0.1 M [Bu₄N][PF₆] supporting electrolyte, glassy carbon working electrode, silver reference electrode, platinum counter electrode, 100 mV/s scan rate